

**Growth, microstructure and ferroelectric properties
of non-*c*-axis-oriented rare-earth-substituted
bismuth titanate thin films and nanostructures**

Dissertation

zur Erlangung des akademischen Grades

doctor rerum naturalium (Dr. rer. nat.)

vorgelegt der

Mathematisch-Naturwissenschaftlich-Technischen Fakultät
(mathematisch-naturwissenschaftlicher Bereich)
der Martin-Luther-Universität Halle-Wittenberg

von Herrn Sung Kyun Lee
geb.: 19.09.1972 in: Seoul

Gutachter:

1. Prof. Dr. Ulrich Gösele
2. Prof. Dr. Horst Beige
3. Prof. Dr. Lukas Eng

Halle/Saale, 22 Juni 2005,

verteidigt am 15 November 2005

urn:nbn:de:gbv:3-000009466

[<http://nbn-resolving.de/urn/resolver.pl?urn=nbn%3Ade%3Agbv%3A3-000009466>]

Contents

1	Introduction	1
2	Rare-earth element-substituted bismuth titanates	4
2.1	Rare-earth-substituted $\text{Bi}_4\text{Ti}_3\text{O}_{12}$ as a new class of ferroelectric materials	4
2.2	Epitaxial growth of Bi-layered perovskite oxides – achievements and problems	9
3	Experimental details	15
3.1	Deposition techniques	15
3.2	Structural characterization	17
3.3	Ferroelectric characterization	20
4	Epitaxial La-substituted $\text{Bi}_4\text{Ti}_3\text{O}_{12}$ thin films grown on (001)-, (011)-, and (111)-oriented SrTiO_3 single crystal substrates	22
4.1	Experiment	23
4.2	Results and discussion	23
4.2.1	Crystallographic orientations and epitaxial relationships	23
4.2.2	Surface morphology	30
4.2.3	Ferroelectric properties	32
4.3	Summary	34
5	Epitaxial growth of (104)-oriented rare-earth element-substituted $\text{Bi}_4\text{Ti}_3\text{O}_{12}$ thin films on silicon substrates using (111)-oriented Pt electrode layers	36
5.1	Experiment	37
5.2	Results and discussion	38
5.2.1	Growth of (111)-oriented Pt electrode layer	38
5.2.2	Ferroelectric La- and Nd-substituted $\text{Bi}_4\text{Ti}_3\text{O}_{12}$ thin films	43
5.3	Summary	58
6	Reducing azimuthal domains in epitaxial ferroelectric La-substituted $\text{Bi}_4\text{Ti}_3\text{O}_{12}$ films using miscut yttria-stabilized zirconia single crystal substrates	59
6.1	Experiment	61
6.2	Results and discussion	62
6.2.1	SrRuO_3 films on miscut YSZ(100) single crystal substrates	62
6.2.2	La-substituted $\text{Bi}_4\text{Ti}_3\text{O}_{12}$ films on SrRuO_3 -covered miscut YSZ(100) substrates	70
6.3	Summary	77
7	Well-ordered large-area arrays of epitaxial ferroelectric La-substituted $\text{Bi}_4\text{Ti}_3\text{O}_{12}$ nanostructures of (001), (118)/(100), and (104) orientations	78
7.1	Experiment	79
7.2	Results and discussion	81
7.2.1	Preparation of gold nanotube membranes	81
7.2.2	La-substituted $\text{Bi}_4\text{Ti}_3\text{O}_{12}$ nanostructures	82
7.3	Summary	91
8	Conclusions and future work	92
	Bibliography	95

Chapter 1

Introduction

The fabrication of epitaxial films involves the growth of a crystalline material on a single crystal substrate. The growing crystalline film possesses a specific orientation in relation to that of the substrate. Epitaxy has long been known in materials science but the deposition of epitaxial thin films has only become common with the help of improved vacuum systems. Advances in epitaxial thin film growth techniques have enabled the widespread use of epitaxial film growth as a method of materials fabrication for laboratory studies, and increasingly for industrial fabrication of electronic and optical devices. Oxide epitaxial films of numerous compositions are grown by various techniques, such as pulsed laser deposition (PLD), molecular beam epitaxy, chemical vapor deposition, and sputtering techniques.

Layered complex oxide materials have large unit cells which are composed of two or more types of atomic layers built up in a specific sequence along one or more crystal axes. These materials often have a highly anisotropic structure, with lattice parameters in the stacking direction (the c axis) of five or more times those of the a and b lattice parameters. Epitaxial growth can provide a viable route to the synthesis of layered complex oxides in chemically pure, epitaxial form, enabling investigations of the high anisotropy of their fundamental properties avoiding bulk synthesis methods. The latter can be complicated by processing limitations, including uncharted phase equilibria and incongruent phase transformations.

Ferroelectric films of bismuth-layered perovskite oxides, such as $\text{SrBi}_2\text{Ta}_2\text{O}_9$ (SBT) and lanthanum-substituted $\text{Bi}_4\text{Ti}_3\text{O}_{12}$ (BLT), are being extensively investigated for use in future high-density nonvolatile ferroelectric random access memory (NV-FRAM) systems due to their high fatigue endurance together with low processing temperatures (especially for BLT). Although commercial low-density memories made of polycrystalline films are already in use,

for high density memories in the gigabit range, the individual cells should have a lateral size below 100 nm. This size, however, corresponds also to the order to magnitude of the grain diameter in polycrystalline films. Therefore it is difficult to obtain uniform ferroelectric properties over the different cells (consisting of randomly oriented grains) within a large memory capacitor array. The use of uniformly oriented, i.e., epitaxial or epitaxially twinned, ferroelectric films is a suitable way to avoid nonuniformity problems in NV-FRAM systems. The integration of bismuth-layered perovskite materials into silicon-based microelectronics entails the growth of these materials on silicon substrates. This is most important for any practical application of these materials in actual memory devices.

In addition, it is necessary to understand whether and why bismuth-layered perovskite materials still have ferroelectric properties on a scale of below 100 nm. As ferroelectricity represents a cooperative phenomenon that depends on the interaction of neighboring permanent electric dipole moments in a crystal lattice, there is a size limit, known as superparaelectric limit, below which ferroelectricity vanishes. The chances for an application of bismuth-layered ferroelectric perovskite materials therefore also depend on the presence or absence of size effects like the superparaelectric limit.

During recent years, rare-earth-substituted bismuth titanate ceramics and thin films have been in the focus of international research. Many characteristics of these materials have been determined. Uniformly oriented thin films have, however, mainly been grown on ternary oxide-type, single-crystal model substrates of convenient lattice structure and lattice parameters. There is still a lack of data and of methods concerning growth, microstructure and properties of uniformly oriented, crystallographically rather perfect thin films of these materials on suitably electroded *silicon substrates* – the only substrates used in silicon-based technologies –, as well as on growth and physical characterization of *nanostructures* made from these materials. The present work concentrates on these issues. As materials of choice, lanthanum- and neodymium-substituted bismuth titanates (BLT and BNT) are considered, and PLD is used to achieve a well-controlled deposition of BLT and BNT thin films and nanostructures.

Chapter 2 describes the background and the significance of ferroelectric rare-earth-substituted $\text{Bi}_4\text{Ti}_3\text{O}_{12}$ materials for possible applications, such as nonvolatile memory devices. Epitaxial growth is introduced in brief, and the importance of and requirements for epitaxial growth of these materials are presented. **Chapter 3** is dedicated to the discussion of the deposition method and the characterization methods used in the present study.

To obtain a reference with respect to existing literature data, the growth by PLD of well-oriented BLT films on SrTiO_3 model substrates of different orientations is studied first (**Chapter 4**). In **Chapter 5**, a new electrode/epitaxial template/buffer layer system is developed, in part making use of (100)-oriented yttria-stabilized cubic ZrO_2 (YSZ) buffer layers on Si(100) known from literature. This new $\text{SrRuO}_3(111)/\text{Pt}(111)/\text{YSZ}(100)$ system is grown on Si(100) substrates and characterized with respect to its microstructure. It is then

utilized for the growth of uniformly non-*c*-axis-oriented ferroelectric BLT and BNT thin films on Si(100) substrates. The optimum deposition conditions are found, and crystallographic orientation, microstructure, surface topography, and ferroelectric properties of these films are characterized. Finally it is demonstrated that uniformly (104)-oriented BLT and BNT thin films on thus electroded and buffered Si(100) substrates have sufficiently good ferroelectric properties to be applied in silicon-based microtechnologies.

As part of the investigations, (100)-oriented yttria-stabilized cubic ZrO₂ (YSZ) buffer layers turned out to be essential. However, the fourfold symmetry of their surface together with the non-fourfold symmetry of the electrode layers leads to a multiply twinned structure of the electrodes and of the otherwise uniformly oriented BLT and BNT films. The latter thus involve a number of azimuthal domain variants and corresponding azimuthal domain boundaries. This is true for (100)-, (118)-, and (104)-oriented rare-earth-substituted Bi₄Ti₃O₁₂ thin films on electroded, YSZ(100)-buffered Si(100) substrates, irrespective of the different orientations of these films. Since the azimuthal domain boundaries are defects that may harm the ferroelectric properties, a study of azimuthal domain reduction in BLT films grown on YSZ(100) single crystal substrates is performed in **Chapter 6**, using vicinal miscut substrates. It is shown that the number of azimuthal domain variants in (100)- and (118)-oriented BLT films can be reduced by 50%, if well-annealed YSZ(100) substrates with suitable miscut parameters are used, and that the ferroelectric properties of the BLT films can be improved in this way.

Finally, regular large-area arrays of well-oriented BLT nanostructures of less than 150 nm lateral size are prepared by pulsed laser deposition in **Chapter 7**, applying metal nanotube membranes as shadow masks. Their crystallographic orientation is determined and their ferroelectric properties are studied. It is demonstrated that the individual cells of these large-area BLT nanostructure arrays retain their ferroelectric properties irrespective of their small volume and that they are thus principally suitable for ferroelectric memories of high memory density. Finally, in **Chapter 8** conclusions are given and future work is considered.

Chapter 2

Rare-earth element-substituted bismuth titanates

2.1 Rare-earth-substituted $\text{Bi}_4\text{Ti}_3\text{O}_{12}$ as a new class of ferroelectric materials

2.1.1 Ferroelectric random access memories

Ferroelectrics are materials that belong to the pyroelectric family, showing a spontaneous polarization in the absence of an external electric field, and within a certain range of temperatures and pressures. The direction of the polarization vector can be switched by an external field. Ferroelectric films can display a wide range of dielectric, ferroelectric, piezoelectric, electrostrictive, and pyroelectric properties. Recently, the potential utilization of these properties in a new generation of electronic devices has driven studies on the synthesis, characterization, and determination of processing-microstructure-property relationships of ferroelectric thin films.

Considerable attention has been paid to ferroelectric random access memories (FRAMs), which are non-volatile memory devices using ferroelectric thin films. Since they retain information when power is interrupted, they will constitute important computer components. The structure of FRAMs is quite similar to that of conventional dynamic random access memories (DRAMs) [1]. A DRAM cell includes a capacitor, where the binary information is stored in terms of the signs of the stored charge. To maintain this information, a voltage has to be periodically applied to compensate for charge reduction due to leakage currents. In the FRAM cell, the dielectric material in the DRAM capacitor cell is replaced with the ferroelectric thin film. Information can be stored in the polarization states of the ferroelectric thin film, namely two polarization states at zero electric field can be utilized as '0' and '1' digital states as shown in Fig. 2.1.

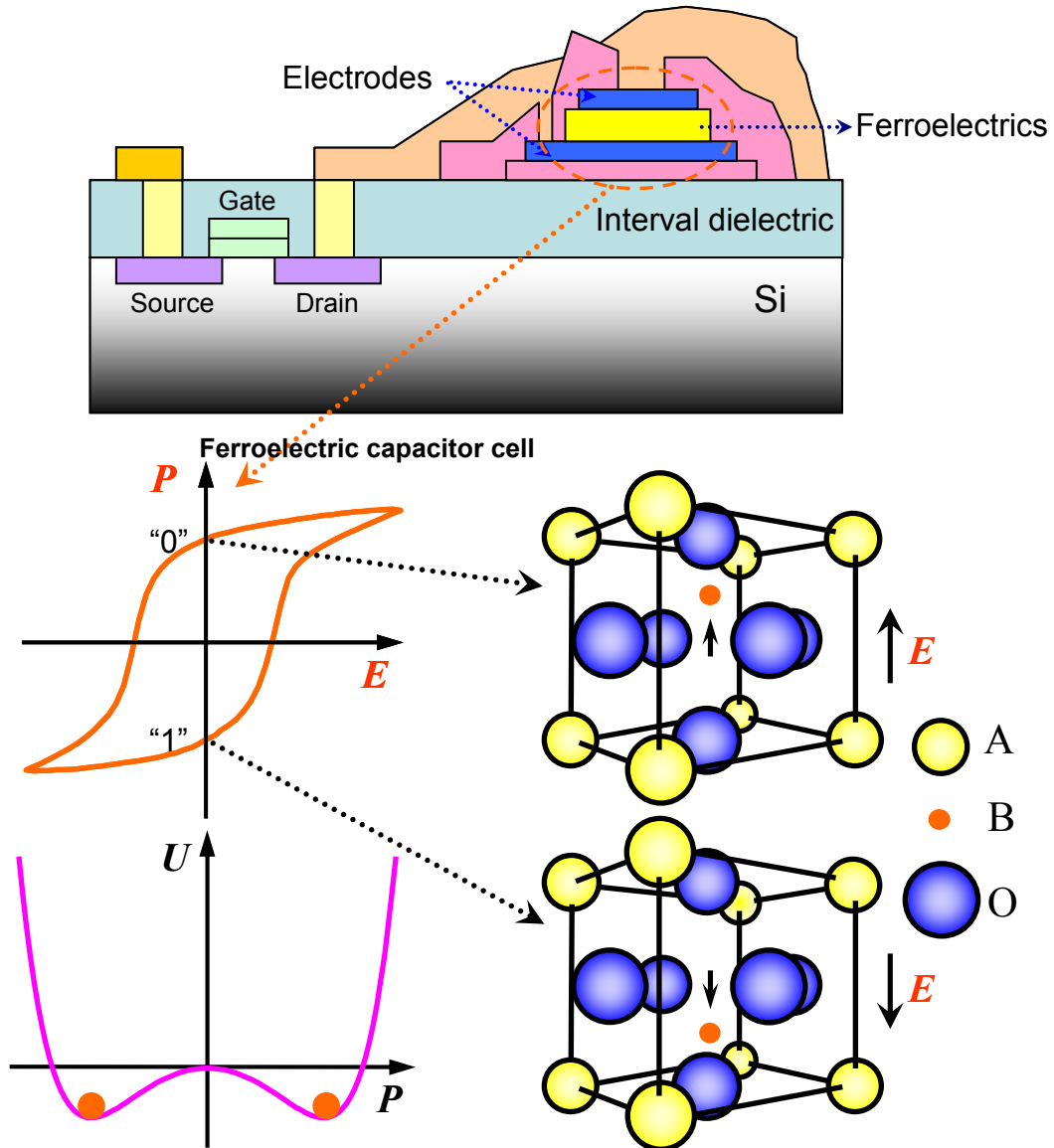


FIG. 2.1. Schematic diagram of a ferroelectric random access memory, typical ferroelectric hysteresis loop, and a unit cell of ABO₃ type perovskite structure. The spontaneous polarization in a ferroelectric arises from a noncentrosymmetric arrangement of ions in its unit cell, which result in an electrical dipole moment. Bottom left: Energy scheme showing two stable polarization states.

In principle, FRAMs should have a lower power consumption, a faster access time, and potentially lower costs than many other semiconductor memory devices. There have been numerous efforts to develop FRAMs during the last few decades [1,2,3,4], but their commercialization has been quite slow [5]. There have been a number of reasons for this slow commercialization. The material issues have been the most important. In order to realize a practical FRAM, ferroelectric thin films should satisfy the following criteria: (i) compatibility with current DRAM technologies, (ii) large remanent polarization (P_r), and (iii) good reliabilities of polarization cycling characteristics.

2.1.2 $\text{Pb}(\text{Zr}_x\text{Ti}_{1-x})\text{O}_3$ -based materials

One of the most conventional ferroelectric materials used in nonvolatile FRAM technology is $\text{Pb}(\text{Zr}_x\text{Ti}_{1-x})\text{O}_3$, known as PZT, due to its large remanent polarization values, low processing temperatures, and principal compatibility with silicon-based technology. As shown in Fig. 2.2(a), PZT-based materials have the perovskite structure. They usually show large values of $2P_r$: depending on substituting elements and processing conditions, reported values vary from 20 to 70 $\mu\text{C}/\text{cm}^2$ [6,7]. However, when the capacitor is fabricated with the PZT film on a conventional metallic Pt electrode, the polarization value is reduced after repetitive read/write cycles. This problem is called “*fatigue*”. It might be attributed to space charges resulting from defects inside the ferroelectric material [2,8]. It is also related, to a major extent, to phenomena occurring near the bottom and/or top electrode-ferroelectric interfaces [9,10]. These phenomena include the presence of oxygen vacancies and their action as charge trapping centers. In addition, internal interfaces in the PZT layer such as domain walls and grain boundaries influence the ferroelectric properties such as fatigue [11,12]. In order to overcome the fatigue, a modification of the electrodes has been suggested. Some researchers replaced the metallic Pt electrodes with electrically conducting oxide electrodes such as RuO_2 [13,14] and IrO_2 [15], with perovskite-type oxides such as $\text{YBa}_2\text{Cu}_3\text{O}_{7-\delta}$ (YBCO) [16] and $(\text{La},\text{Sr})\text{CoO}_3$ [17] or with hybrid metal-oxide electrodes [14,15,18,19]. The fatigue problem in PZT-based films can be reduced significantly in this way. However, these electrodes are more difficult to synthesize than pure metal electrodes [20]. Therefore, the search for new candidate materials exhibiting good fatigue endurance on Pt electrodes is essential.

2.1.3 Bismuth-layered perovskite materials

An alternative ferroelectric material that has emerged during the last ten years for FRAM application is $\text{SrBi}_2\text{Ta}_2\text{O}_9$ (SBT) [3]. It was found that SBT thin films or related oxides could overcome the fatigue problem even on metallic Pt electrodes. As shown in Fig. 2.2(b), SBT has a bismuth-layered perovskite structure where the double TaO_6 octahedron layers are sandwiched between the $(\text{Bi}_2\text{O}_2)^{2+}$ layers. It is well known that the $(\text{Bi}_2\text{O}_2)^{2+}$ layers make SBT fatigue free [3]: These layers have net electrical charges, so their positioning in the lattice becomes self-regulated to compensate for the space charges near the electrodes due to oxygen vacancies. However, SBT films have other shortcomings. They have relatively small $2P_r$ values, which vary from 4 to 16 $\mu\text{C}/\text{cm}^2$ [3,20,21,22,23]. In addition, a high processing temperature (750–850 °C) is usually required to deposit high-quality SBT films, which makes them difficult to be compatible with the current DRAM technologies.

Bismuth-layered perovskite materials are also called Aurivillius phases. The structure of

Aurivillius phases can be described as the intergrowth of fluorite-like $(\text{Bi}_2\text{O}_2)^{2+}$ units and perovskite $(\text{A}_{n-1}\text{B}_n\text{O}_{3n+1})^{2-}$ slabs, where $n=2, 3, 4$ and 5 [24]. The twelffold coordinated perovskite A sites can be occupied by divalent or trivalent cations such as Ba^{2+} , Ca^{2+} , Sr^{2+} , Bi^{3+} , and rare earth elements, and the sixfold coordinated B sites are usually occupied by smaller cations such as Ti^{4+} , Ta^{5+} , Nb^{5+} , and W^{6+} , leading to BO_6 octahedra [25].

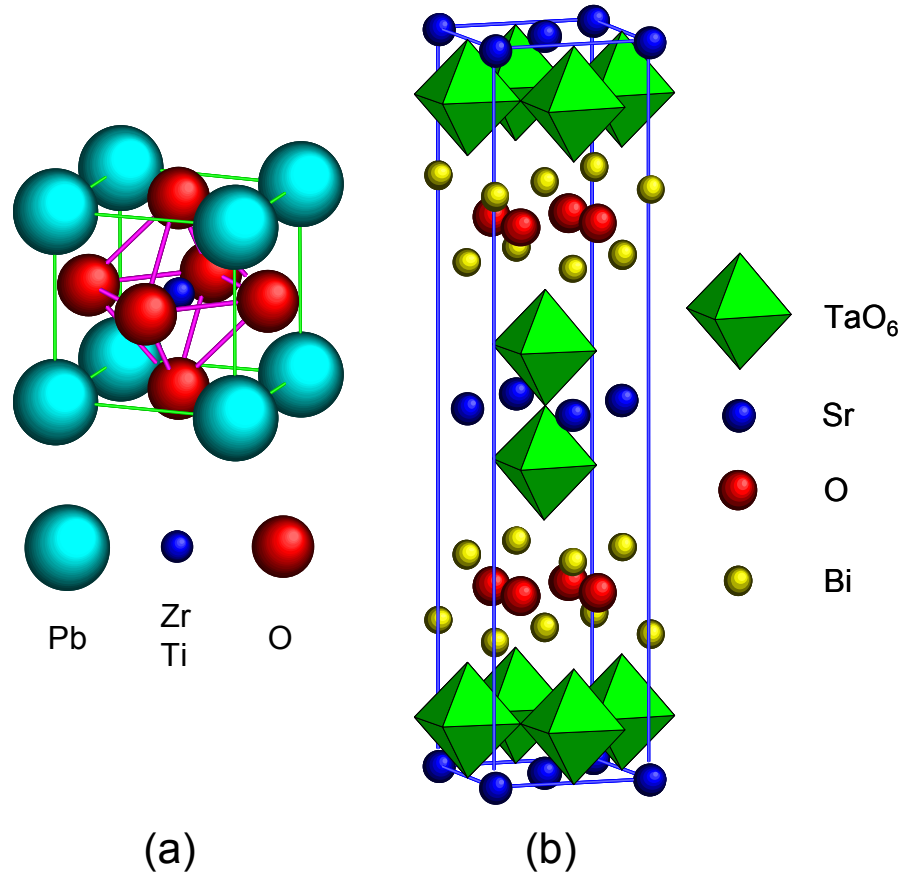


FIG. 2.2. Unit cells of two typical ferroelectric oxide crystals. (a) The cubic perovskite structure $[\text{Pb}(\text{Zr}_x\text{Ti}_{1-x})\text{O}_3]$ and (b) the bismuth-layered perovskite structure $(\text{SrBi}_2\text{Ta}_2\text{O}_9)$.

SBT and $\text{Bi}_4\text{Ti}_3\text{O}_{12}$ belong to the $n=2$ and 3 members of the Aurivillius family, respectively. The exact crystal structure of SBT has been determined by Rae *et al.* using single crystal and powder x-ray diffractometer data and electron diffraction. Due to their results, it crystallizes in the space group $A2_1am$ and has a orthorhombic structure, with lattice parameters $a=0.5531$ nm, $b=0.5534$ nm, and $c=2.4984$ nm [26]. Ferroelectric $\text{Bi}_4\text{Ti}_3\text{O}_{12}$ is monoclinic with the space group $B1a1$ but can be considered as pseudo-orthorhombic, with $a=0.545$ nm, $b=0.541$ nm, and $c = 3.283$ nm [27] as shown in Fig. 2.3.

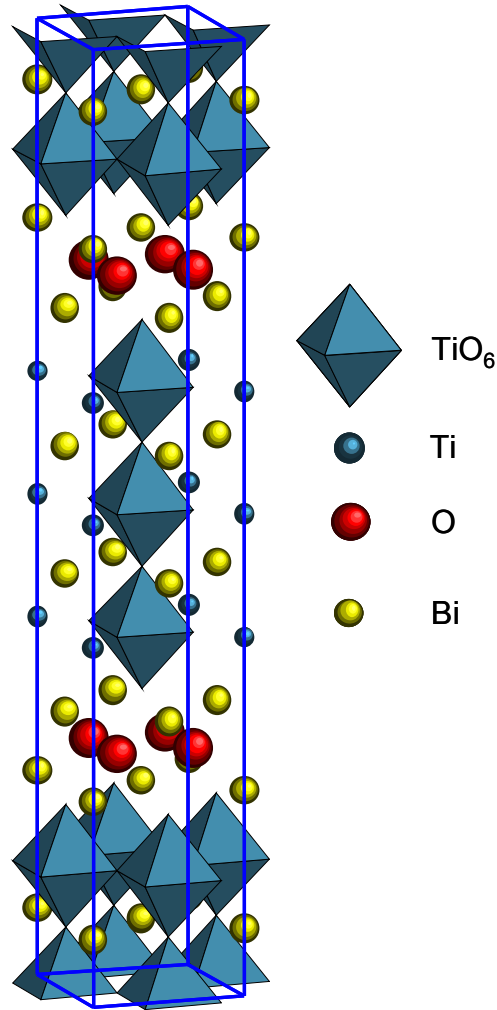


FIG. 2.3. Crystal structure of $\text{Bi}_4\text{Ti}_3\text{O}_{12}$.

In view of their large remanent polarization, $\text{Bi}_4\text{Ti}_3\text{O}_{12}$ single crystals could be good candidates for devices, since they show a large spontaneous polarization of $50 \mu\text{C}/\text{cm}^2$ along their crystallographic a axis [28]. However $\text{Bi}_4\text{Ti}_3\text{O}_{12}$ thin films showed severe fatigue failure in spite of the presence of the compensating $(\text{Bi}_2\text{O}_2)^{2+}$ layers [29,30,31].

2.1.4 Rare-earth element-substituted $\text{Bi}_4\text{Ti}_3\text{O}_{12}$

In 1999, Park *et al.* presented La-substituted $\text{Bi}_4\text{Ti}_3\text{O}_{12}$ ($\text{Bi}_{4-x}\text{La}_x\text{Ti}_3\text{O}_{12}$) films as a promising candidate material for FRAM applications [32]. They deduced that the substitution with lanthanum led to an improved oxygen ion stability in the $\text{Bi}_4\text{Ti}_3\text{O}_{12}$ lattice and therefore improved the fatigue endurance, because some of the Bi ions in the pseudoperovskite layers containing TiO_6 octahedra are preferentially substituted by La ions [33]. Moreover, they chose $\text{Bi}_{3.25}\text{La}_{0.75}\text{Ti}_3\text{O}_{12}$ (BLT, $x=0.75$), since BLT with $x=0.75$ shows the largest remanent polarization value among various La-modified $\text{Bi}_4\text{Ti}_3\text{O}_{12}$ materials [34]. BLT ($x=0.75$) films also showed a high fatigue endurance. In addition, these films can be deposited at

temperatures as low as 650 °C, and their remanent polarization values ($2P_r$) of $\sim 24 \mu\text{C}/\text{cm}^2$ were larger than those of SBT films. However the substitution of the Bi^{3+} cation with the La^{3+} cation reduces the structural distortion of the octahedra in the perovskite block in such a way as to cause a decrease of the spontaneous polarization compared to non-substituted $\text{Bi}_4\text{Ti}_3\text{O}_{12}$ [35].

It has also been proposed to substitute the Bi in $\text{Bi}_4\text{Ti}_3\text{O}_{12}$ by other lanthanide elements such as Nd, Sm, and Pr. These elements are of interest because the extent of enhancement of the spontaneous polarization in $\text{Bi}_4\text{Ti}_3\text{O}_{12}$ and other bismuth-layered perovskite oxides is also dependent upon structural distortion. For these materials the rotation of TiO_6 octahedra in the a - b plane accompanied by a tilt of the octahedra from the c axis is largely enhanced by the lanthanides substitution on the Bi site in the perovskite layer [27,35]. Therefore, the substitution on the Bi site by other lanthanides with smaller ionic radius than that of La is expected to increase the spontaneous polarization. The ionic radii of these elements for a coordination number of eight are 0.117 nm for Bi^{3+} , 0.116 nm for La^{3+} , 0.111 nm for Nd^{3+} , 0.108 nm for Sm^{3+} , and 0.113 nm for Pr^{3+} . It can be deduced from these data that the substitution by Nd will lead to a larger distortion than the substitution by La doping and should, in principle, result in a larger spontaneous polarization. This has also been proven experimentally by studies comparing the effects of substitution of $\text{Bi}_4\text{Ti}_3\text{O}_{12}$ with various lanthanide elements [36,37,38,39]. Chon *et al.* [37] reported very high values of the remanent polarization in sol-gel processed, Nd-modified $\text{Bi}_4\text{Ti}_3\text{O}_{12}$ ($\text{Bi}_{4-x}\text{Nd}_x\text{Ti}_3\text{O}_{12}$: BNT) films which can thus be prime candidates for FRAM applications. However, most of the above studies were conducted on films prepared by a chemical solution route and thus the films had a polycrystalline structure. In order to clarify the effect of the lanthanide substitution, investigations using epitaxial films with identical orientation are essential because the ferroelectric properties of these materials strongly depend on the film orientation.

2.2 Epitaxial growth of Bi-layered perovskite oxides – achievements and problems

Besides the effect of substitution on the ferroelectric properties discussed in Section 2.1, the film orientation has a significant influence on the film properties. This section focuses on the epitaxial growth of bismuth-layered perovskite materials, considering their highly anisotropic structure. The growth of single crystals often represents the first key step in probing the fundamental properties of a highly anisotropic material. Bulk synthesis methods, although the most direct way to this purpose, can often be complicated by processing limitations, including uncharted phase equilibrium and incongruent phase transformation. In many of these cases, epitaxial growth of thin films offers a viable alternative. However, the growth of epitaxial thin films has also its own complications. For example, the substrate

choice is critical for a successful growth; substrates must be chemically compatible and closely lattice matched to the film. Additionally, the study of ferroelectrics and dielectrics generally entails the growth of an underlying epitaxial electrode. For many of the ferroelectrics that have received considerable attention recently, such as those of the Bi-layered perovskite materials SBT and $\text{Bi}_4\text{Ti}_3\text{O}_{12}$ (including lanthanide-substituted $\text{Bi}_4\text{Ti}_3\text{O}_{12}$), lattice match and chemical compatibility with a number of substrates and electrode candidates have been demonstrated.

2.2.1 Epitaxy

Two ancient Greek words, $\varepsilon\pi\iota$ (*epi*) meaning placed or resting upon and $\tau\alpha\zeta\iota\zeta$ (*taxi*) meaning arrangement, are the root of the modern word epitaxy which refers to the process of atom-by-atom growing complex structures onto the surface of a substrate. *Epitaxy* or *epitaxial growth* refers to extended single crystal material, e.g., a thin film, on the surface of a single-crystal substrate, and including a specific crystallographic orientation relationship between the film and the underlying substrate. The specific orientation of the film is significantly influenced by that of the substrate as a result of some degree of matching between the two along the interface. Two types of epitaxy can be distinguished and each has important scientific and technological implications, viz., *homoepitaxy* and *heteroepitaxy*. *Homoepitaxy* is the simplest form of epitaxy and refers to the case where the film and the substrate are of identical material. Epitaxial Si deposited on Si wafers is the most significant example of homoepitaxy. The second type of epitaxy is known as *heteroepitaxy* and refers to the case where films and substrates consist of different materials, e.g., Ge deposited on Si. In practice, heteroepitaxy is the most general form of epitaxy in various technological applications such as semiconductors, superconducting devices, ferroelectric memories, or optoelectronic devices. The fundamental criterion for epitaxy is defined by the lattice mismatch, f , in the atomic periodicities of the two materials along the interface, which can be written as

$$f = \frac{(d_{\text{film}} - d_{\text{sub}})}{(d_{\text{film}} + d_{\text{sub}})/2} \approx (d_{\text{film}} - d_{\text{sub}})/d_{\text{sub}} \quad (2.1)$$

where d_{film} and d_{sub} stand for the atomic spacings along some direction in the film and in the substrate.

2.2.2 Substrate choice

One of the most important factors affecting epitaxy is the nature of the substrate. For the epitaxial growth of films the substrate should be a single crystal substrate. The choice of substrate is limited by various factors, such as crystal symmetry, orientation, minimum lattice parameter mismatch, surface energy consideration, surface termination, chemical nature, thermal expansion coefficient, and most importantly the application for which the film is being deposited. The growth of high-quality epitaxial materials requires that the substrates have structural and chemical compatibility with the desired film. Chemical incompatibility can lead to a variety of interfacial reaction layers or interdiffusion of unwanted elements between the film and the substrate. Structural incompatibility, typically manifested through substrate lattice parameters with very different values from the film, or large differences in thermal expansion between the film and substrate, can have a significant effect on the structural and electrical properties of the film. Structural defects, including dislocations, cracking, or even a complete loss of epitaxy are common when the film and substrate are not well lattice matched. In addition, several experimental and theoretical studies have shown that strain can have a significant influence on the electrical properties of dielectric, ferroelectric, and superconducting thin films. For example, (i) shifting of the Curie temperature in ferroelectric $\text{Ba}_{1-x}\text{Sr}_x\text{TiO}_3$ and BaTiO_3 [40], (ii) introduction of ferroelectricity and improved dielectric tunability in SrTiO_3 grown on DyScO_3 [41], (iii) enhancement of ferroelectricity in fully strained $\text{SrRuO}_3/\text{BaTiO}_3/\text{SrRuO}_3$ capacitors grown on GdScO_3 and DyScO_3 [42], and (iv) increasing the superconducting transition temperature in $(\text{La,Sr})_2\text{CuO}_4$ [43] have all been observed. Clearly, the characterization of the intrinsic properties of thin films without consideration of their strain state is not possible.

The choice of the substrate is also important when an epitaxial growth of Bi-layered perovskite oxides is desired. Due to their highly anisotropic structure, epitaxial thin films of these materials can easily be grown with the [001] axis parallel to the film normal, i.e., in the so-called *c*-axis orientation, particularly when grown on (001)-oriented perovskite substrates, such as $\text{LaAlO}_3\text{-Sr}_2\text{AlTaO}_6$ (LSAT), SrTiO_3 , and LaAlO_3 [44,45,46]. However, *c*-axis-oriented bismuth-layered perovskite films do (almost) not have a polarization component along the film normal, because the vector of the (major) spontaneous polarization in these layered perovskite materials lies (almost) entirely in the *a*-*b* plane and specifically is (almost) directed along only the crystallographic *a* axis. The challenge in studying the anisotropy of these compounds thus lies in growing films with orientations in which some component of the *a* axis is perpendicular to the substrate surface. Among perovskite single crystal substrates, SrTiO_3 single crystals have been used as substrates to grow a number of epitaxial thin films of perovskite-type ferroelectrics. SrTiO_3 has a cubic structure with the space group *Pm3m* and the lattice parameter $a=0.3905$ nm at room temperature. In particular, SrTiO_3 single crystal substrates with (011) and (111) orientations are very useful for growing non-*c*-axis-oriented

Bi-layered perovskite films, resulting in a non-zero component of the vector of spontaneous polarization normal to the substrate. In other words they permit to have a large angle between the c axis of the film and the substrate normal.

2.2.3 Electrode choice

Pure conducting metal electrodes have been the most popular choice for ferroelectric thin films due to the easy deposition. Among many pure metals, only a few noble metals such as Pt, Au, and Ag can be used as electrodes in practical processing, because other metals show instabilities at elevated temperatures in oxygen. However Au and Ag react with many ferroelectric materials during their processing. This is the reason why Pt is the mostly viable choice for electrodes. Pt has been extensively used as the bottom electrode for ferroelectric thin films. It has mostly been deposited on Si substrates using buffer layers of SiO₂ or Ti/SiO₂. Pt has been deposited mainly by sputtering and e-beam evaporation. Usually Ti has been used as an intermediate layer to improve the adhesion between Pt and the SiO₂ layer. However Pt electrodes on Ti/SiO₂/Si substrates have some drawbacks, such as the formation of hillocks in the Pt films due to stress relief which can lead to capacitor shorting and Pt/Ti interactions leading to alloy or compound formation. Moreover, these Pt-coated Si substrates are not suitable for growing epitaxial films of Bi-layered perovskite oxides due to the fiber-textured character of the Pt electrodes: When Bi-layered perovskite films are deposited on such Pt-coated Si substrates, they are usually polycrystalline or textured, or (001)-oriented at best [47].

The desire to grow a variety of perovskite ferroelectric materials on an epitaxial conducting electrode has led to the extensive investigation of SrRuO₃. Many perovskite oxide electrodes such as (La,Sr)₂CuO₄, (La,Sr)CoO₃, SrRuO₃, and Sr₂RuO₄ have been tested. Their choice also depends on the underlying perovskite-type single crystal substrate due to lattice mismatch. Among these conducting perovskite electrodes, SrRuO₃ is very promising, since it is electrically conductive, and structurally well lattice matched with (and chemically compatible when in contact with) most perovskite-type oxides [48]. With these superior properties, SrRuO₃ is expected to serve as a good starting layer in various perovskite oxide-based devices. Moreover, if grown with sufficiently high quality, it may permit full monolithic integration of crystalline oxides into complex silicon-based devices. SrRuO₃ crystallizes in an orthorhombically distorted perovskite-type structure with the space group $Pbnm$ and the lattice parameters $a = 0.553$ nm, $b = 0.557$ nm, and $c = 0.785$ nm at room temperature [49]. Owing to the only small distortions in the arrangement of the RuO₆ octahedra, it can be regarded as a pseudo-cubic perovskite with a lattice parameter of $a_f = 0.393$ nm. Pseudocubic indexing is used for SrRuO₃ throughout this thesis. In addition, SrRuO₃ has a paramagnetic-to-ferromagnetic phase transition at 160 K [50], a relatively large remanent magnetization and a large magneto-optic constant which make it potentially attractive for various electronic

and optic devices [51]. Epitaxial thin films of SrRuO₃ have been grown by various deposition techniques such as off-axis sputtering [48], pulsed laser deposition (PLD) [52,53,54], metal organic chemical vapor deposition [55] and electron beam evaporation [56] on SrTiO₃ and LaAlO₃ substrates. These epitaxial thin films have been shown to be excellent electrodes for the growth of several ferroelectric compounds, including BaTiO₃ and Pb(Zr,Ti)O₃. In addition, SrRuO₃ has been shown to significantly reduce the fatigue failure in these materials like other oxide electrodes [57], a serious advantage over metal electrodes. Epitaxial integration of SrRuO₃ with silicon would provide an ideal conducting template for the subsequent growth of ferroelectrics.

2.2.4 Integration with silicon

Since oxide single crystals are not suitable as substrates in silicon-based microelectronics, epitaxial ferroelectric thin films should be grown on silicon substrates. First of all, various attempts to integrate the functional properties of crystalline oxides with silicon have led to the development of various innovative growth techniques.

The first epitaxial growth of ferroelectric perovskite materials grown on silicon substrates was reported using MgAl₂O₄ spinel buffer layers for the subsequent growth of PbTiO₃ [58]. In 1991, the epitaxial growth of BaTiO₃ thin films was reported on Si(100) substrates with the use of a BaO/BaSi₂ buffer layer [59]. In particular, perovskite SrTiO₃ or La-doped SrTiO₃ films have been epitaxially grown on silicon substrates by MBE [60,61]. The epitaxial SrTiO₃ layers served as an effective template to grow epitaxial GaAs on Si [62] and for the growth of a variety of ferroelectric compounds on Si with underlying electrode layers [63,64].

The use of SrTiO₃ as a buffer layer or epitaxial template is restricted by its insulating properties: Many applications, especially ferroelectric thin films, require a conducting buffer layer or a conducting epitaxial template, which can be used as bottom electrode. Epitaxial conducting perovskite electrodes such as SrRuO₃ and La_{0.5}Sr_{0.5}CoO₃ have been grown with a (001) orientation on (100)-oriented Si substrates using epitaxial template layers of SrTiO₃ or La-doped SrTiO₃. The (001) orientation of SrRuO₃ or La_{0.5}Sr_{0.5}CoO₃ is very useful for growing *c*-axis-oriented simple perovskite ferroelectrics, such as Pb(Zr_{1-x}Ti_x)O₃ and BaTiO₃. Their vector of spontaneous polarization is entirely directed along the *c* axis. On the other hand, bismuth-layered perovskite oxides, such as SBT and BLT, have been grown on (001)-oriented SrRuO₃ with *c*-axis orientation, showing a negligible remanent polarization component perpendicular to the film plane. Accordingly, for the epitaxial growth of non-*c*-axis-oriented SBT and BLT films on Si(100) substrates, non-(001)-oriented SrRuO₃ films are required as bottom electrodes, in this way obtaining a non-zero polarization component perpendicular to the film plane. However, attempts to grow SrRuO₃ directly on silicon have

resulted in a variety of interfacial reactions usually resulting in the growth of a polycrystalline SrRuO₃ film [65].

2.2.5 Growth of Bi-layered perovskite films on silicon substrates

Yttria-stabilized zirconia (YSZ) has proved to be an attractive buffer layer for the subsequent growth of numerous oxide materials on non-oxide substrates. In particular, epitaxial YSZ buffer layers grown on Si(100) substrates were used to grow non-*c*-axis-oriented epitaxial films of Bi-layered perovskite materials [66]. It has a cubic structure with a lattice parameter from 0.514 to 0.523 nm depending on its Y₂O₃ content. In this thesis, YSZ with 9 mol % of Y₂O₃ was used both as a single crystal substrate and a buffer layer on Si(100) substrates, exhibiting a lattice parameter of $a=0.514$ nm. The epitaxial growth of YSZ has been achieved by PLD both on hydrogen terminated silicon surfaces [67] and silicon substrates without chemical removal of the native oxide [68]. Several studies suggest that a thin SiO₂ layer on top of the Si surface favors the high-quality epitaxial growth of YSZ. It is assumed that the impinging zirconia atoms reduce the SiO₂ to Si, which epitaxially crystallizes on the substrate, enabling ZrO₂ epitaxy. Epitaxial SrRuO₃ films with (110) orientation have been grown on Si(100) substrates with these (100)-oriented YSZ buffer layers [69]. Epitaxial thin films of Bi-layered perovskite materials grown on the (110)-oriented SrRuO₃ bottom electrode YSZ(100)/Si(100) substrates showed ferroelectric hysteresis loops revealing their anisotropic properties [70,71]. Lee *et al.* reported that uniformly *a*-axis-oriented, epitaxially twinned BLT thin films having the spontaneous polarization entirely normal to the film surface were grown on (100)-oriented YSZ buffered Si(100) substrates covered with very thin (110)-oriented SrRuO₃ electrode layers [71]. Chapter 5 of this thesis investigates the growth of (104)-oriented lanthanides-substituted Bi₄Ti₃O₁₂ thin films grown on YSZ(100) buffered Si(100) substrates covered with SrRuO₃(111)/Pt(111) layer. The (111)-oriented Pt films grown on the YSZ(100)/Si(100) substrates provide template layers for the subsequent growth of non-*c*-axis-oriented Bi-layered perovskite oxides.

Chapter 3

Experimental details

3.1 Deposition techniques

In this thesis, pulsed laser deposition was used for the preparation of various complex-oxide thin films, whereas platinum electrodes were deposited by magnetron sputtering.

3.1.1 Pulsed laser deposition

Several thin film growth techniques capable of a well-controlled deposition of materials have been developed. One of the most versatile approaches to oxide film growth is pulsed-laser deposition (PLD) which is convenient and efficient. Although the significant development of this technique began only in the late 1980s, PLD is now a widely used deposition approach for film deposition, particularly in oxide compound research. Since the success of PLD in the growth of epitaxial high transition-temperature (T_C) $\text{YBa}_2\text{Cu}_3\text{O}_{7-x}$ superconducting films [72], this technique was popularized as an oxide film growth technique. In this technique, shown schematically in the left part of Fig. 3.1, a pulsed laser beam is focused onto a target surface of the material to be deposited. For sufficiently high laser energy density, each laser pulse vaporizes or ablates a small amount of the material. The ablated material is ejected from the target in a forward-directed plume which is always normal to the target surface irrespective of the angle of laser beam incidence. The ablation plume provides the material flux for film growth. Most commonly, UV excimer lasers such as F_2 (with a wavelength of 157 nm), ArF (193 nm), KrCl (222 nm), KrF (248 nm), XeCl (308 nm), and XeF (351 nm) are employed and the wavelength of the laser is tuned by the lasing gas composition. The KrF composition has been most dominantly employed due to its high energy-laser pulse output.

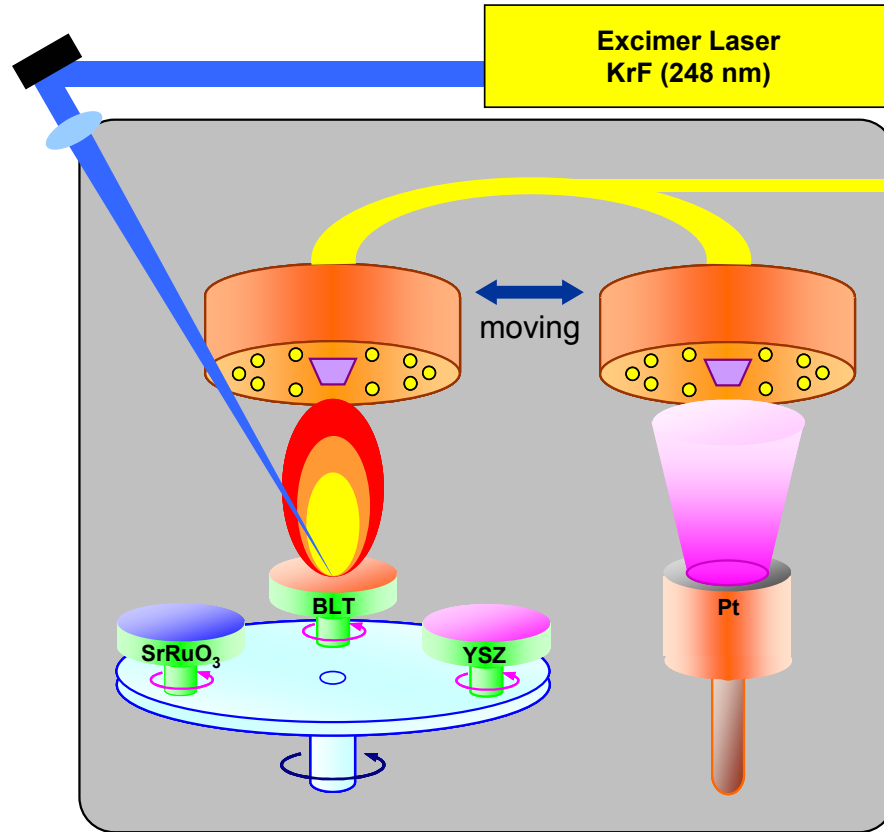


FIG. 3.1. Schematic diagram of the vacuum chamber involving pulsed laser deposition (left-hand side) and rf sputtering (right-hand side) systems, used in the present work.

PLD has several attractive features, including the stoichiometric transfer of material from the target, generation of energetic species, hyperthermal reaction between the ablated cations and molecular oxygen in the ablation plasma, and compatibility with background pressures ranging from ultra high vacuum (UHV) to 100 Pa. Among them, the most important and enabling characteristic of the PLD process is the ability to realize a stoichiometric transfer of the ablated material from a multi-cation target for many materials, in this way achieving a composition of the film that is almost identical with that of the target, even though the target involves a complex stoichiometry. Moreover, the ability to easily vary the deposition rate is one of the principal features of PLD compared to other physical vapor deposition methods such as the sputtering technique. In laser ablation, each laser pulse typically results in a material transfer sufficient for the deposition of only a sub-monolayer of the desired phase. The amount of film growth per laser pulse depends on multiple factors, such as target-substrate separation, background pressure, and laser energy density. Typically, the deposition rate per laser pulse is of the order of 10^{-4} to 0.1 nm per pulse. As such, PLD allows for a laser shot-to-shot control of the deposition process that is ideal for multilayer and interface formation where sub-monolayer control is needed. The PLD technique has been extremely successful for growing many functional oxide thin films, such as high- T_C superconducting,

ferroelectric, and ferromagnetic materials. For details of thin film deposition by PLD, see Ref. 73.

3.1.2 Magnetron sputtering

Sputtering is one of the effects occurring in a glow discharge, resulting in a surface being bombarded by energetic particles. In this process the target atoms travel through the plasma and undergo many collisions with the plasma species (electrons, neutrals, gas ions, and metal ions) and subsequently are deposited on a substrate. The substrate can be heated depending on the nature of the deposition. Sputtering processes can employ dc or rf power depending on the electrical conductivity of the target. DC power can be used only for conducting targets, whereas rf power can be used for both conducting and insulating targets. Usually a magnetic field (use of magnetron gun) is employed to enhance the efficiency of plasma utilization and the sputter efficiency. This happens due to the increased electron residence time in the plasma, improving the ion collision probability and thus resulting in larger discharge currents. The sputtering process using a magnetron is called magnetron sputtering. Details of magnetron sputtering are described in Ref. 74.

3.2 Structural characterization

3.2.1 X-ray diffraction

Epitaxial thin films are structurally characterized by various different methods and some of the most commonly used techniques are x-ray diffraction, transmission electron microscopy, and scanning force microscopy. Among them, four-circle x-ray diffraction is an extremely useful technique for determining the characteristics of the crystallographic structure of epitaxial thin films or films with a high degree of orientation. In addition to the standard two circles (ω and 2θ) found in a typical powder diffraction apparatus, the four circle tool has two additional degrees of freedom represented by the angular designations ϕ and ψ . Figure 3.2 shows a schematic of the four circle geometry [75]. While the ω and 2θ circles enable probing of the crystalline planes in a film parallel to the surface of the substrate, the ϕ and ψ circles allow probing of reflections and planes that are not parallel to the substrate surface. Unlike a randomly oriented powder or a randomly oriented film, an epitaxial film displays a much lower symmetry where sets of diffraction planes occupy unique positions in geometric space. Probing these reflections provides a wealth of information not apparent through studying planes probed in a θ - 2θ scan alone. In this thesis, a PANalytical X'Pert MRD four-circle diffractometer with Cu K_α radiation ($\lambda=0.154$ nm) was used.

A θ - 2θ scan (run at $\psi=0^\circ$ and termed an “on-axis scan”) is a scan where the ω and 2θ circles are moved simultaneously through angular space. As with any other diffraction process, when the Bragg condition is satisfied, diffraction events occur. Noting the specific angles at which this Bragg condition is satisfied provides information concerning the interatomic spacing of the planes parallel to the surface of the substrate. Peak position, peak shape, and peak width provide quantitative information concerning the out-of-plane lattice constant, film strain (coherency or incoherency), out-of-plane disorder along the film and substrate normal direction, film thickness, phase purity, and out-of-plane crystallographic orientation.

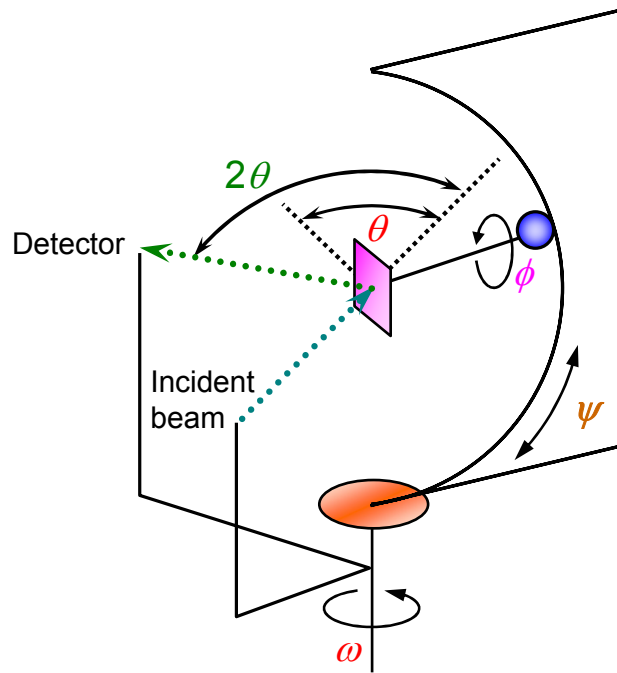


FIG. 3.2. Schematic showing the geometry and angular relationships for a four circle diffraction setup.

The second type of scan employed in this thesis, termed an ω scan or a rocking curve, is one where the sample is moved to the angular position to satisfy the Bragg condition ($n\lambda = 2d\sin\theta$) for a specific reflection and the sample is swept through the ω angular space while the detector (2θ) is kept fixed.

The third type of scan employed in this thesis, termed a ϕ scan, is one where the sample is moved to the angular position to satisfy the Bragg condition for a specific reflection, and a set of planes not parallel to the surface of the substrate (at an “off-axis position” or where ψ no longer is equal to 0°) is swept through the ϕ angular space while all other angles are kept fixed. This scan reveals information about in-plane alignment, quantitative data concerning the in-plane mosaic spread of the film, and the symmetry of a given set of reflections.

Although several θ - 2θ scans and ϕ scans are sufficient in order to determine and to confirm the film orientation with respect to the substrate orientation, it is rather difficult to

determine whether the film has also other minor orientations, which can not be distinguished in a θ - 2θ scan, e.g., because of a relatively weak peak intensity or because of an overlap of film peaks with substrate peaks. Therefore, ϕ scans are needed at all ψ angles (from 0° to 90°). The result is a pole figure at a certain 2θ angle providing a chance to see other possible orientations and also to confirm the film orientation which was determined previously by recording the θ - 2θ scan. During the pole figure measurement, the θ angle is fixed for a chosen direction of the film, and angles ϕ and ψ are varied. All pole figures were plotted with the pole distance angle from $\psi = 0^\circ$ (center) to $\psi = 90^\circ$ (rim). $\psi = 90^\circ$ corresponds to the substrate surface being parallel to the plane defined by the incident and reflected x-ray beams. The full width at half maximum (FWHM) values of the film used in the present study were calculated from both rocking curves and ϕ scan curves, comparing them with the FWHM of the substrate in order to evaluate the crystallinity and the in-plane alignment, respectively. This gives information about the “mosaicity” of the film. Details about thin film characterization by XRD can be found in Ref. 76.

3.2.2 Transmission electron microscopy

Transmission electron microscopy (TEM) is an important standard technique to characterize the microstructure of the film, i.e., the orientation relationship between the film and the substrate, and to visualize lattice defects like, e.g., misfit dislocations at the interface, stacking faults, twins, and antiphase boundaries. In this thesis, in order to investigate epitaxial thin films in both plan-view and cross section geometry using electron diffraction patterns, bright-field, and dark-field images, a Philips CM20T electron microscope was employed at a primary beam energy of 200 keV. It provided information on the orientation relationship with respect to the underlying substrate as well as on details of the morphology and microstructure of the films and interfaces involved.

Both cross-sectional and plan-view specimens of samples are prepared by polishing and ion milling techniques. For cross-sectional specimens, the sample is cut into thin slices normal to the interfaces which are glued face-to-face. After the glue has cured, disks with a diameter of 3 mm are obtained by cutting away the redundant epoxy. These disks are then ground, dimpled, and polished, followed by Ar-ion milling. Plan-view samples are prepared cutting disks with a diameter of 3 mm using an ultrasonic cutter. Then these disks are ground, dimpled, and finally thinned to perforation from the substrate side. Details on TEM methodology and sample preparation can be found in Ref. 77.

3.2.3 Atomic force microscopy

Atomic force microscopy (AFM) is a useful method for the study of topographic surface features of epitaxial thin films, which also provides an indirect insight into the growth process. AFM is a local surface probing technique in the sense that individual grains are visualized, not relying on long range order. The operation of an AFM is based on the detection of a low power laser beam reflected by the edge of a soft cantilever. The cantilever is typically made of Si as the tip material and oscillates in free air at its resonant frequency. An AFM can operate in principal modes, viz., tapping (non-contact) mode and contact mode. The tapping mode operation is of advantage to investigate the sample surface state without its modification, whereas the contact mode is used to add or remove atoms to or from the sample surface or in cases where an electrical field, a voltage or a current shall be applied to the sample. There is also preference in using the tapping mode in order to record images of better resolution.

In this study, an AFM (Digital Instruments D5000) with an ultrasharp tip was used in order to perform morphological studies of epitaxial films (including grain size and arrangement) and roughness measurements of the grown films. AFM was operated in the tapping mode. The silicon tip is mounted on a flexible cantilever and scans across the sample surface. The tip height is maintained using a piezoelectric crystal in order to maintain a constant vibrating amplitude which is equivalent to a constant distance between the tip and the sample surface. The changes in voltage applied to maintain this constant distance are converted into a signal indicating the topographical variation of the sample surface when it is scanned by the tip. Details about AFM can be found in Ref. 78.

3.3 Ferroelectric characterization

Global ferroelectric polarization–electric field (P – E) hysteresis loops and fatigue endurance were recorded to evaluate the ferroelectric properties of epitaxial thin films using the TF Analyzer 2000 ferroelectric tester (AixACCT) with triangular pulse sequences at 100 Hz. For details of macroscopic ferroelectric characterization techniques, see Ref. 79.

The understanding of local properties of materials at the nanometer level is of high importance for both fundamental scientific interest and electronic devices. For this purpose, one of the most promising approaches are scanning force microscopy (SFM) techniques that enable local property measurements and device characterizations on the nanoscale. Among different SFM techniques, the most useful method for nanoscale investigations of ferroelectric materials is piezoresponse force microscopy (PFM). The PFM technique is based on the detection of local vibrations of a cantilever induced by a probing ac signal applied between the conducting tip of a SFM and the bottom electrode of a ferroelectric sample. The cantilever vibrations are converted into an electrical signal by the position sensitive detector of the SFM

and extracted from the global deflection signal using a standard lock-in technique. This electrical signal representing the cantilever vibrations is referred to as the piezoresponse signal. The out-of-plane piezoresponse signal is extracted from the z deflection signal given by the detector electronics, and represents the local oscillations perpendicular to the plane of the sample surface. Similarly, if the piezoresponse signal is obtained from the x deflection signal, then it represents the oscillations of the surface perpendicular to the cantilever, in the plane of the film, and is referred to as in-plane piezoresponse signal. In general, the out-of-plane piezoresponse signal is directly related to the out-of-plane component of the local spontaneous polarization. More exactly, a high piezoresponse signal is implicitly associated with a large value of z component of the polarization, whereas a zero piezoresponse signal is attributed to the absence of polarization normal to the film surface.

In this thesis, a commercial scanning probe microscope (Autoprobe CP Research, Veeco) working in contact mode and a lock-in amplifier (EG&G Instruments, model 7260) were employed to measure the local mechanical oscillations induced by a small ac voltage applied to a conducting tip and the bottom electrode of the sample. Details of PFM characterization of ferroelectric thin films can be found in Ref. 80.

Chapter 4

Epitaxial La-substituted $\text{Bi}_4\text{Ti}_3\text{O}_{12}$ thin films grown on (001)-, (011)-, and (111)-oriented SrTiO_3 single crystal substrates

Randomly oriented polycrystalline ferroelectric thin films of bismuth-layered perovskites, such as $\text{SrBi}_2\text{Ta}_2\text{O}_9$ (SBT), $\text{Bi}_4\text{Ti}_3\text{O}_{12}$ or $\text{Bi}_{3.25}\text{La}_{0.75}\text{Ti}_3\text{O}_{12}$ (BLT), have been extensively investigated both in view of their fundamental properties and for their possible application to nonvolatile ferroelectric random access memory (NV-FRAM) systems due to their high fatigue endurance [3,32]. Particularly BLT is a very attractive candidate for use in ferroelectric microelectronic devices because it has remarkable advantages in terms of rather low processing temperatures and high remanent polarization. These bismuth-layered perovskite materials have a very anisotropic structure, namely, SBT (orthorhombic): $a=0.5531$ nm, $b=0.5534$ nm, and $c=2.4984$ nm [26], $\text{Bi}_4\text{Ti}_3\text{O}_{12}$ (pseudo-orthorhombic): $a=0.545$ nm, $b=0.541$ nm, and $c=3.283$ nm [27], and BLT: $a=0.542$ nm, $b=0.5415$ nm, and $c=3.289$ nm [35,81] at room temperature. Therefore, the ferroelectric properties such as remanent polarization, coercive field, piezoelectric coefficient, etc., depend on the crystallographic orientation of the films with respect to the substrate normal. Moreover, due to their anisotropic structure, epitaxial thin films of these materials can be easily grown with the [001] axis parallel to the film normal (perpendicular to the film plane), i.e., in the so-called c -axis orientation. However, it is well known that, if c -axis-oriented, these materials have a very small polarization component along the film normal, because the vector of the (major) spontaneous polarization in these bismuth-layered perovskite materials is directed along the crystallographic a axis [26,27,28]. If the bismuth-layered perovskite materials are to be used in a ferroelectric thin film capacitor with electrodes on the top and bottom surfaces, the

component of the spontaneous polarization normal to the film plane is essential. Therefore it is desirable to grow non-*c*-axis-oriented films of these bismuth-layered perovskite materials in order to obtain a higher polarization component along the film normal. Epitaxial growth of thin films of these materials by pulsed laser deposition (PLD) [44,82,83,84], molecular beam epitaxy [85], radio-frequency sputtering [86], metalorganic chemical vapor deposition [87], and coating-pyrolysis process [88] have been reported.

To receive experience in SrRuO₃ and BLT epitaxy, to test the methods and the equipment, and to obtain a reference with respect to literature data, epitaxial BLT films were grown on SrRuO₃-covered SrTiO₃ substrates of three different orientations, and their microstructure and properties were investigated.

4.1 Experiment

The deposition of the SrRuO₃ electrode layers and the BLT thin films onto SrTiO₃ single crystal substrates of (001), (011), and (111) orientations was carried out *in situ* by PLD using a KrF excimer laser ($\lambda = 248$ nm) operated at a repetition rate of 5 Hz. The SrRuO₃ films were grown from a stoichiometric target at a substrate temperature of 700 °C in 0.14 mbar oxygen ambient using a laser energy density of 1.7 J/cm². The epitaxial BLT films were grown at 750 °C in 0.4 mbar of oxygen pressure with a laser energy density of 2.3 J/cm². A Bi-rich single target (2 inch in diameter) with Bi:La:Ti atom ratio of 3.75:0.75:3 was used as the source material. After the BLT film deposition, the samples were cooled to room temperature in 0.4 mbar oxygen atmosphere to prevent bismuth losses in the film. For the electrical characterization, Pt top electrodes with a diameter of 100 μ m were prepared by conventional photolithography lift-off. After top electrode deposition, the samples were annealed at 400 °C for 20 min in air to stabilize the contact between the BLT films and the Pt top electrodes.

4.2 Results and discussion

4.2.1 Crystallographic orientations and epitaxial relationships

θ - 2θ scans

Figure 4.1 shows XRD θ - 2θ scans of BLT films deposited on SrRuO₃-covered SrTiO₃ substrates of (a) (001), (b) (011), and (c) (111) orientations at a substrate temperature of 750 °C. Since the lattice mismatch, $(d_{\text{film}}-d_{\text{sub}})/d_{\text{sub}}$, between SrRuO₃ ($a_c=0.3928$ nm) and SrTiO₃ ($a_c=0.3905$ nm) is only 0.6%, the orientations of SrRuO₃ are identical with those of

SrTiO₃ as can be seen in Fig. 4.1. Well-developed BLT (00 l) reflections are seen as the only BLT reflections in Fig. 4.1(a). Thus a c -axis-oriented BLT film was grown on SrRuO₃(001)-covered SrTiO₃(001) substrate with high crystallinity as well as phase pure. The full width at half maximum (FWHM) values for the 0014 peak were 0.31° and 0.15° in 2θ and ω scans, respectively. The FWHM values of the (001)-oriented SrTiO₃ substrate are 0.31° and 0.14° for the 2θ and ω scans of the 002 peak, respectively.

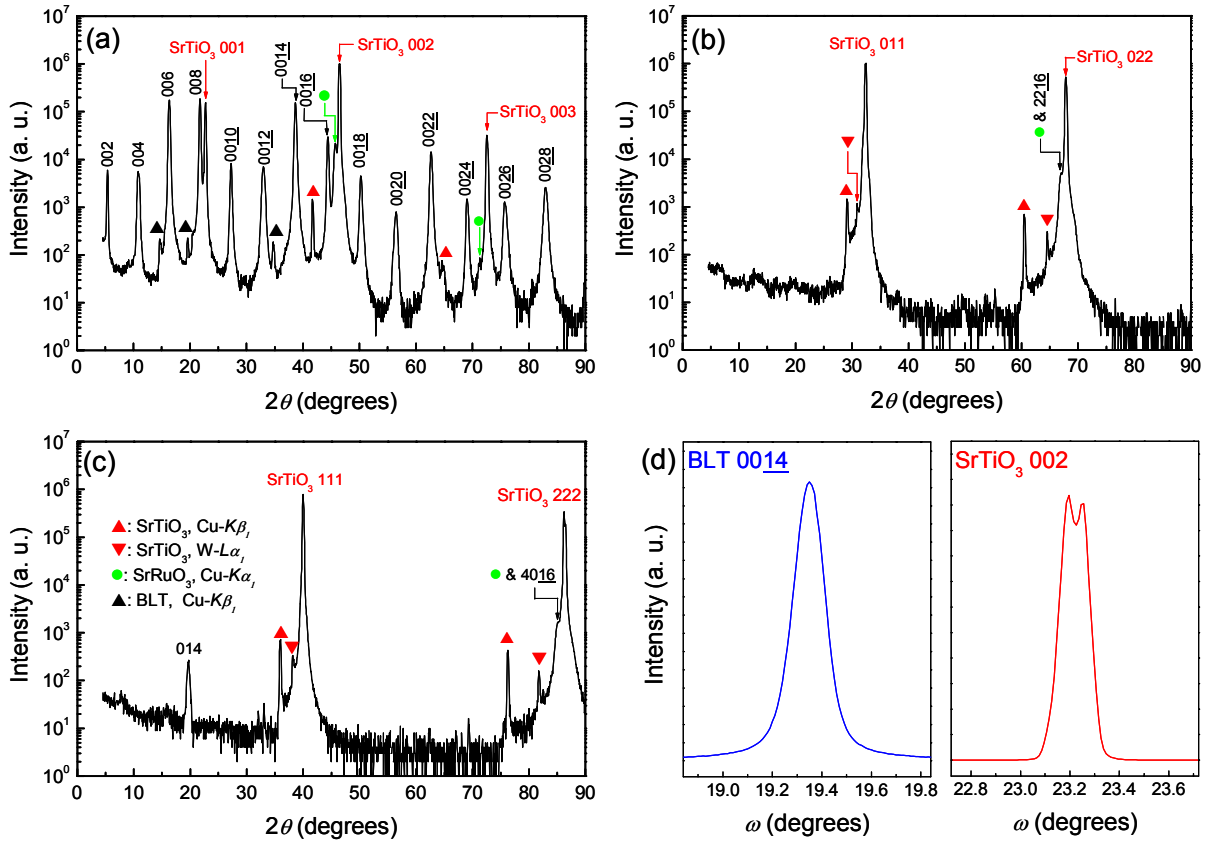


FIG. 4.1. X-ray diffraction θ - 2θ scans of BLT films on SrRuO₃-covered (a) (001)-, (b) (011)-, (c) (111)-oriented SrTiO₃ substrates. (d) X-ray diffraction ω scans of sample (a) for the BLT 0014 (left-hand side) and SrTiO₃ 002 peaks (right-hand side). The Cu- $K\beta_1$ lines are due to the remaining Cu- $K\beta_1$ radiation, and W- $L\alpha_1$ lines are due to the tungsten contamination of the x-ray target by the tungsten cathode filament. Due to the high diffraction intensity from the BLT epitaxial thin film, small BLT peaks coming from the Cu- $K\beta_1$ radiation are visible. The legend in (c) is also valid for (a) and (b).

Figure 4.1(b) shows a XRD θ - 2θ scan of a BLT film grown on SrRuO₃(011) on SrTiO₃(011) substrate, revealing mostly a (118)-oriented BLT film. Moreover, it can be seen that in this BLT film a small amount of (100) or (010) orientation is present: A corresponding slight shoulder to the right of the SrTiO₃ 011 and 022 substrate peaks was observed in the θ - 2θ scan. It should be noticed that the thickness of SrRuO₃ as a bottom electrode layer on all three SrTiO₃ single crystal substrates is only about 15nm. In the case of a different BLT film on about 50 nm thick SrRuO₃ on SrTiO₃(011) substrate, only the (118) orientation in the BLT

film was observed. In Fig. 4.1(b) the presence of a small amount of *a*-axis orientation is probably due to the very thin SrRuO₃ layer. This conclusion is in accordance with an investigation of Lee *et al.* [71] on the influence of the SrRuO₃ layer thickness on the respective amounts of (118)- and (100)-oriented BLT in their films. I also confirmed this minor phase of (100) orientation of BLT film on SrRuO₃(011)/SrTiO₃(011) substrates from the analyses of XRD ϕ scans, pole figures, and atomic force microscopy (AFM) images. A XRD θ - 2θ scan of a BLT film on a SrRuO₃(111)-covered SrTiO₃(111) single crystal substrate is shown in Fig. 4.1(c). The scan reveals a nearly phase pure (104)-oriented BLT film. FWHM values for (118)- and (014)-oriented BLT films were 1.05° and 0.83° in ϕ scans of the BLT 0014 peak [see Figs. 4.3(c) and 4.3(e) below]. The FWHM values of (011)- and (111)-oriented SrTiO₃ substrates were 0.25° and 0.21° in the ϕ scans of the 002 reflection [Figs. 4.3(d) and 4.3(f) below].

Pole figures

In order to confirm the crystallographic orientations of BLT and determine whether the BLT/SrRuO₃/SrTiO₃ heterostructures are epitaxial, various pole figure analyses were performed. Figure 4.2 shows pole figures of the BLT films on SrRuO₃-covered SrTiO₃ single crystal substrates of (a) (001), [(b) and (d)] (011), and (c) (111) orientations. For Figs. 4.2(a)–4.2(c), the fixed 2θ used to record the pole figures was 30.1° corresponding to the BLT 117 reflection. In the case of the *c*-axis-oriented BLT film in Fig. 2(a), four peaks with a single-domain situation are observed at $\psi \approx 51^\circ$ showing that the BLT(001) film has a good in-plane orientation; the BLT{117} planes have a tilt angle of 50.7° with respect to the BLT (001) plane, which is parallel to the substrate surface.

As already indicated above, in the case of a BLT film on SrTiO₃(011) interestingly, two sets of peaks corresponding to (118) and (100) orientations in the BLT film are seen in Fig. 4.2(b). The pole figure consists of a set of peaks (marked “A”) that stems from the (118)-oriented part of the BLT film, and of another set (marked “B”) which stems from the (100)-oriented part. First of all, the major set “A” is composed of peaks located at $\psi \approx 4^\circ$, 65°, and 82° corresponding to 117, $\bar{1}17/1\bar{1}7$, and $11\bar{7}$ peaks, respectively, from the (118)-oriented part of the film, which is double twinned [cf. the angles $\angle (118) : (117) = 3.8^\circ$, $\angle (118) : (\bar{1}17) = 64.1^\circ$, $\angle (118) : (1\bar{1}7) = 64.6^\circ$, and $\angle (118) : (11\bar{7}) = 82.4^\circ$]. The minor set “B” appears at $\psi \approx 57^\circ$ consisting of the 117, $1\bar{1}7$, $1\bar{1}\bar{7}$, and $11\bar{7}$ peaks from the (100)-oriented part of the film, revealing that this part has a single-domain situation. Finally, in case of the (104)-oriented BLT film, a triple-twin situation is observed as demonstrated by the pole figure shown in Fig. 4.2(c). The peaks at $\psi \approx 36^\circ$ and 84° correspond to $117/1\bar{1}7$ reflections and $1\bar{1}\bar{7}/11\bar{7}$ reflections, respectively, indicating that the (104)-oriented BLT film has a triple-domain structure and showing that the BLT (104) plane is parallel to the SrTiO₃ (111)

substrate plane, because the angle between the (104) and (117) planes of BLT is 36.2°. For the BLT film grown on the SrTiO₃(011) substrate, an additional pole figure was recorded using the BLT 111 reflection ($2\theta=23.31^\circ$), shown in Fig. 4.2(d). From Figs. 4.2(b) and 4.2(d), the presence of some (100) orientation in the BLT films grown on SrTiO₃(011) is clearly confirmed.

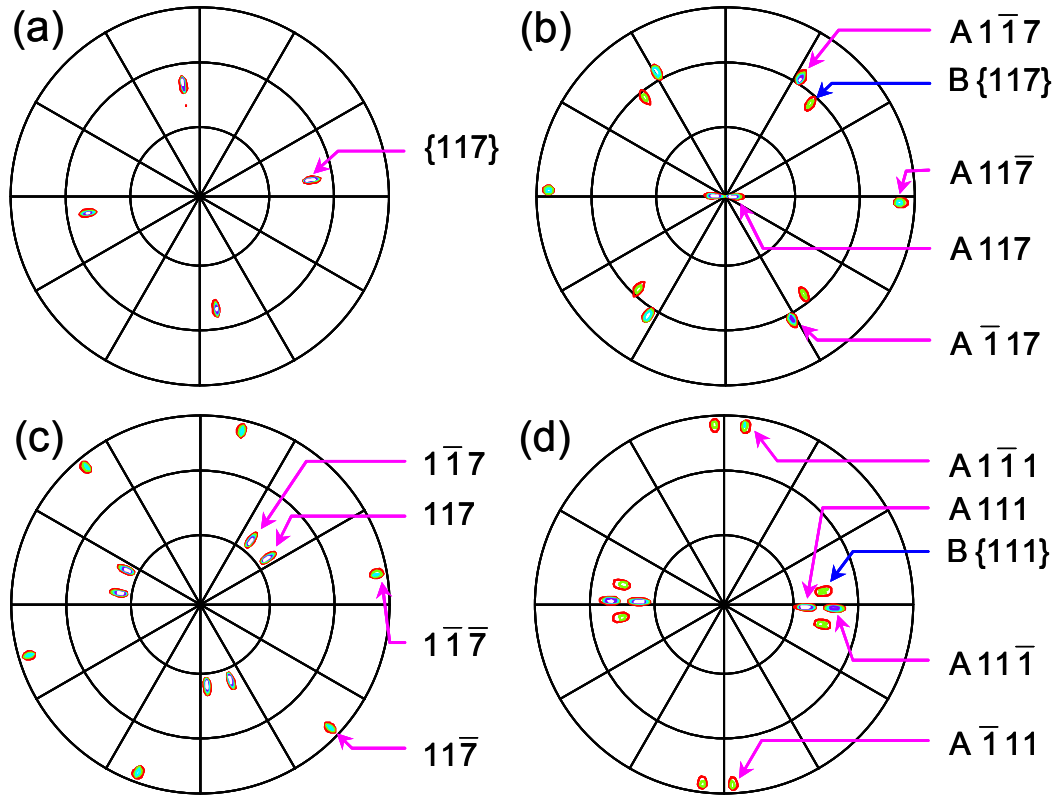


FIG. 4.2. X-ray diffraction pole figures of BLT/SrRuO₃ heterostructures on (a) (001)-, [(b) and (d)] (011)-, (c) (111)-oriented SrTiO₃ substrates. The fixed 2θ angles were 30.1° [(a) to (c)] and 23.31° for Fig. 4.2(d) corresponding to BLT 117 and 111 reflections, respectively. Peaks originating from (118)- and (100)-oriented parts of the BLT film are denoted “A” and “B”, respectively in (b) and (d). The center and the rim of the pole figures correspond to $\psi=0^\circ$ and 90° , respectively; $\psi=90^\circ$ corresponds to the substrate surface being parallel to the plane defined by the incident and reflected x-ray beams.

ϕ scans

As shown in Fig. 4.3, ϕ scans of the BLT films and the SrTiO₃ substrates were performed in order to establish the in-plane orientation alignments of the BLT films with respect to the underlying SrTiO₃ substrates. In Figs. 4.3(a) and 4.3(b), ϕ scans of a c -axis-oriented BLT film on a SrTiO₃(001) substrate are shown, recorded using the BLT (2216) and SrTiO₃ (022) reflections, respectively. The ϕ rotation axis is parallel to the c axis of BLT and the [001] axis of SrTiO₃. The positions of the peaks from BLT(2216) are identical to those of

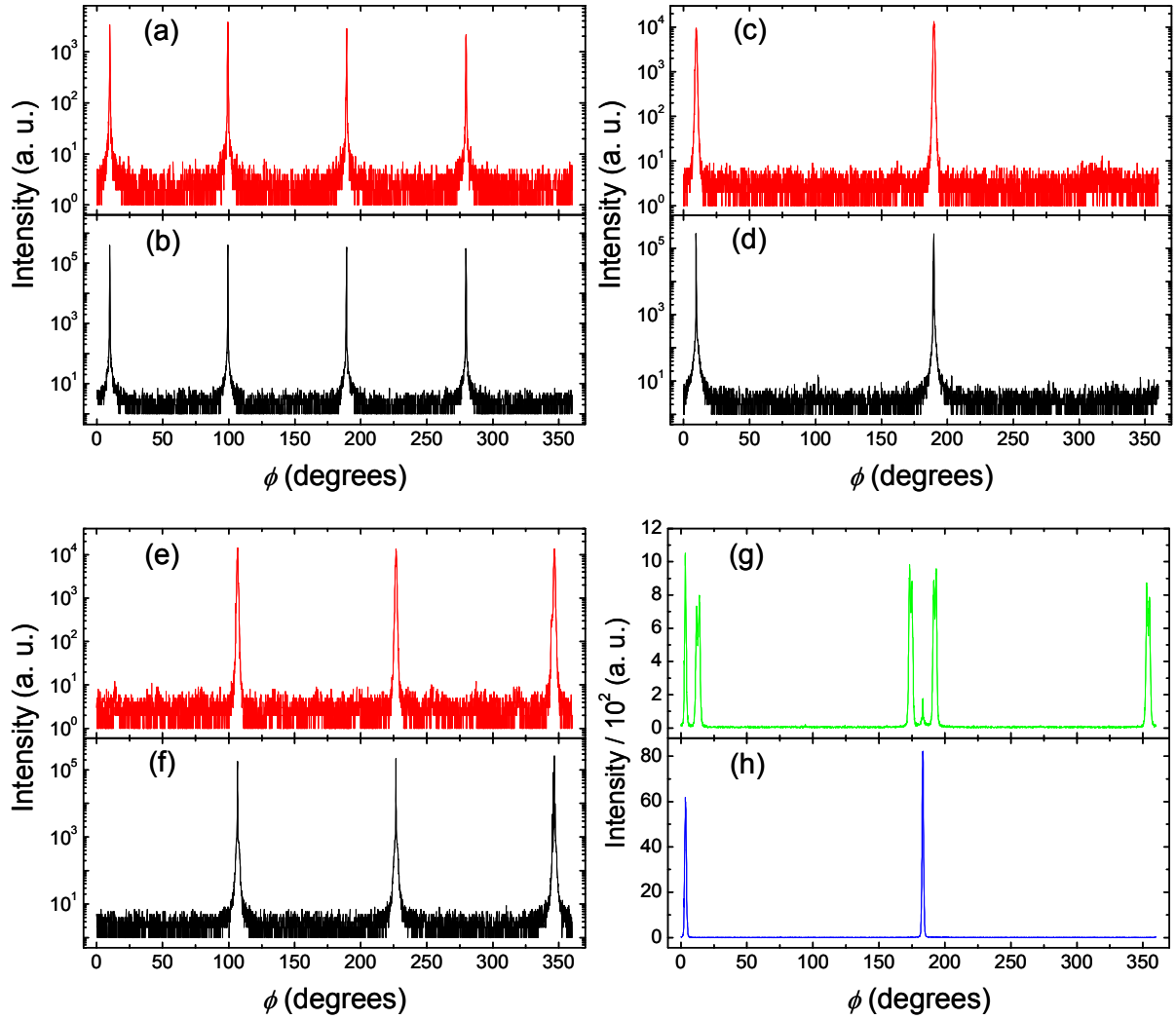


FIG. 4.3. [(a) and (b)] X-ray diffraction ϕ scans of a BLT thin film on a SrRuO₃(001)/SrTiO₃(001) substrate: (a) BLT $22\bar{1}6$ reflection at $\psi=46.9^\circ$ and (b) SrTiO₃ 022 reflection at $\psi=45^\circ$. [(c) and (d)] ϕ scans of a BLT film on SrRuO₃(011)/SrTiO₃(011): (c) BLT $00\bar{1}4$ reflection at $\psi=46.9^\circ$ and (d) SrTiO₃ 002 reflection at $\psi=45^\circ$. [(e) and (f)] ϕ scans of a BLT(104)/SrRuO₃(111)/SrTiO₃(111) heterostructure: (e) BLT $00\bar{1}4$ reflection at $\psi=56.4^\circ$ and (f) SrTiO₃ 002 reflection at $\psi=54.7^\circ$. [(g) and (h)] ϕ scans of a BLT film on SrRuO₃(011)/SrTiO₃(011) recorded using the BLT 111 reflection at (g) $\psi=46^\circ$ and (h) $\psi=36^\circ$, in correspondence to (100) and (118) orientations.

the peaks from SrTiO₃(022), which clearly shows that the BLT unit cell is rotated by 45° in plane with respect to the SrTiO₃ substrate, namely BLT $[1\bar{1}0]||\text{SrTiO}_3[100]$. The appearance of the peaks every 90° indicates a good quality of the in-plane BLT orientation as revealed by a FWHM of 0.30° in the ϕ scans of the BLT $22\bar{1}6$ peak [cf. the FWHM of a (001)-oriented SrTiO₃ substrate which was 0.25° in the ϕ scans of the 022 peak]. ϕ scans of BLT($00\bar{1}4$) and SrTiO₃(002) were recorded for a (118)-oriented BLT film on a SrTiO₃(011) substrate, as shown in Figs. 4.3(c) and 4.3(d). The two peaks originating from BLT ($00\bar{1}4$) were detected on the same ϕ positions as those of SrTiO₃(002), which results in the in-plane orientation relationship BLT $[1\bar{1}0]||\text{SrTiO}_3[100]$ or BLT $[1\bar{1}0]||\text{SrTiO}_3[010]$ (two azimuthal domains).

Finally, the in-plane epitaxial relation of (104)-oriented BLT on SrTiO₃(111) was determined by ϕ scans of BLT(001) and SrTiO₃(002) as seen in Figs. 4.3(e) and 4.3(f). Three peaks of both the BLT film and the SrTiO₃ substrate can be seen at the same ϕ positions. This results in the in-plane epitaxial orientation of the BLT(104) film on the SrTiO₃(111) substrate BLT[010]||SrTiO₃[$\bar{1}$ 10], BLT[010]||SrTiO₃[0 $\bar{1}$ 1], or BLT[010]||SrTiO₃[10 $\bar{1}$] (three azimuthal domains). Figure 4.3(g) and 4.3(h) show ϕ scans of the sample of Fig. 4(c), i.e., the BLT film on SrTiO₃(011). They were recorded using the BLT 111 reflection at $\psi=46^\circ$ [Fig. 4.3(g)] and $\psi=36^\circ$ [Fig. 4.3(h)], corresponding to the (100) and (118) orientations, respectively. Comparing the two intensities in the ϕ scans, the volume fraction, $I_{100}/(I_{100}+I_{118})$, of (100) orientation in the BLT film on SrTiO₃(001) is about 10%.

Summarizing the XRD results of Figs. 1, 2, and 3, the two-dimensional epitaxial relationships between the BLT films and the underlying SrTiO₃ substrates can be summarized as follows [ignoring azimuthal domain variants and the minor (100)-oriented BLT part on SrTiO₃(011)]:

$$\text{BLT}(001) \parallel \text{SrTiO}_3(001); \quad \text{BLT}[1 \bar{1} 0] \parallel \text{SrTiO}_3[100], \quad (4.1)$$

$$\text{BLT}(118) \parallel \text{SrTiO}_3(011); \quad \text{BLT}[1 \bar{1} 0] \parallel \text{SrTiO}_3[100], \quad (4.2)$$

$$\text{BLT}(104) \parallel \text{SrTiO}_3(111); \quad \text{BLT}[010] \parallel \text{SrTiO}_3[\bar{1} 10]. \quad (4.3)$$

Orientation relation

Based on the XRD analyses the epitaxial orientation relationship of the BLT films and underlying SrTiO₃ single crystal substrates are schematically summarized in Fig. 4.4. Figure 4.4(a) (left hand side) shows the in-plane orientation relationship for a (001)-oriented BLT film grown on (001)-oriented SrTiO₃. It can be seen that the BLT 001 plane is rotated by 45° with respect to the SrTiO₃(001) plane for epitaxial alignment, namely BLT[1 $\bar{1}$ 0]||SrTiO₃[100], as mentioned before. The lattice mismatches along BLT[100]||SrTiO₃[110] and BLT[010]||SrTiO₃[$\bar{1}$ 10] are about -1.3% and -2.0%, respectively. Figure 4(b) shows the situation on the SrTiO₃(011) plane. The two mismatch values along BLT[$\bar{4}$ $\bar{4}$ 1]||SrTiO₃[0 $\bar{1}$ 1] and BLT[$\bar{1}$ 10]||SrTiO₃[$\bar{1}$ 00] are about +1.8% and -1.7%, respectively. Finally, Fig. 4(c) shows the situation on the SrTiO₃(111) plane. The two mismatch values along BLT[$\bar{4}$ 0 1]||SrTiO₃[$\bar{1}$ $\bar{1}$ 2] and BLT[010]||SrTiO₃[$\bar{1}$ 10] are about +2.8% and -2.0%, respectively. The [001] directions of the SrTiO₃ substrates having (011) and (111) orientations are tilted nearly 45° and 55°, respectively, away from the normal to the substrate surface. Therefore when BLT films are epitaxially grown on these substrates, their *c* axes will also be tilted nearly 45° and 55° away from the normal to the substrate plane. The BLT planes that are

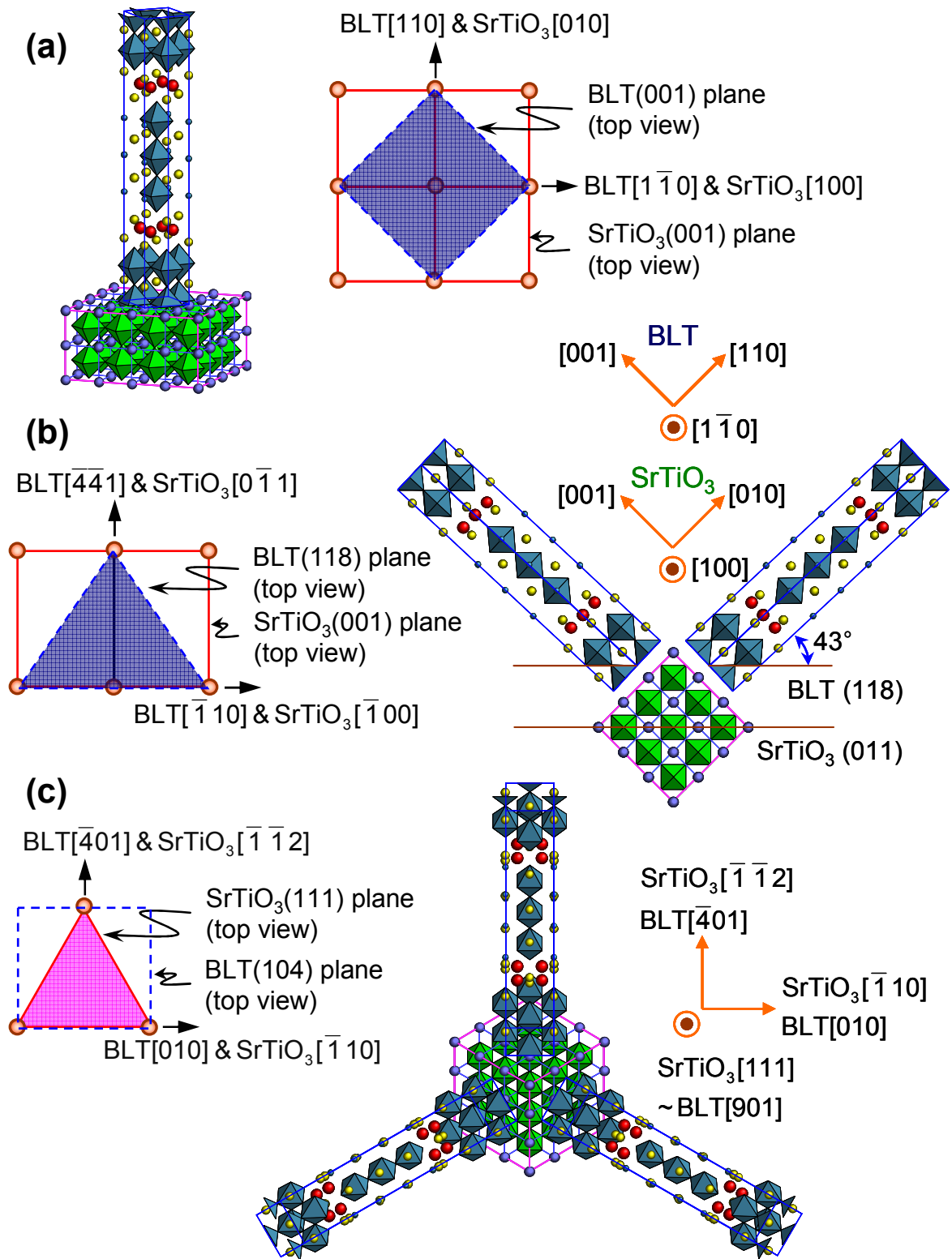


FIG. 4.4. Schematic drawing of the epitaxial relationships of BLT on SrTiO₃; (a) BLT(001)||SrTiO₃(001), (b) BLT(118)||SrTiO₃(011), and (c) BLT(104)||SrTiO₃(111).

corresponding (parallel) to the SrTiO₃(011) and SrTiO₃(111) planes are BLT(118) and BLT(104), as can be seen in Figs. 4.1, 4.2, and 4.3. Correspondingly, the angles that these planes make with the BLT(001) plane are $\angle (001) : (118) = 46.9^\circ$ and $\angle (001) : (104) = 56.4^\circ$ [cf. the angles $\angle (001) : (011) = 45^\circ$ and $\angle (001) : (111) = 54.7^\circ$ for the SrTiO₃ substrate].

The close similarity of the BLT lattice parameters a and b makes it most difficult to differentiate by XRD between, e.g., the planes (100) and (010), or the planes (104) and (014), unless high resolution methods are available. As a consequence, unlike the situation for simple perovskites, standard XRD methods are not suitable to investigate the presence of 90° a - b ferroelectric domains in BLT. Selected area electron diffraction (SAED), however, principally allows to differentiate, e.g., between the directions [100] and [010] due to some difference between the corresponding electron diffraction patterns [81,89]. As a TEM/SAED study has shown, 90° a - b boundaries are present in as-grown BLT films, the domains having, however, very small diameters of the order of 5 to 10 nm [89]. Due to this small size and the general difficulty to investigate 90° domains in BLT, the a - b switchability in lanthanide-substituted bismuth titanate is still a matter of controversy in the literature. This question is therefore not discussed in this thesis, and a differentiation between, e.g., (104) and (014) planes, is not considered.

4.2.2 Surface morphology

Figure 4.5 shows AFM topographic images of the surface morphologies of BLT films grown on SrRuO₃-covered SrTiO₃ single crystal substrates of different orientations, revealing very different surface morphologies. In the case of a (001)-oriented BLT film, submicron-sized flat grains are observed in Fig. 4.5(a). The root mean square (rms) surface roughness of this film over an area of $3 \times 3 \mu\text{m}^2$ was about 1.4 nm. As can be seen in Fig. 4.5(b) [magnified AFM image of Fig. 4.5(a)] round grains are clearly visible. These round grains on the surface were also observed in c -axis-oriented films of bismuth-layered perovskite compounds such as ferroelectric SBT and Bi₄Ti₃O₁₂ materials [45,84,85]. Moreover, the formation of a round grain shape due to a spiral growth mechanism was reported in c -axis-oriented superconducting YBa₂Cu₃O₇ films deposited by PLD or sputtering [90].

In the case of a BLT film grown on SrRuO₃(011)/SrTiO₃(011) substrate in Fig. 4.5(c), it is interesting to note that there are two distinct shapes of grains, namely long needlelike ones and more or less equiaxed ones. It turned out that the needlelike grains correspond to the (118)-oriented part of the film, whereas the equiaxed grains represent the (100)-oriented one, cf., Refs. 71 and 91. According to the XRD pole figures and ϕ scans, the occurrence of (100)-oriented grains in the BLT films on about 15 nm-thick SrRuO₃-covered SrTiO₃(011) could already be expected, and the volume fraction of (100) orientation could be roughly estimated from the distribution of the two distinct grain shapes visible in AFM topography images. Most

similar AFM topography images consisting of a mix of needlelike grains [(118) orientation] and equiaxed ones [(100) orientation] were also observed in BLT films grown on buffered Si(100) substrates [71,91] as well as in mixed (116)- and (100)-oriented SBT films grown on (110)-oriented SrLaGaO₄ single crystal substrates [92] by PLD. The long edges of needlelike (118) grains are parallel to the BLT[1 $\bar{1}$ 0] direction as well as to SrTiO₃[100], and the *c* axes of the grains point $\sim 43^\circ$ out of the film plane, the *c* axis being perpendicular to the long edge of the grain.

Figure 4.5(d) represents an AFM image of a BLT film of (104) orientation on a SrRuO₃(111)/SrTiO₃(111) substrate exhibiting a threefold symmetry of the distribution of the grains. The grains are arranged along three directions with 120° in between, which result from the growth of the BLT film with a triple-domain structure. In addition, I observed that the rms roughness of 21.1 nm on the (104)-oriented BLT film is higher than that of 16.8 nm on the BLT film grown on a SrTiO₃(011) substrate.

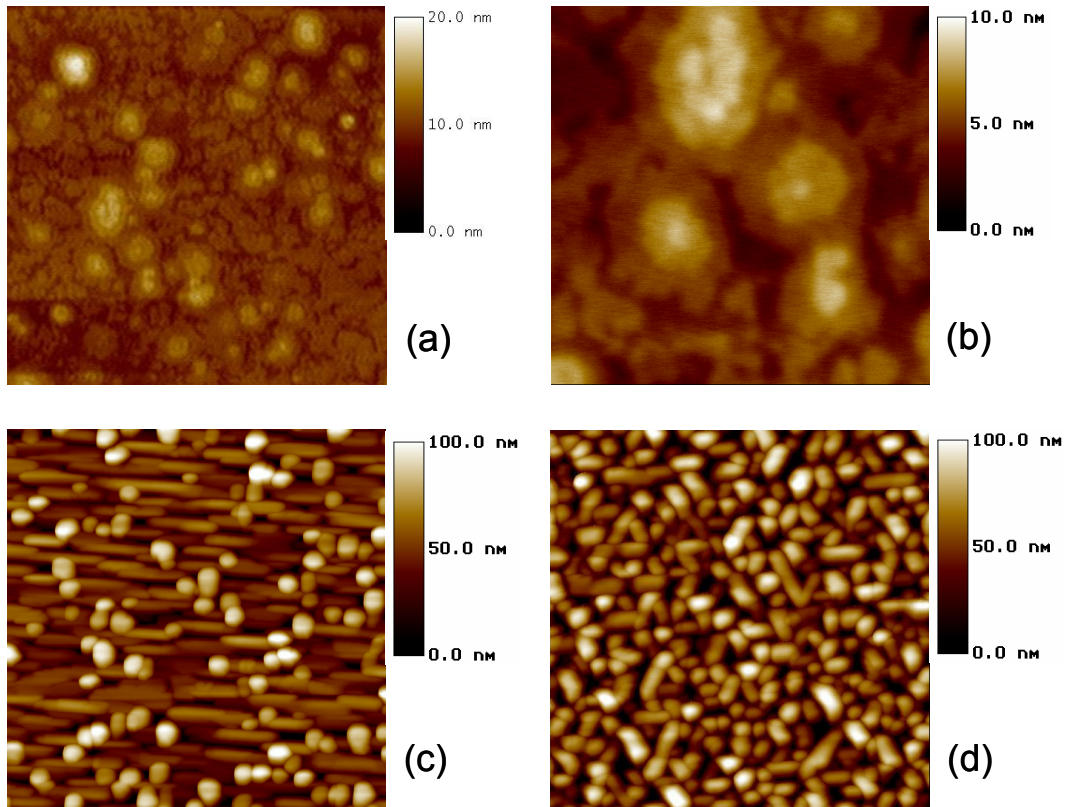


FIG. 4.5. AFM topography images of BLT films grown on SrRuO₃-covered [(a) and (b)] (001)-, (c) (011)-, (d) (111)-oriented SrTiO₃ single crystal substrates. (b) Magnified AFM topography image of part of a *c*-axis-oriented BLT film in (a). The image size of (a), (c) and (d) is $3 \times 3 \mu\text{m}^2$ while in (b) it is $1 \times 1 \mu\text{m}^2$.

4.2.3 Ferroelectric properties

Since the vector of the spontaneous polarization in BLT is almost directed along its a axis, the growth of non- c -axis-oriented films is required to achieve a large polarization component along the normal to the film plane. The directions of the vector \vec{P} of the spontaneous polarization of (001)-, (118)-, and (104)-oriented BLT films are away from the normal to the substrate surface by 90° , $\sim 59^\circ$, and $\sim 34^\circ$, respectively [cf. the angles $\angle \text{BLT}(001) : \text{BLT}(100) = 90^\circ$, $\angle \text{BLT}(118) : \text{BLT}(100) = 59.0^\circ$, and $\angle \text{BLT}(104) : \text{BLT}(100) = 33.6^\circ$]. Therefore the perpendicular polarization components of BLT films having different orientations can be estimated by means of the above angles. The components of the vector \vec{P}_s perpendicular to the substrate surface, for (001), (118), and (104) orientations, are proportional to the values of $P_\perp^{001} = |\vec{P}_s| \cdot \cos 90^\circ = 0$, $P_\perp^{118} = |\vec{P}_s| \cdot \cos 59^\circ \approx 0.5|\vec{P}_s|$, and $P_\perp^{104} = |\vec{P}_s| \cdot \cos 34^\circ \approx 0.8|\vec{P}_s|$ as can be schematically seen in Fig. 4.6. Accordingly, from these normal polarization components the c -axis-oriented BLT film exhibits a zero normal polarization component and the (104)-oriented BLT film reveals an about 1.6 times larger normal polarization than the (118)-oriented BLT film.

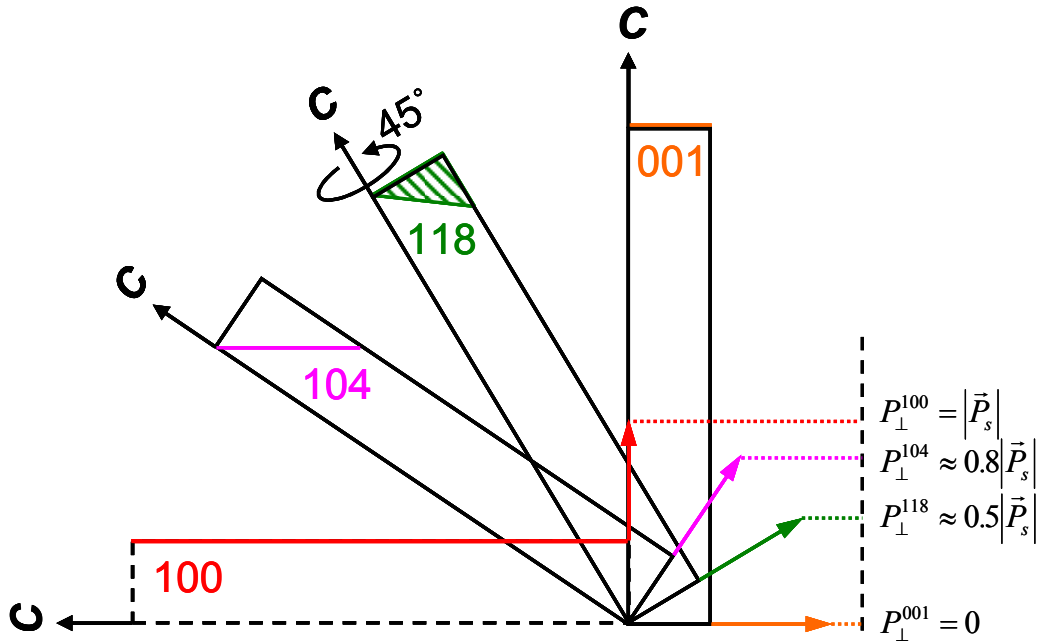


FIG. 4.6. Schematic drawing of polarization components of BLT thin films with (001), (118), (104), and (100) orientations. The vertical components of the spontaneous polarization with respect to the substrate plane are denoted “ P_\perp ”.

Ferroelectric polarization–electric field (P – E) hysteresis loops were recorded in order to evaluate the dependence of ferroelectricity on the different crystallographic orientations in BLT. Figure 4.7 shows ferroelectric hysteresis loops recorded from (a) (001)-, (b) (118)-, and (c) (104)-oriented BLT films grown on (001)-, (011)-, and (111)-oriented SrRuO₃ bottom electrodes, clearly demonstrating the ferroelectric anisotropy. As can be seen in Fig. 4.7(b), the measured remanent polarization ($2P_r$) and coercive field ($2E_c$) of the (118)-oriented BLT films were $21.8\mu\text{C}/\text{cm}^2$ and $180.4\text{ kV}/\text{cm}$, respectively, for a maximum applied electric field of $450\text{ kV}/\text{cm}$. About 1.5 times higher remanent polarization ($2P_r=32.62\mu\text{C}/\text{cm}^2$) was recorded in (104)-oriented BLT films. As schematically illustrated in Fig. 4.6, the estimated polarization component of a (104)-oriented BLT film normal to the film plane is 1.6 times higher than that of a (118)-oriented BLT film. From this result, it was found that although BLT films grown on SrTiO₃(011) substrates with about 15 nm thick SrRuO₃ electrode layer have about 10% volume fraction of (100) orientation, this amount of volume fraction of a -axis orientation had no significant influence on its overall polarization. The c -axis-oriented BLT

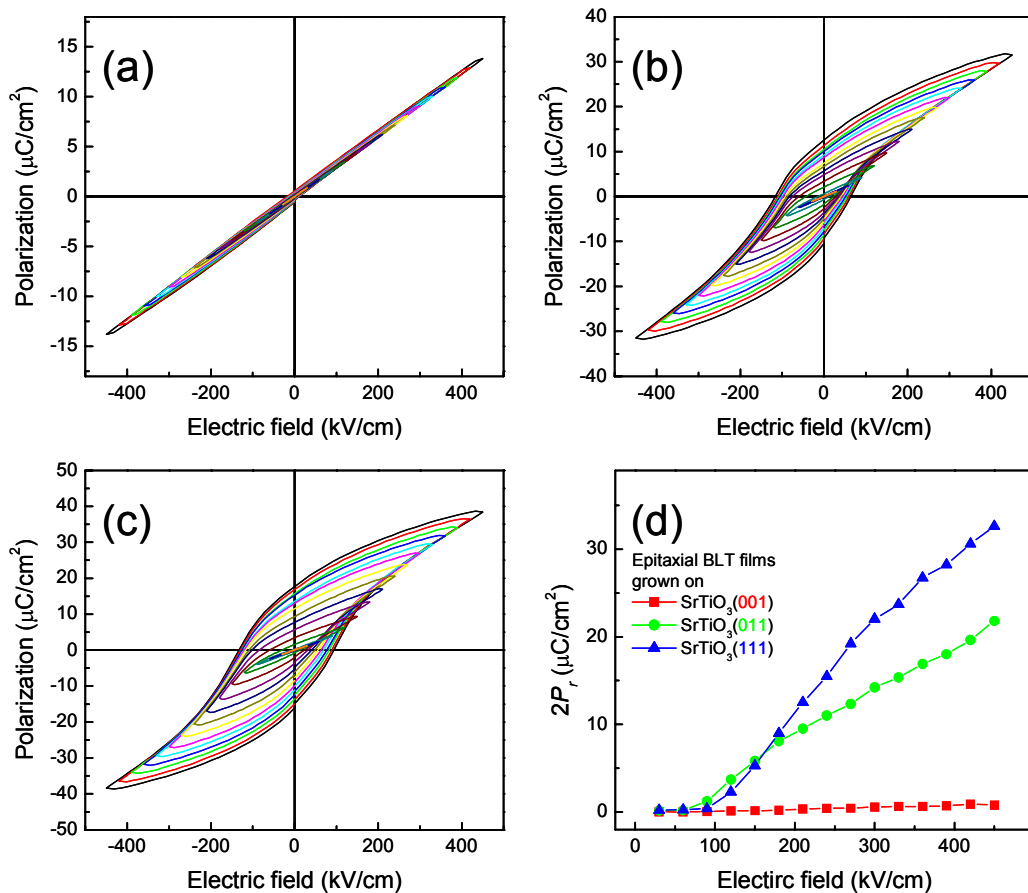


FIG. 4.7. [(a) to (c)] P – E hysteresis loops of epitaxially twinned BLT films with (a) (001), (b) (118), and (c) (104) orientations for various applied electric fields. (d) Remanent polarization ($2P_r$) of BLT films of corresponding orientations as a function of the applied electric field. Different colors of P – E hysteresis loops stand for various applied electric fields.

exhibiting weak ferroelectricity, a small polarization component ($2P_r=0.81 \mu\text{C}/\text{cm}^2$ and $2E_c=25.7 \text{ kV}/\text{cm}$) was found in the (001)-oriented BLT films as shown in Fig. 4.7(a). This result confirms that *c*-axis-oriented BLT has a small component of the polarization along the normal to the film plane. Figure 4.7(d) summarizes the recorded remanent polarization ($2P_r$) of the BLT films grown on the different SrTiO₃ substrates covered with SrRuO₃.

Figure 4.8 shows the fatigue endurance of (118)-oriented and (104)-oriented BLT films. The values of switching polarization $P_{sw} = (P_{max+} - P_{r-})$ are shown as a function of the number of switching cycles up to 4.6×10^{10} cycles at a frequency of 1 MHz, where P_{max+} is the polarization value at positive saturation and P_{r-} stands for the polarization in the negative remanent state. After being subject to 4.6×10^{10} cycles, both (118)- and (104)-oriented films revealed only very weak fatigue.

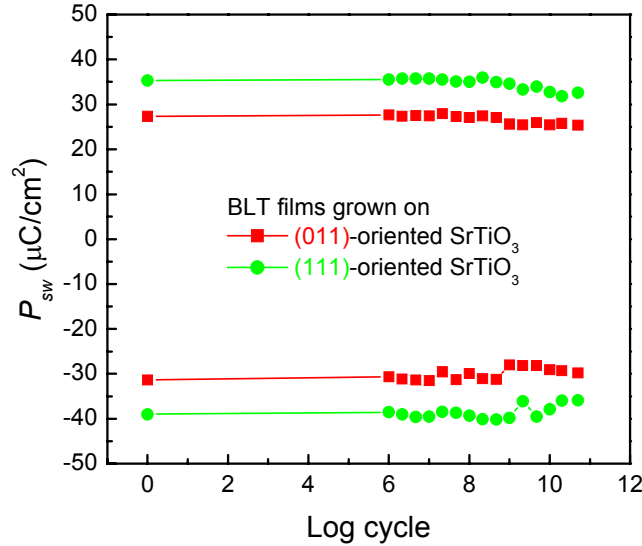


FIG. 4.8. Fatigue properties of epitaxial BLT films grown on SrRuO₃-covered (011)- and (111)-oriented SrTiO₃ substrates. The fatigue was recorded by applying an ac electric field of the amplitude 300 kV/cm at a frequency of 1 MHz.

4.3 Summary

Epitaxial (001)-oriented and epitaxially twinned (118)- and (104)-oriented BLT thin films have been grown by PLD on (001)-, (011)-, and (111)-oriented SrTiO₃ single crystal substrates, respectively, covered with SrRuO₃ electrodes. By XRD characterization it has been found that the low-index three-dimensional epitaxial relationship BLT(001)||SrRuO₃(001)||SrTiO₃(001); BLT[1 $\bar{1}$ 0]|| SrRuO₃[100]||SrTiO₃[100] is valid for all (epitaxially twinned) BLT thin films in spite of their different orientation. The (104)-oriented BLT films showed an about 1.5 times higher remanent polarization than the (118)-oriented BLT films, while (001)-

oriented BLT films revealed only a very small polarization component. The ferroelectric anisotropy was demonstrated and a good fatigue resistance was observed.

The results of this chapter show that uniformly oriented BLT films can be grown with sufficient quality using our group's PLD equipment, and that the applied XRD, AFM, and ferroelectric measurement methods are suitable to characterize them. The orientation relationship, surface topographies, and ferroelectric properties obtained are in accordance with corresponding literature data and represent a suitable base for the experiments on non-*c*-axis-oriented BLT and Nd-substituted Bi₄Ti₃O₁₂ (BNT) growth onto Si(100) substrates described in the next chapter.

Chapter 5

Epitaxial growth of (104)-oriented rare-earth element-substituted $\text{Bi}_4\text{Ti}_3\text{O}_{12}$ thin films on silicon substrates using (111)-oriented Pt electrode layers

Numerous attempts to grow epitaxial non-*c*-axis-oriented thin films of bismuth-layered perovskite compounds have been made using single crystal substrates such as LaSrAlO_4 [44], MgO [86], SrLaGaO_4 [92], SrTiO_3 [93,94,95,96,97], and TiO_2 [98]. However these complex oxide single crystals are not suitable as substrates in microelectronics. For better compatibility with silicon-based microelectronics, epitaxial films of bismuth-layered perovskites should be grown on silicon substrates [66,71,99]. For accomplishing this purpose, a sequence of appropriate intermediate layers between the ferroelectric film and the silicon substrate should be used, mainly to reduce the lattice mismatch between the film and the silicon substrate, but also fulfilling the requirement of a bottom electrode. An approach to grow non-*c*-axis-oriented SBT epitaxial thin films with (103) orientation on $\text{SrRuO}_3(111)/\text{MgO}(111)/\text{YSZ}(100)/\text{Si}(100)$ substrates has been reported [99]. To date, however, there have been no reports on epitaxial growth of (104)-oriented La-substituted $\text{Bi}_4\text{Ti}_3\text{O}_{12}$ (BLT) or Nd-substituted $\text{Bi}_4\text{Ti}_3\text{O}_{12}$ (BNT) films on buffered Si(100) substrates.

I have investigated the use of an intermediate SrRuO_3 layer to achieve orientation control in the epitaxial growth of both BLT and BNT films on (111)-oriented Pt electrode layers deposited onto $\text{YSZ}(100)/\text{Si}(100)$ substrates. SrRuO_3 will be shown to grow in an oriented fashion on Pt-covered silicon substrates, with $\text{SrRuO}_3(111)\parallel\text{Pt}(111)$. Additionally, unlike the direct deposition of BLT (or BNT) on platinum, the strong chemical stability of the BLT (or BNT)/ SrRuO_3 and SrRuO_3/Pt interfaces minimizes any reactions between the platinum and BLT (or BNT) layers. Therefore the function of SrRuO_3 is twofold. First, it acts

as a diffusion barrier between BLT (or BNT) and platinum, and second it provides a suitable template for the epitaxial growth of the BLT (or BNT) layer.

The crystal structure of BLT can be described as a stack of alternating layers of bismuth oxide (Bi_2O_2)²⁺ units and pseudoperovskite ($\text{Bi}_2\text{Ti}_3\text{O}_{10}$)²⁻ units containing TiO_6 octahedra, with a rare-earth element, e.g., La, substituting for Bi in the pseudoperovskite layers. It has been reported for this structure that the rotation of TiO_6 octahedra in the *a*-*b* plane accompanied with a shift of the octahedron along the *a* axis is largely enhanced by the rare-earth element substitution for Bi in the pseudoperovskite layer [26,35]. However, substitution of the Bi^{3+} cation with La^{3+} reduces the structural distortion of the perovskite block and therefore reduces the remanent polarization. The substitution of Bi in the pseudoperovskite layer by lanthanide ions having smaller ionic radii than Bi such as Nd or Sm should maintain a more significant structural distortion and improve the ferroelectric properties. The higher the distortion, the higher the remanent polarization will be. Ionic radii for these elements for twelvefold coordination are 0.136 nm (Bi^{3+}), 0.127 nm (Nd^{3+}), and 0.124 nm (Sm^{3+}) [100]. Recently, Chon *et al.* have reported very high values of remanent polarization ($2P_r$) of 103 $\mu\text{C}/\text{cm}^2$ in BNT ($\text{Bi}_{3.15}\text{Nd}_{0.85}\text{Ti}_3\text{O}_{12}$) films prepared by a sol-gel process [37]. To compare the effect of the substitution of lanthanide ions, investigations using epitaxial films with the same orientation are essential, because the ferroelectric properties of these materials depend strongly on the film orientation. For the above purpose, Kojima *et al.* have grown epitaxial (104)-oriented films of BNT ($\text{Bi}_{3.54}\text{Nd}_{0.46}\text{Ti}_3\text{O}_{12}$), BLT ($\text{Bi}_{3.44}\text{La}_{0.56}\text{Ti}_3\text{O}_{12}$), and $\text{Bi}_4\text{Ti}_3\text{O}_{12}$ materials grown on $\text{SrRuO}_3(111)$ electrode layers on $\text{SrTiO}_3(111)$ substrates by metalorganic vapor deposition (MOCVD) and obtained higher remanent polarization values from BNT films compared to those of BLT and $\text{Bi}_4\text{Ti}_3\text{O}_{12}$ films [97].

Here I report on the epitaxial growth of non-*c*-axis-oriented lanthanide-substituted $\text{Bi}_4\text{Ti}_3\text{O}_{12}$ films with (104) orientation on buffered Si(100) substrates using (111)-oriented Pt layers, as well as on the effect of the substitution of lanthanide ions using films with the same orientation.

5.1 Experiment

All films of ferroelectric BLT and BNT, SrRuO_3 conducting layer and yttria-stabilized zirconia (YSZ) buffer layer except Pt films were deposited by pulsed laser deposition (PLD), employing a KrF excimer laser ($\lambda = 248$ nm) operating at a repetition rate 5 Hz with an energy density of 1.7–3.4 J/cm^2 . Pt layers were deposited on YSZ(100)-buffered Si(100) substrates by rf sputtering at a substrate temperature of 400 °C. The (111)-oriented Pt films were grown in 2.4×10^{-3} mbar pure argon ambient using a rf power of 10 W employing a Pt source target (2 inch in diameter). The epitaxial YSZ, SrRuO_3 , BLT and BNT films were grown at substrate temperatures of 800 °C (YSZ), 700 °C (SrRuO_3), and 500–825 °C (BLT

and BNT) in flowing O₂ pressure of 2.4×10^{-4} mbar (YSZ), 0.14 mbar (SrRuO₃), and 0.4 mbar (BLT and BNT), respectively. A bismuth-excess Bi_{3.75}La_{0.75}Ti₃O₁₂ and a Bi_{3.54}Nd_{0.46}Ti₃O₁₂ target were used for PLD.

5.2 Results and discussion

5.2.1 Growth of (111)-oriented Pt electrode layer

X-ray diffraction θ - 2θ scans, pole figures, and ϕ scans

Figure 5.1 shows an x-ray diffraction (XRD) θ - 2θ scan of a Pt thin film grown on a (100)-oriented YSZ buffered Si(100) substrate at a substrate temperature of 400 °C, using an rf plasma power of 10 W. The scan reveals x-ray peaks for (111)-oriented Pt and (100)-oriented YSZ films without impurity phases. A very low-intensity peak at $2\theta \approx 33^\circ$ is a Si 200 reflection which is theoretically forbidden but occurs to appear experimentally. (This peak most probably stems from the Si 400 Bragg reflection of half the wavelength of the Cu- $K\alpha$ radiation, the half wavelength being present in the white radiation background and passing the secondary monochromator.)

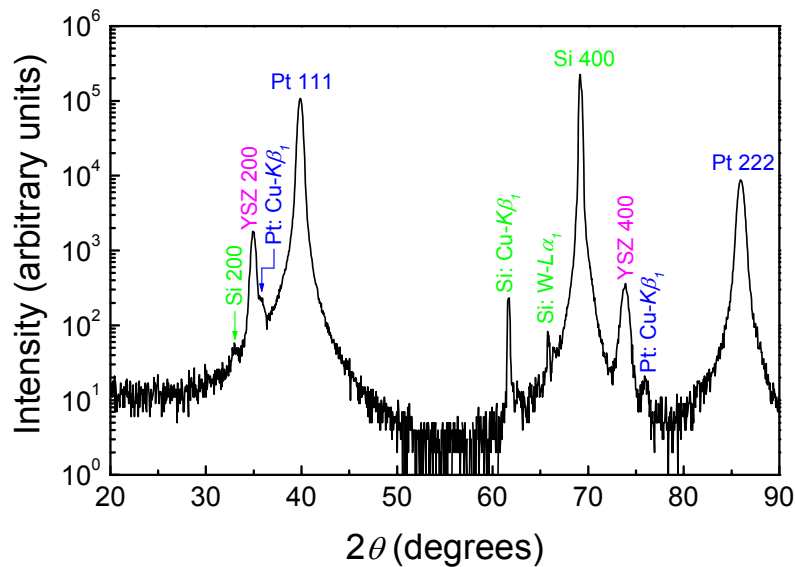


FIG. 5.1. X-ray diffraction θ - 2θ scan of a Pt film on a (100)-oriented YSZ buffered Si(100) substrate. The Cu- $K\beta_1$ lines are due to the remaining Cu- $K\beta_1$ radiation, and the W- $L\alpha_1$ lines are due to the tungsten contamination of the x-ray target by the tungsten cathode filament.

In order to determine whether the Pt/YSZ/Si heterostructure is epitaxial and to confirm the crystallographic orientation, XRD pole figures and ϕ scans were performed. Figure 5.2(a)

shows a pole figure of a Pt film on a (100)-oriented YSZ buffered Si(100) substrate. The fixed 2θ angle used to record the pole figure is 46.24° corresponding to the Pt 200 reflection. The pole figure was plotted with the pole distance angle $\psi=0^\circ$ (center) to $\psi=90^\circ$ (rim). 12 reflection peaks with a peak-to-peak separation of 30° between neighboring peaks are observed at $\psi\approx 55^\circ$ revealing that the Pt(111) thin film has a very good out-of-plane orientation ($\psi=90^\circ$ corresponds to the substrate surface being parallel to the plane defined by the incident and reflected x-ray beams). The Pt (111) plane is tilted by 54.7° away from the Pt (100) plane, which is parallel to the substrate surface. ϕ scans of the Pt film (upper scan) and the YSZ film (lower scan) were performed using the Pt 200 and the YSZ 111 reflections, respectively, as can be seen in Fig. 5.2(b), in order to establish the in-plane orientation relationship of the Pt film with respect to the underlying YSZ film. The fixed ψ angle is $\sim 55^\circ$ for both of them indicating that the Pt (111) plane is completely parallel to the YSZ (100) plane. Details on the in-plane orientation relationship between Pt(111) and YSZ(100) films will be discussed using the schematic drawing of their corresponding unit cells [see Fig. 5.3 later].

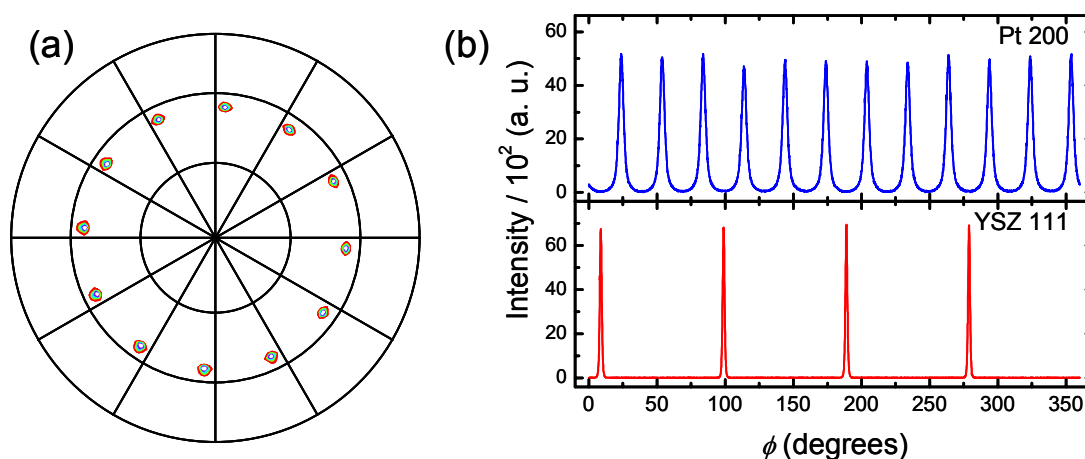


FIG. 5.2. X-ray diffraction (a) pole figure of the Pt 200 reflection, and (b) ϕ scans of the Pt 200 (upper) and the YSZ 111 (lower) peak of a Pt(111)/YSZ(100)/Si(100) heterostructure. The ϕ scans are performed at $\psi=54.7^\circ$.

As shown in the ϕ scan of the Pt 200 reflection [Fig. 5.2(b)], 12 peaks are detected from the (111)-oriented Pt film. These peaks correspond (a) to the well-known threefold symmetry of the (111) plane, and (b) to four different azimuthal positions of Pt(111) domains on the YSZ(100) surface. The 12 symmetric peaks in the ϕ scan of Fig. 5.2(b) provide reliable evidence for the specific in-plane triangle-on-cube epitaxy relation of the Pt(111) film on the YSZ(100) film illustrated in Fig. 5.3. In this figure, four types of azimuthally rotated domains (rotated in-plane by 0° , 90° , 180° , and 270° around the normal to the substrate surface) are schematically sketched. The four orientation variants result in the 12 reflections [Fig. 5.2(b)], with a characteristic separation angle of 30° between the neighboring peaks. From these XRD

results and the schematic drawing, the epitaxial orientation relationship between the Pt(111) and the YSZ(100) films is determined as $\text{Pt}(111)\parallel\text{YSZ}(100)$; $\text{Pt}[0\bar{1}1]\parallel\text{YSZ}\langle 001\rangle$, taking into account that the $\text{Pt}[0\bar{1}1]$ direction may be parallel to any of the four $[010]$, $[0\bar{1}0]$, $[001]$, and $[00\bar{1}]$ YSZ directions. The lattice mismatch value calculated along the $\text{Pt}[2\bar{1}\bar{1}]\parallel\text{YSZ}[001]$ direction is -6.5% ; that along the $\text{Pt}[0\bar{1}1]\parallel\text{YSZ}[010]$ direction is $+8.0\%$. A similar epitaxial growth trend of (111)-oriented Pt films on MgO(100) single crystal substrates prepared by electron beam evaporation [101] or rf magnetron sputtering [102] was reported before.

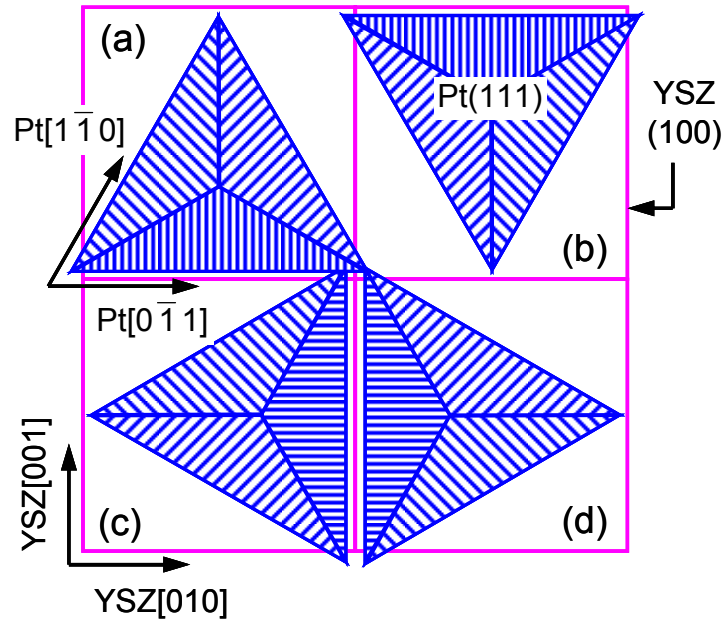


FIG. 5.3. Schematic drawing of the orientation relationship between the top Pt(111) film and the bottom YSZ(100) film. The Pt(111) plane is rotated in-plane by (a) 0° , (b) 180° , (c) 270° , and (d) 90° around the normal to the substrate surface. The squares represent unit cells of YSZ, seen along the $[100]$ direction. The hatched triangles represent unit cells of Pt, seen along the $[111]$ direction, whereby the hatched planes protrude out of and recede below the (100) YSZ plane, respectively.

Transmission electron microscopy

Figure 5.4 (a) shows a cross-sectional transmission electron microscopy (TEM) bright-field image of a 20 nm thick Pt film on a 35 nm thick YSZ buffer layer on Si(001). The inset shows the diffraction pattern, which is repeated in magnified form in Fig. 5.4(b), together with the indexation of some of the reflections. The exact cube-on-cube epitaxy of YSZ(001) on Si(001) is clearly revealed, visualized by the two green squares formed by the corresponding (400) and (040) reflections of Si and YSZ. Only one row of platinum reflections is seen, however, consisting of (111) and (222) Pt reflections on the vertical axis of the figure, which indicates that the (111) plane of platinum is parallel to the substrate surface. The absence of other Pt reflections is due to the specific azimuthal orientations of the Pt

domains, which obviously do not give diffraction spots in the case of the beam direction used. Figure 5.4(c) is a cross-sectional Pt dark-field image, and Fig. 5.4(d) a cross-sectional YSZ dark-field image of the same sample. The lateral size of the azimuthal Pt domains of between about 80 nm and about 150 nm, as well as their columnar structure (a domain extending from the Pt/YSZ interface to the top of the Pt layer), and the roughly perpendicular domain boundaries are well visible in Fig. 5.4(c). Most remarkably, the surface of the Pt electrode is plane and smooth, although a bit wavy [Fig. 5.4(c)], which should favor the growth of high-quality ferroelectric films on top of them. The YSZ dark-field image of Fig. 5.4(d) reveals the well-known columnar structure of the YSZ film, which consists of narrow columnar grains of about 5 nm diameter, extending from the lower to the upper interface.

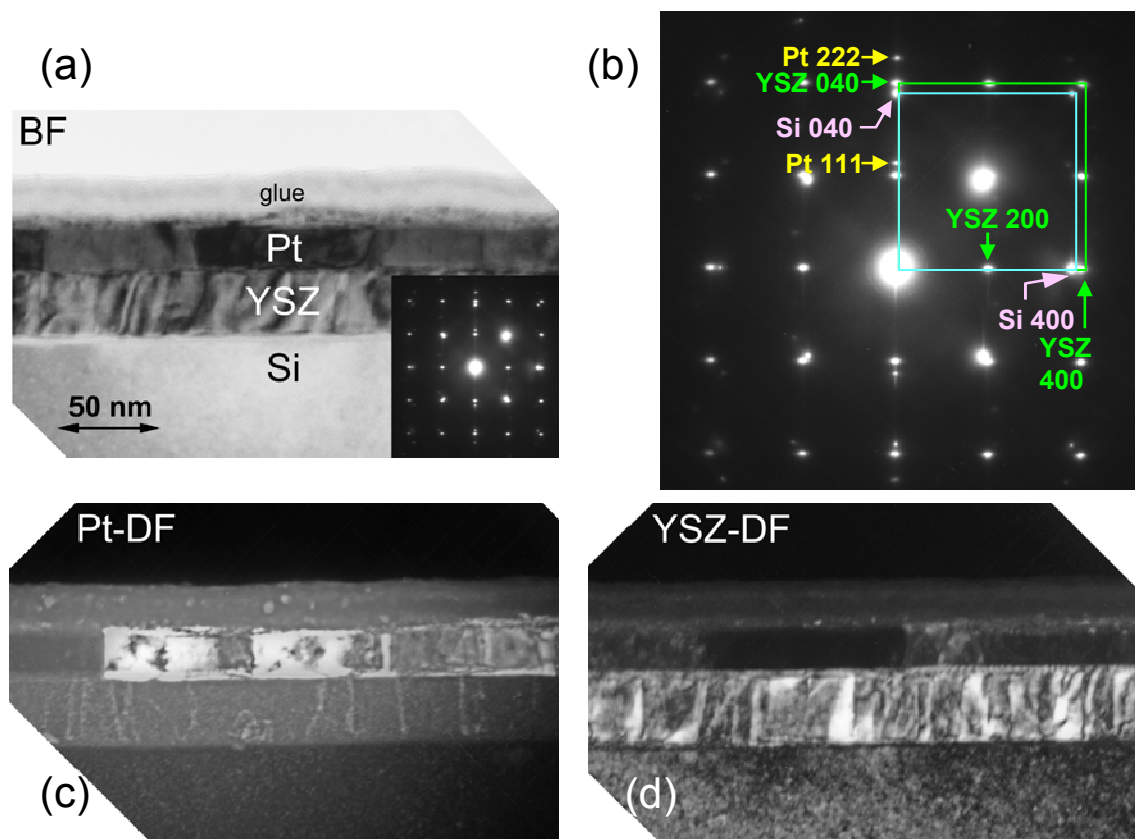


FIG. 5.4. (a) Cross-sectional TEM bright-field image and (b) magnified electron diffraction pattern from (a), of a Pt(111) film on aYSZ(100)/Si(100) substrate. (c) Cross-sectional Pt dark-field image, and (d) cross-sectional YSZ dark-field image of the same sample. The scale in (a) also refers to (c) and (d).

Figure 5.5(a) shows a plan-view TEM bright field image of the Pt(111) film; a corresponding Pt dark-field image is shown in Fig. 5.5(b). Both figures reveal the irregular shape and rather wide size variation of the azimuthal Pt domains. Single domains reach more than 200 nm in lateral size. Interestingly, the domain boundaries show a regular arrangement

of dislocations. This is certainly due to the regular character of the domain boundaries, the nature of which is equivalent to that of a twin boundary or a well-defined low-angle grain boundary. A more detailed characterization of the domain boundaries has not been performed, however.

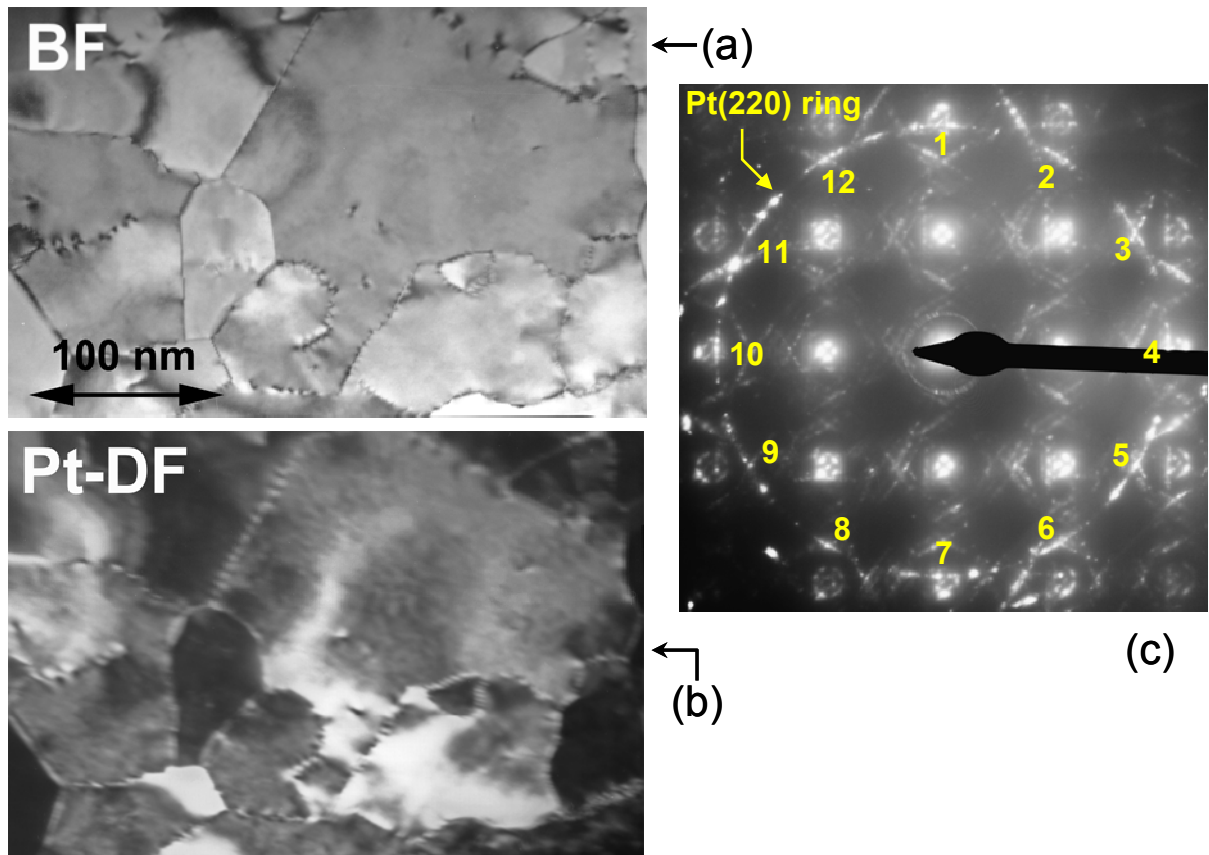


FIG. 5.5. Plan-view TEM (a) bright-field image and (b) dark-field image of the Pt(111) film on a YSZ(100)/Si(100) substrate. (c) Plan-view electron diffraction pattern of the sample.

Figure 5.5(c) shows a plan-view electron diffraction pattern of this sample. The quadratic spot patterns in this diffraction pattern originate from YSZ and Si, as well as from a double diffraction effect between them. At the radius of the Pt(220) ring, 12 bows (ring sections) are clearly seen, which obviously are an analogue to the 12 peaks of the platinum ϕ scan in Fig. 5.2(b). The following has to be taken into account: There are three different crystal planes of type $\{110\}$ perpendicular to the beam direction $[111]$ in a Pt single crystal. Considering the details of Fig. 5.3, this results in six azimuthally different planes of type $\{110\}$ in a Pt thin film consisting of four exactly oriented azimuthal domains. These six $\{110\}$ planes give 12 reflections of type $\{110\}$ in an electron diffraction pattern, due to the well-known 180° symmetry of all electron diffraction patterns. Thus the presence of four different azimuthal domains schematically shown in Fig. 5.3 is confirmed by the plan-view diffraction pattern of Fig. 5.4(c). However, the rather large length of each ring section speaks in favor of

some azimuthal spread (rotational freedom) of each of these azimuthal variants, giving rise to sort of a $\langle 111 \rangle$ texture of the Pt film. Considering, however, the sharpness of the 12 platinum peaks in Fig. 5.2(b), which speak in favor of exactly oriented azimuthal variants in that sample, one must assume that slight variations of the microstructural quality of the deposited Pt films have occurred. These variations have not been investigated in detail.

Overall, (111)-oriented Pt electrodes have been obtained on the YSZ(100)-buffered Si(100) substrate. To my knowledge, well-oriented Pt electrodes of this type have not been described before, except for a private communication, according to which similar Pt electrodes on YSZ(100) and YSZ(111) single crystals have been recently used by a group at Giessen University for electrochemical reasons [103].

5.2.2 Ferroelectric La- and Nd-substituted $\text{Bi}_4\text{Ti}_3\text{O}_{12}$ thin films

Figure 5.6 is a XRD θ - 2θ scan of a BLT thin film grown directly on a (111)-oriented Pt covered electrode on a YSZ(100)-buffered Si(100) substrate by PLD. The scan reveals peaks of a polycrystalline BLT film having (117), (001), and (014) orientations. This is similar to BLT films deposited on conventional (111) fiber-textured Pt-coated Ti/SiO₂/Si(100) substrates by chemical solution deposition [36] or PLD [47]. From the scan it is found that the epitaxial growth of ferroelectric films of bismuth layered perovskite oxides is very difficult directly on even very smooth (111)-oriented Pt electrodes.

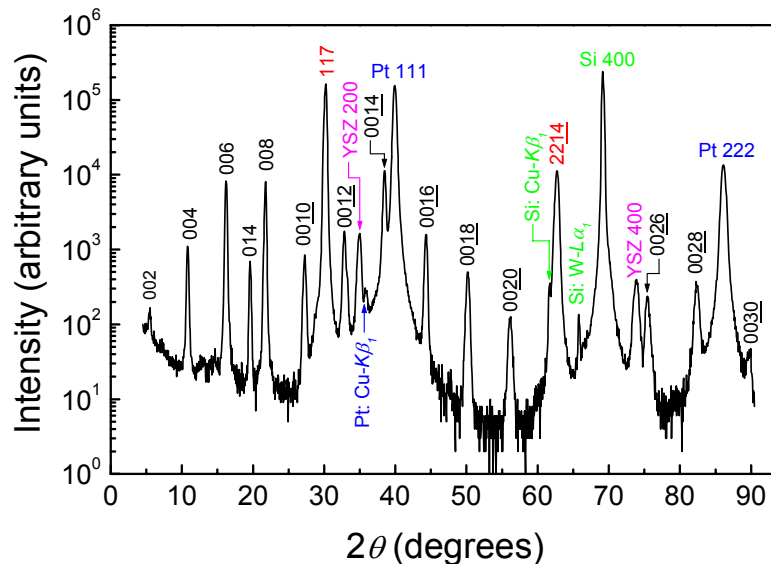


FIG. 5.6. X-ray diffraction θ - 2θ scan of a BLT film on a (111)-oriented Pt-covered YSZ(100)/Si(100) substrate (without SrRuO₃ layer). The Cu- $K\beta_1$ lines are due to the remaining Cu- $K\beta_1$ radiation, and the W- $L\alpha_1$ lines are due to the tungsten contamination of the x-ray target by the tungsten cathode filament.

As mentioned earlier, SrRuO₃ films having a perovskite structure similar to bismuth-layered perovskite oxides, as well as a good lattice match with Pt films, should be favorable for the epitaxial growth of BLT films. Therefore the (111)-oriented Pt films were covered with (111)-oriented SrRuO₃ layers.

Figure 5.7(a) is a cross-sectional TEM dark-field image, taken in two nearby SrRuO₃ and Pt reflections. Figure 5.7(b) shows a plan-view electron diffraction pattern of this sample. In addition to the Si and YSZ quadratic spot pattern, two rings consisting of 24 short segments are visible. (The third faint ring is not being considered here.) Comparing with Fig. 5.5(c), where only the Pt(220) ring is present, one comes to the conclusion that the outer ring in Fig. 5.7 (b) corresponds to the Pt(220) ring and should thus coincide with the SrRuO₃(220) ring (in pseudocubic indexing).

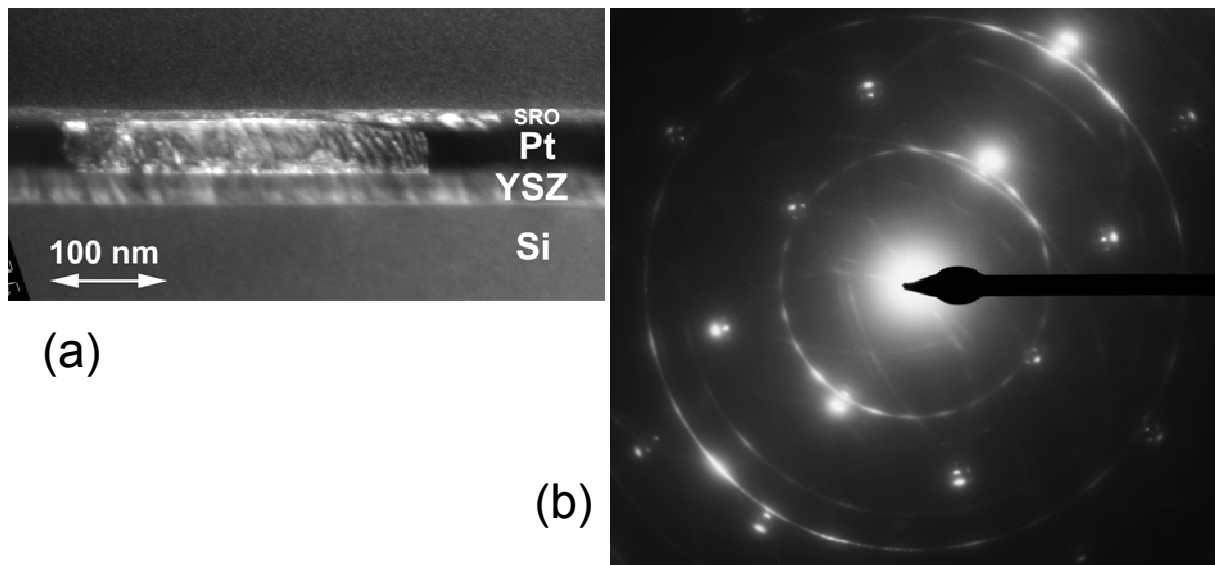


FIG. 5.7. (a) Cross-sectional TEM dark-field image of a SrRuO₃/Pt/YSZ/Si(100) structure, taken in two nearby SrRuO₃ and Pt reflections. (b) Plan-view electron diffraction pattern of this sample.

The cubic lattice parameter of Pt ($a_p=0.3923$ nm) is very close to the pseudocubic lattice parameter of SrRuO₃ ($a_s=0.3928$ nm) resulting in the coincidence of the corresponding diffraction rings. The Pt(110) ring being forbidden, however, the inner ring can result only from SrRuO₃(110) (in pseudocubic indexing). Since SrRuO₃ in fact is non-cubic, the extinction rule for f.c.c. metals is not applicable to this ring. On the other hand, the fact that along the SrRuO₃(110) ring 24 ring sections occur, instead of 12 ring sections seen in Fig. 5.5(c) for Pt, is certainly also a consequence of the non-cubic, orthorhombic character of SrRuO₃. Accordingly, the schematic drawing of Fig. 5.3 (for Pt) should be modified, taking the orthorhombicity of SrRuO₃ into account. Most probably a corresponding modification would result in 12 azimuthal domain variants of the SrRuO₃(111) film. Details of this modification and of the diffraction patterns have, however, not been considered, because the

SrRuO₃ layer has been used here solely under the useful aspect of lattice fit with both Pt and BNT/BLT. As the following paragraphs will show, this role has been indeed fulfilled by the (111)-oriented SrRuO₃ layers. It can be expected that the details of its microstructure should, in principle, be most similar to that of the (111)-oriented Pt layer.

θ - 2θ and ω scans

Bi₄Ti₃O₁₂ crystallizes in a monoclinic lattice, which for simplicity can, however, be considered pseudo-orthorhombic. BLT and BNT have been reported to be orthorhombic. The corresponding lattice parameters are $a_L = 0.542$ nm, $b_L = 0.5415$ nm, $c_L = 3.289$ nm for Bi_{3.25}La_{0.75}Ti₃O₁₂ [35,81], and $a_N = 0.5429$ nm, $b_N = 0.54058$ nm, and $c_N = 3.2832$ nm for Bi_{3.6}Nd_{0.4}Ti₃O₁₂ [104]. I have not determined the exact chemical composition of my BLT and BNT films. However, considering the composition of the targets given above, and the lattice parameters determined from XRD and selected-area electron diffraction, I concluded that the composition is close to the nominal formulas Bi_{3.25}La_{0.75}Ti₃O₁₂ and Bi_{3.54}Nd_{0.46}Ti₃O₁₂, respectively. BLT and BNT films turned out to be most similar to each other, with respect to their orientation relationship, morphology, and microstructure, although somewhat different in the ferroelectric properties.

Figure 5.8 shows XRD θ - 2θ scans of (a) BLT films and (b) BNT films deposited on (111)-oriented SrRuO₃-covered Pt(111)/YSZ(100)/Si(100) substrates at substrate temperatures in the range of 500–825 °C. One can see that the θ - 2θ scan in Fig. 5.8(a) is completely different from that of a BLT film directly grown on Pt/YSZ/Si(100) in Fig. 5.6. This means that SrRuO₃ plays an important role in growing epitaxial films of bismuth-layered perovskite oxides. Asayama *et al.* reported that (103)-oriented fiber-textured SrBi₂Nb₂O₉ films were grown on (111)-oriented fiber-textured Pt-coated Si(100) substrates using a SrRuO₃ buffer layer as a template [105]. In addition, the epitaxial growth of YBa₂Cu₃O_{7- δ} thin films on epitaxial SrRuO₃(100) films on Pt(100)/MgO(100) substrates by PLD was reported [106]. Since the lattice mismatch between SrRuO₃ ($a_S=0.3928$ nm) and Pt ($a_P=0.3923$ nm) is only 0.13%, the orientation of SrRuO₃ is identical with that of Pt, as can be seen in Fig. 5.8. In both cases of BLT and BNT films deposited at 500 °C, the low intensities of the 014 peaks indicate that the onset of crystallization of these films might be around 500 °C under my growth conditions. (The 208 and 4016 peaks are hidden behind the Pt 111 and Pt 222 peaks, respectively.) I found that the films exhibit high crystallinity as the deposition temperature of the films increases. However, I also found that above about 800 °C a small amount of impurity phases exists for both BLT and BNT films. Especially in the case of BNT films, above 800 °C an unidentified sharp peak at $2\theta \approx 30.1^\circ$ is observed, but this peak might also be due to a 117 orientation. Figure 5.9(a) shows full width at half maximum (FWHM) values in the XRD 2θ scans of the 014 peak as a function of the deposition temperature. BNT films

exhibit higher crystallinity than BLT films. Based on the results of the θ - 2θ scans, the crystallographic orientation relationship between the films and the substrates can be derived as BLT(104);BNT(104)||SrRuO₃(111)||Pt(111)||YSZ(100)||Si(100).

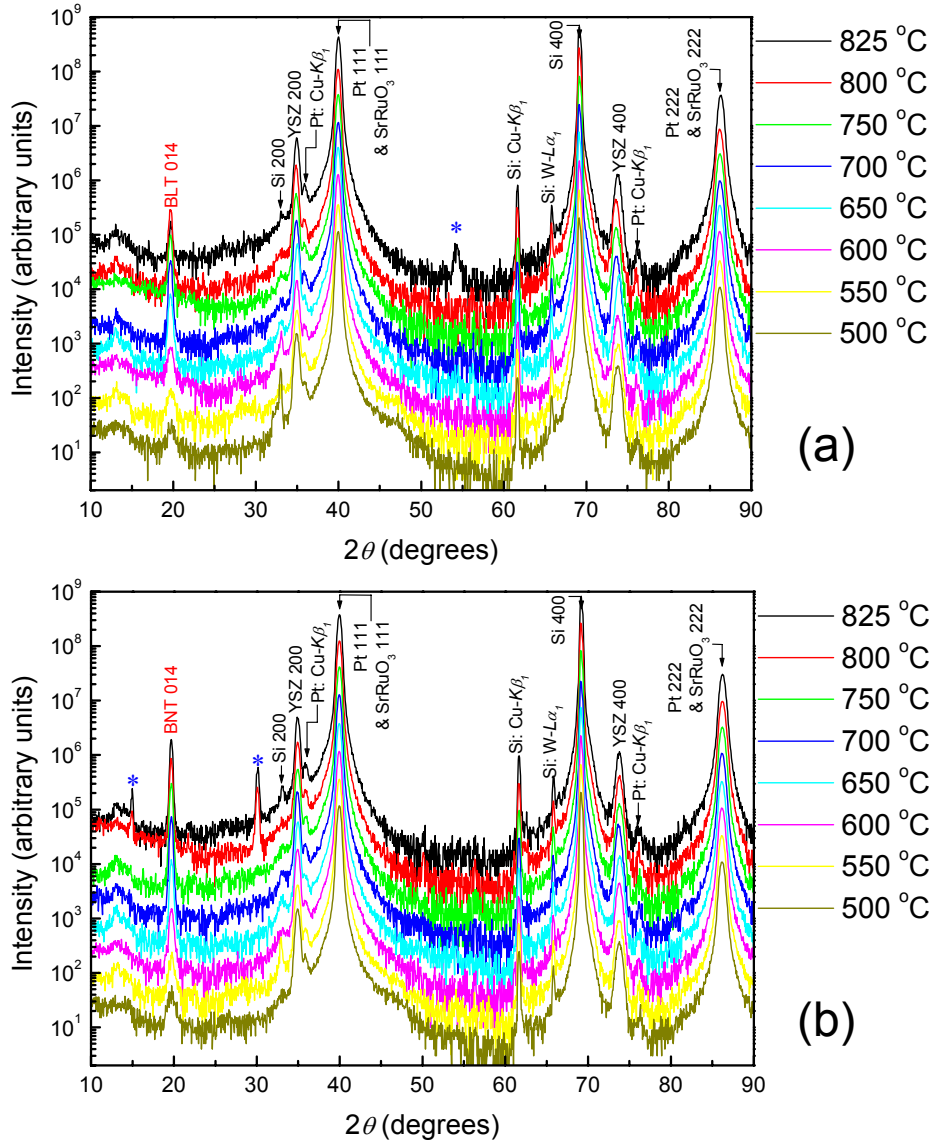


FIG. 5.8. X-ray diffraction θ - 2θ scans of (a) BLT films and (b) BNT films on SrRuO₃(111)-covered Pt(111) electrodes on YSZ(100)/Si(100) substrates with various deposition temperatures. The peaks of unidentified phases are labeled as (*).

XRD ω scans were carried out in order to characterize the epitaxial quality of the films depending on the deposition temperature, and moreover to make a comparison between BLT films and BNT films deposited on identical substrates. Figures 5.9(b) and 5.9(c) show ω scans of the BLT 014 peak [Fig. 5.9(b)] and the BNT 014 peak [Fig. 5.9(c)] as a function of the deposition temperature. Compared with ω scans of BLT films, BNT films show somewhat sharper reflection peaks than BLT films. As roughly expected from the FWHM values in 2θ

scans [Fig. 5.9(a)], it is found that the BNT films have a somewhat higher epitaxial quality than the BLT films, as can be seen from the lower FWHM values in ω scans [Fig. 5.9(d)]. For example, BLT and BNT films deposited at 750 °C revealed FWHM values of 1.99° and 1.24° in the ω scans, respectively. A detailed consideration of the temperature dependence of the film quality and of the optimum substrate temperature for BNT and BLT films, respectively, will be given in the next paragraph.

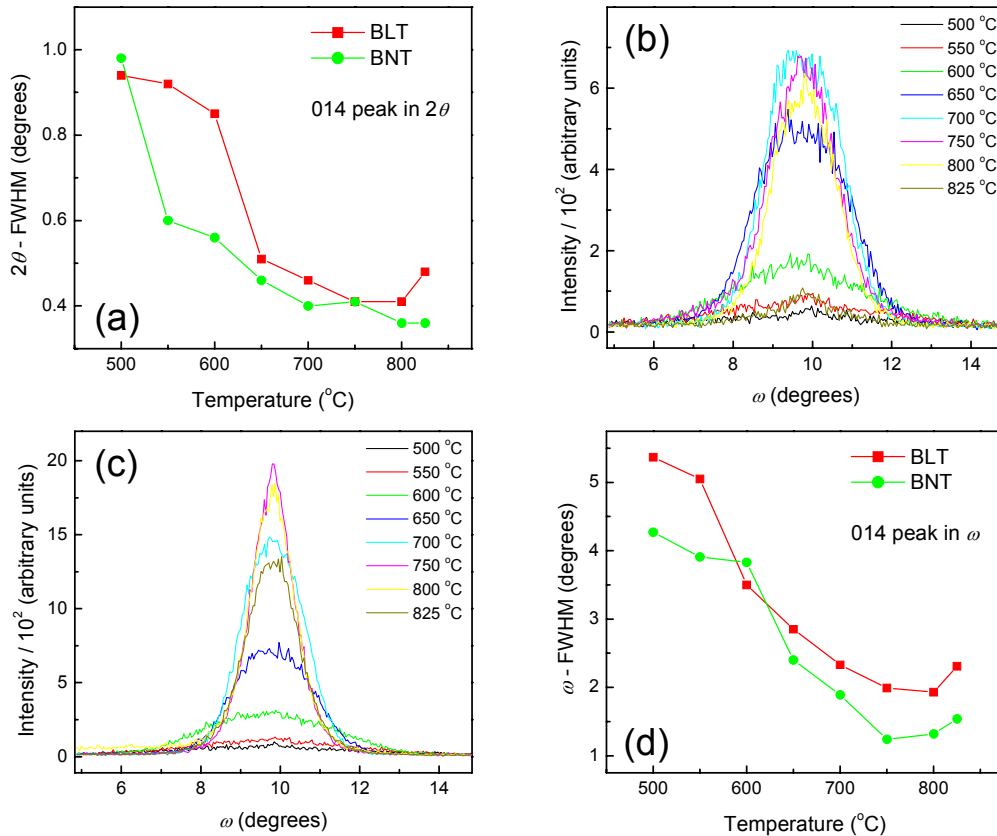


FIG. 5.9. (a) Substrate temperature dependence of 2θ -FWHM, [(b) and (c)] ω scans, and (d) substrate temperature dependence of ω -FWHM (of the BLT;BNT 014 peak) for BLT films and BNT films grown at various substrate temperatures on SrRuO₃(111)/Pt(111)/YSZ(100)/Si(100) substrates.

Pole figures and ϕ scans

For both BLT and BNT films, in order to determine the epitaxial growth and confirm the crystallographic orientations various pole figure analyses were performed. Figure 5.10 shows pole figures of BLT films [Figs. 5.10(a) and 5.10(c)] and BNT films [Figs. 5.10(b) and 5.10(d)]. BLT and BNT films deposited at a substrate temperature of 750 °C were selected to record the scans because they show high crystallinity as well as pure phase formation at this growth temperature. The fixed 2θ values used to record the pole figures were 30.1° [Figs.

5.10(a) and 5.10(b)] and 23.31° [Figs. 5.10(c) and 5.10(d)] corresponding to the 117 reflection and the 111 reflection, respectively. In the pole figures of the 117 reflection [Figs. 5.10(a) and 5.10(b)], four sets of 12 peaks recorded at $\psi \approx 36^\circ$ and 84° correspond to the $11\bar{7}/1\bar{1}\bar{7}$ reflections and to the $11\bar{7}/1\bar{1}\bar{7}$ reflections, respectively [cf. the angles $\angle (104) : (11\bar{7}) = 36.4^\circ$, $\angle (104) : (1\bar{1}\bar{7}) = 36.4^\circ$, $\angle (104) : (11\bar{7}) = 84.1^\circ$, and $\angle (104) : (1\bar{1}\bar{7}) = 84.1^\circ$]. These pole figures for both BLT and BNT films indicate that the (104) plane is parallel to the substrate plane and that the (104)-oriented films involve twelve different azimuthal domain variants. The BLT and BNT films inherit these 12 variants from the corresponding azimuthal domain variants of the SrRuO₃ layer. The latter go in turn back to the azimuthal domain variants of the Pt(111) films. The Pt(111) surface has a threefold symmetry, which is valid for each of the four azimuthal domain variants according to Figs. 5.2 and 5.3. Accordingly, 12 azimuthal domain variants result in the (non-cubic) SrRuO₃ films, and finally also in the BNT and BLT films. Each of these 12 variants has an azimuthal angular distance of 30° from its neighbors. Accordingly, a symmetry based on 30° angular distances is visible in the pole figures. A careful evaluation of the pole figures in Fig. 5.10 requires the consideration of the following details. Figures 5.10(e) and 5.10(f) show the simulated pole figures using 117 and 111 reflections of a (104)-oriented film, respectively, when one single domain of the film is grown.

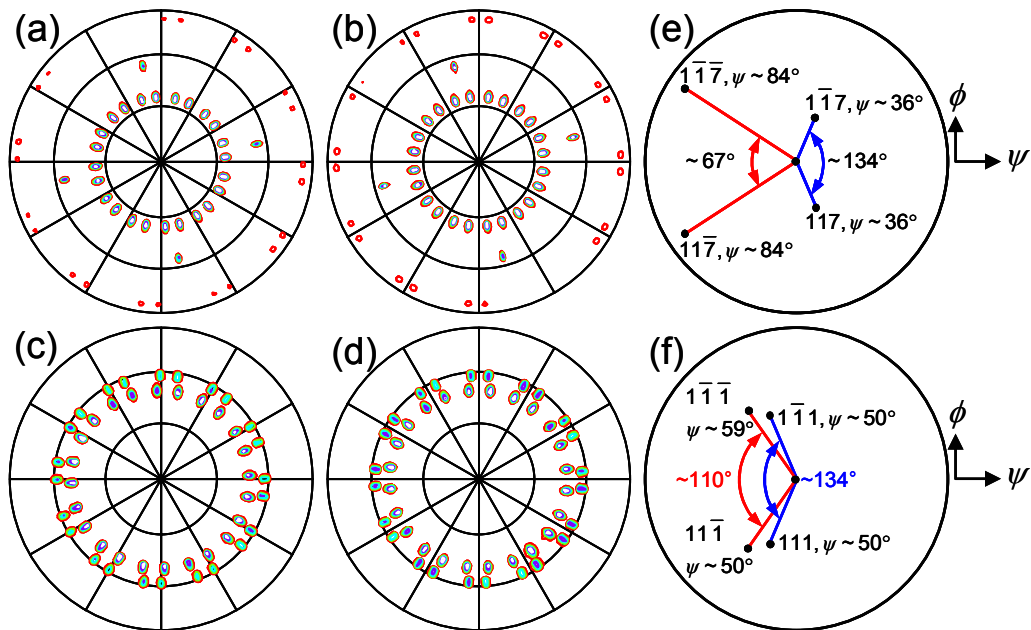


FIG. 5.10. X-ray diffraction pole figures of a BLT film [(a) and (c)] and of a BNT film [(b) and (d)] on SrRuO₃(111)/Pt(111)/YSZ(100)/Si(100) substrates. The fixed 2θ angles were 30.1° [(a) and (b)] and 23.31° [(c) and (d)] corresponding to the 117 reflection and the 111 reflection, respectively. [(e) and (f)] Pole figure simulations using (e) the 117 reflection and (f) the 111 reflection.

Since the azimuthal angle difference between the 117 and the $1\bar{1}\bar{7}$ reflections is $\sim 134^\circ$ [cf. Fig. 5.10(e)], the peaks at $\psi \sim 36^\circ$ have peak-to-peak separation angles of $\Delta\phi \approx 134^\circ - (4 \cdot 30^\circ) = 14^\circ$ and $\Delta\phi \approx [(4+1) \cdot 30^\circ] - 134^\circ = 16^\circ$ between neighboring peaks. In addition, the peaks at $\psi \sim 84^\circ$ are separated by $\Delta\phi \approx 67^\circ - (2 \cdot 30^\circ) = 7^\circ$ and $\Delta\phi \approx [(2+1) \cdot 30^\circ] - 67^\circ = 23^\circ$ resulting from the azimuthal angle difference of $\sim 67^\circ$ between the $11\bar{7}$ reflection and the $1\bar{1}\bar{7}$ one. (Four peaks with a single-domain situation are recorded at $\psi \sim 55^\circ$ corresponding to the YSZ 111 reflection, confirming that the YSZ (100) plane is parallel to the substrate plane.)

Although the pole figures of the 117 reflection are sufficient to identify the crystallographic orientations, I further examined the films recording one more pole figure using the 111 reflection to independently confirm the results [Figs. 5.10(c) and 5.10(d)]. In these pole figures, there are also four sets of 12 peaks at $\psi \sim 50^\circ$ and 59° corresponding to the $111/1\bar{1}\bar{1}$ and $11\bar{1}/1\bar{1}\bar{1}$ reflections, respectively [cf. the angles $\angle (104) : (111) = 49.7^\circ$, $\angle (104) : (1\bar{1}\bar{1}) = 49.7^\circ$, $\angle (104) : (11\bar{1}) = 58.8^\circ$, and $\angle (104) : (1\bar{1}\bar{1}) = 58.8^\circ$]. Since the azimuthal angle difference between the 111 and the $1\bar{1}\bar{1}$ reflection is $\sim 134^\circ$ [cf. Fig. 5.10(f)], the peaks at $\psi \sim 50^\circ$ have peak-to-peak separation angles of $\Delta\phi \approx 134^\circ - (4 \cdot 30^\circ) = 14^\circ$ and $\Delta\phi \approx [(4+1) \cdot 30^\circ] - 134^\circ = 16^\circ$ between the neighboring peaks. The peaks at $\psi \sim 59^\circ$ are separated by $\Delta\phi \approx 110^\circ - (3 \cdot 30^\circ) = 20^\circ$ and $\Delta\phi \approx [(3+1) \cdot 30^\circ] - 110^\circ = 10^\circ$ resulting from the azimuthal angle difference of $\sim 110^\circ$ between $11\bar{1}$ and $1\bar{1}\bar{1}$ reflections. The pole figures [Figs. 5.10(c) and 5.10(d)] thus confirm the (104) orientation of the BLT and BNT films, and also the presence of 12 azimuthal domain variants in the latter. Pole figures of threefold symmetry were recorded in (104)-oriented BLT films grown on SrRuO₃(111)-covered SrTiO₃(111) substrates made by PLD [95,97] and in (028)-oriented BLT films grown on GaN(002) on Al₂O₃(0006) by PLD [107].

Furtheron, various ϕ scans of the BLT;BNT/SrRuO₃/Pt/YSZ/Si heterostructures were recorded to establish the in-plane orientation relationships of the BLT and BNT films with respect to their corresponding underlying layers. Figure 5.11 shows ϕ scans of (a) Si 111, (b) YSZ 111, (c) Pt 200/SrRuO₃ 200, (d) BLT;BNT 0014, and (e) BLT;BNT 117/ $1\bar{1}\bar{7}$ reflections. The fixed ψ angles used to record the ϕ scans of the 0014 and $117/1\bar{1}\bar{7}$ reflections were 56.4° and 36.4° , respectively, for both the BLT and BNT films. The reflections were recorded at fixed ψ angles of 54.7° for the other materials. As already reported [67], a YSZ(100) film on a Si(100) substrate shows a fourfold growth symmetry revealing a cube-on-cube epitaxy relationship as shown in Figs. 5.11(a) and 5.11(b).

From the ϕ scan of the Pt 200 reflections at $\psi = 54.7^\circ$ shown in Fig. 5.11(c), the epitaxial growth was confirmed for the Pt(111) films on the YSZ(100) films, with the corresponding epitaxial relationship Pt(111)||YSZ(100); Pt[$0\bar{1}\bar{1}$]|YSZ<001> [For details see section 5.2.1].

A triple-domain situation of the BLT and BNT films on each of the four azimuthal domain variants of the Pt(111) films was confirmed for the (104)-oriented BLT and BNT films on the SrRuO₃/Pt/YSZ/Si heterostructure, as shown in the ϕ scans of the 0014 and 117 reflections of Figs. 5.11(d) and 5.11(e). The (104)-oriented films consist of twelve

corresponding azimuthal domain variants. (As mentioned before, the ϕ scans of BLT and BNT films shown in Fig. 5.11(e) show two sets of twelve peaks separated by every 30° corresponding to $11\bar{7}$ and $1\bar{1}7$ reflections.)

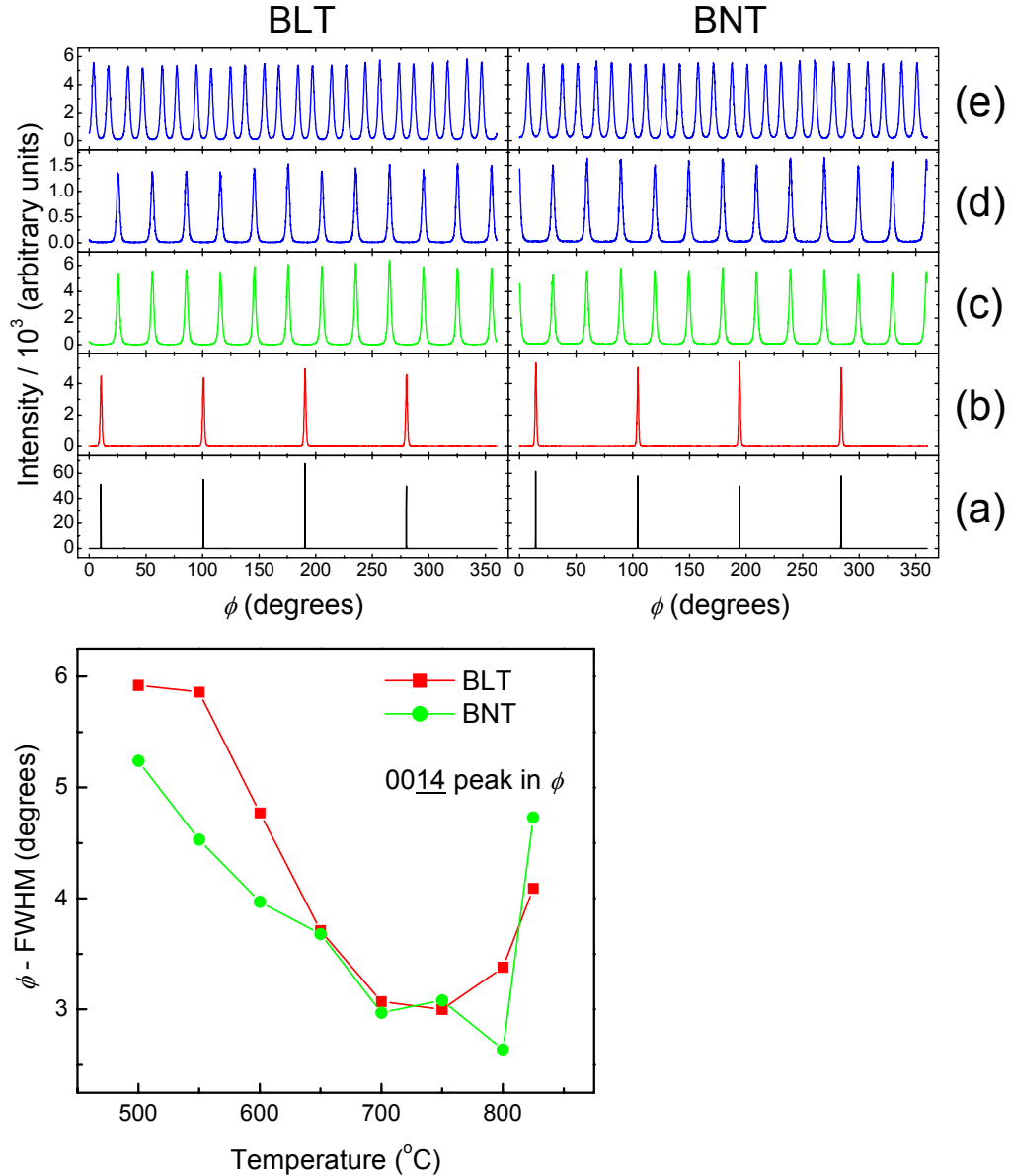


FIG. 5.11. [(a) to (e)] X-ray diffraction ϕ scans of a BLT film (left-hand side) and a BNT film (right-hand side) on SrRuO₃(111)/Pt(111)/YSZ(100)/Si(100) substrates. The ϕ scans were performed using (a) Si 111, (b) YSZ 111, (c) Pt 200/SrRuO₃ 200, and (d) BLT;BNT 001₄, and (e) BLT;BNT 11 $\bar{7}$ /1 $\bar{1}7$ reflections. The fixed ψ angles were 54.7° for Figs. 5.11(a) to 5.11(c), 56.4° for Fig. 5.11(d), and 36.4° for Fig. 5.11(e). (f) Substrate temperature dependence of FWHM values of the 001₄ reflection in ϕ scans for BLT films and BNT films grown at various deposition temperatures.

Based on all the XRD characterizations, the epitaxial relationship between the films and the substrates can be derived as follows:

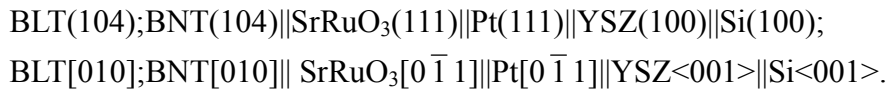


Figure 5.11(f) shows FWHM values in the ϕ scans using the BLT;BNT 0014 peak of BLT films and BNT films deposited on identical SrRuO₃(111)/Pt(111)/YSZ(100)/Si(100) substrates as a function of the deposition temperature. Both BLT and BNT films deposited at around 700–750 °C showed a good in-plane alignment. At low deposition temperatures BNT films show a better quality of the in-plane orientation than BLT films, which is consistent with the FWHM values in the 2θ and ω scans. Considering the overall FWHM values in 2θ , ω , and ϕ scans, a high quality of the films can be obtained at deposition temperatures between 700 and 750 °C.

Atomic force microscopy

In order to compare microstructural features of the BLT and BNT films, AFM investigations were performed as shown in Figs. 5.12 and 5.13.

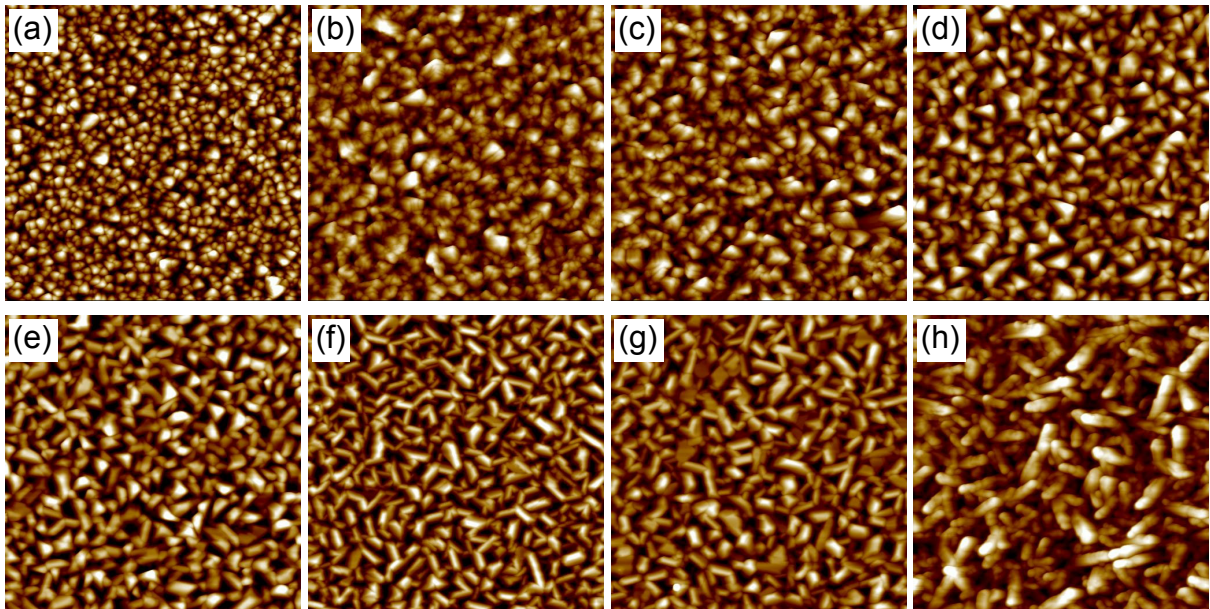


FIG. 5.12. AFM topography images (image size: $3 \times 3 \mu\text{m}^2$) of BLT films grown at different substrates (a) 500, (b) 550, (c) 600, (d) 650, (e) 700, (f) 750, (g) 800, and (h) 825 °C on (111)-oriented SrRuO₃-covered Pt(111)/YSZ(100)/Si(100) heterostructural substrates.

Figure 5.12 shows AFM topography images of BLT films grown at various substrate temperatures. As the substrate temperature increases, the appearance of a triangular grain morphology is clearly observed up to 700 °C which is certainly due to the threefold symmetry of the SrRuO₃(111) surface and/or the corresponding symmetry of the BLT(104) plane, which is a derivative of the (111) perovskite plane. The increasing grain size in Fig. 5.12 with increasing temperature is in good agreement with the XRD results on decreasing FWHM values related to the grain size. Above a substrate temperature of 750 °C, the triangular grains gradually evolve to needlelike grains which are arranged along certain directions with azimuthal angle differences of integral multiples of 30°.

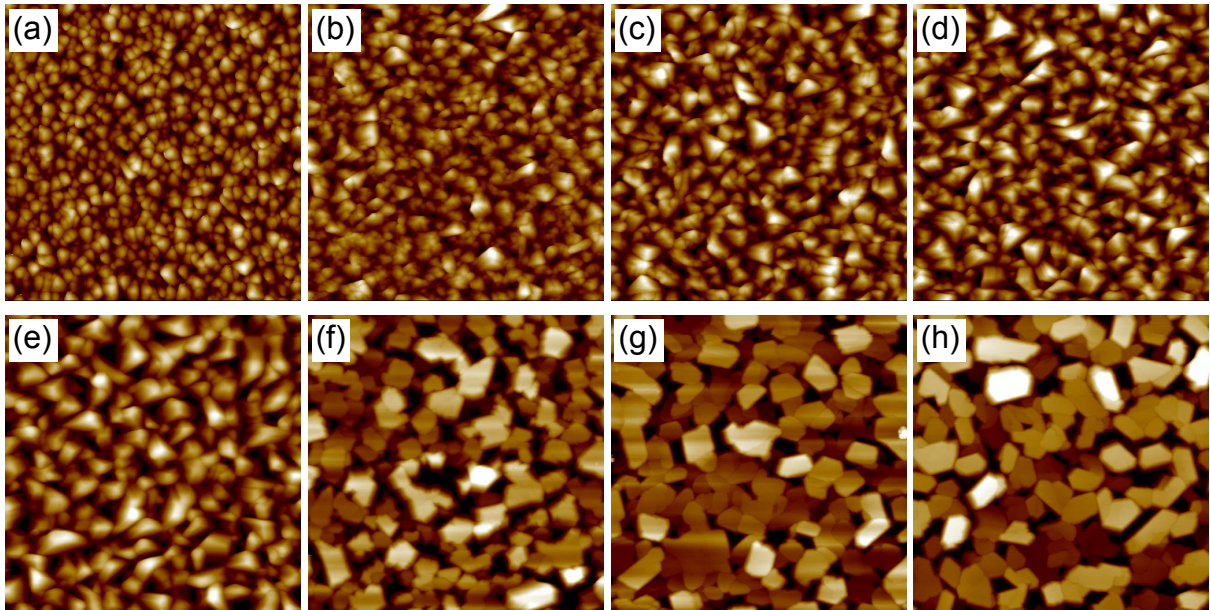


FIG. 5.13. AFM topography images (image size: $3 \times 3 \mu\text{m}^2$) of BNT films grown at different substrates (a) 500, (b) 550, (c) 600, (d) 650, (e) 700, (f) 750, (g) 800, and (h) 825 °C on (111)-oriented SrRuO₃-covered Pt(111)/YSZ(100)/Si(100) heterostructural substrates.

Figure 5.13 shows AFM topography images of BNT films grown at different substrate temperatures revealing the distribution of triangular grains as well. Compared to the size of the grains of the BLT films, larger grains are observed in BNT films. This is in good agreement with the XRD results, according to which lower FWHM values were recorded in BNT films in 2θ , ω , and ϕ scans compared to BLT films. Unlike the surface morphology of the BLT films, platelike grains with polyhedral shape were clearly observed in BNT films above a substrate temperature of 750 °C. However as can be seen in detail, a small amount of these platelike grains is also observed at the surface of BLT films grown at 750 and 800 °C. Most similar platelike grains have been reported in epitaxial Ba₂BiTi₅O₁₈ films deposited on LaNiO₃/CeO₂/YSZ/Si(100) substrates by PLD [108] and Sr_{0.51}Ba_{0.48}La_{0.01}Nb₂O₆ films deposited on Pt/Ti/SiO₂/Si(100) substrates by PLD [109]. The origin of the distinct difference

of grain evolution between BLT and BNT films at rather high substrate temperatures requires further investigations.

Transmission electron microscopy

Figure 5.14(a) shows a cross-sectional TEM image of a 220 nm thick (104)-oriented BLT film on SrRuO₃(111)/Pt(111)/YSZ(100)/Si(100). The BLT film consist of large elongated grains about 100 to 200 nm in lateral size. The surface morphology of the BLT film is determined by the shapes of the grains, resulting in a rather rough surface. Some voids of about 40 nm lateral size and 20 nm height are visible at the bottom of the Pt layer, which most probably result from the fact that the SrRuO₃-covered Pt/YSZ/Si(100) substrate had been heated to the rather high temperature of 700 °C during BLT deposition. Some recrystallization of the Pt layer may have occurred at this high temperature, resulting in the condensation of some free volume into large voids. Figure 5.14(b) taken at higher magnification reveals the Bi₂O₂ layers or (002) planes within a BLT grain. These planes are at an angle of 56.4° with the (104) plane, i.e., with the substrate plane. Planar crystal defects, most probably stacking faults, intergrowth defects, and/or out-of-phase boundaries, are clearly visible in the otherwise rather regular pattern of the (002) planes. For details of such specific crystal defects, which are well known from the bismuth-layered perovskite materials, see Refs. 93, 110, and 111. Apart from these lattice defects, the well-pronounced parallel structure of the (002) planes confirms the good crystallinity of the BLT films. As a comparison of Figs. 5.14(a) and 5.14(b) shows, the (001) plane seems to be a favorable habit plane of the BLT grains, resulting in a tilted by about 55° appearance of the overall grain morphology. The inset of Fig. 5.14(b) shows the selected-area electron diffraction pattern of the grain seen in the image (and its surroundings), revealing the narrow-spaced (00*l*) row of diffraction spots. For a particular direction of the electron beam, i.e., for a particular sample tilt, this regular type of diffraction pattern [showing the (00*l*) spots, and the corresponding images revealing the (002) Bi₂O₂ planes] can at best be seen in only 2/12 or 16.7% of the grains, because the other 83.3% of the grains have a different azimuth and thus the beam direction is different with respect to their own lattice.

Figure 5.15(a) shows a corresponding cross-sectional image of a 240 nm thick (104)-oriented BNT film on SrRuO₃(111)/Pt(111)/YSZ(100)/Si(100). The overall characteristics of the BNT film are similar to those of the BLT film. The BNT film, too, consists of large elongated grains of about 100 nm lateral size, and the surface morphology of the BNT film is also determined by the shapes of the grains, resulting in a very rough surface. The BNT grains have, however, a somewhat larger aspect ratio (length-to-diameter ratio). As for the BLT film, the (001) plane seems to be a favorable habit plane of the BNT grains [Fig. 5.15(a)], however, two senses of the tilt of about 55° are visible, reflecting two (out of 12) different azimuthal domain variants. These two variants are related to each other as twins.

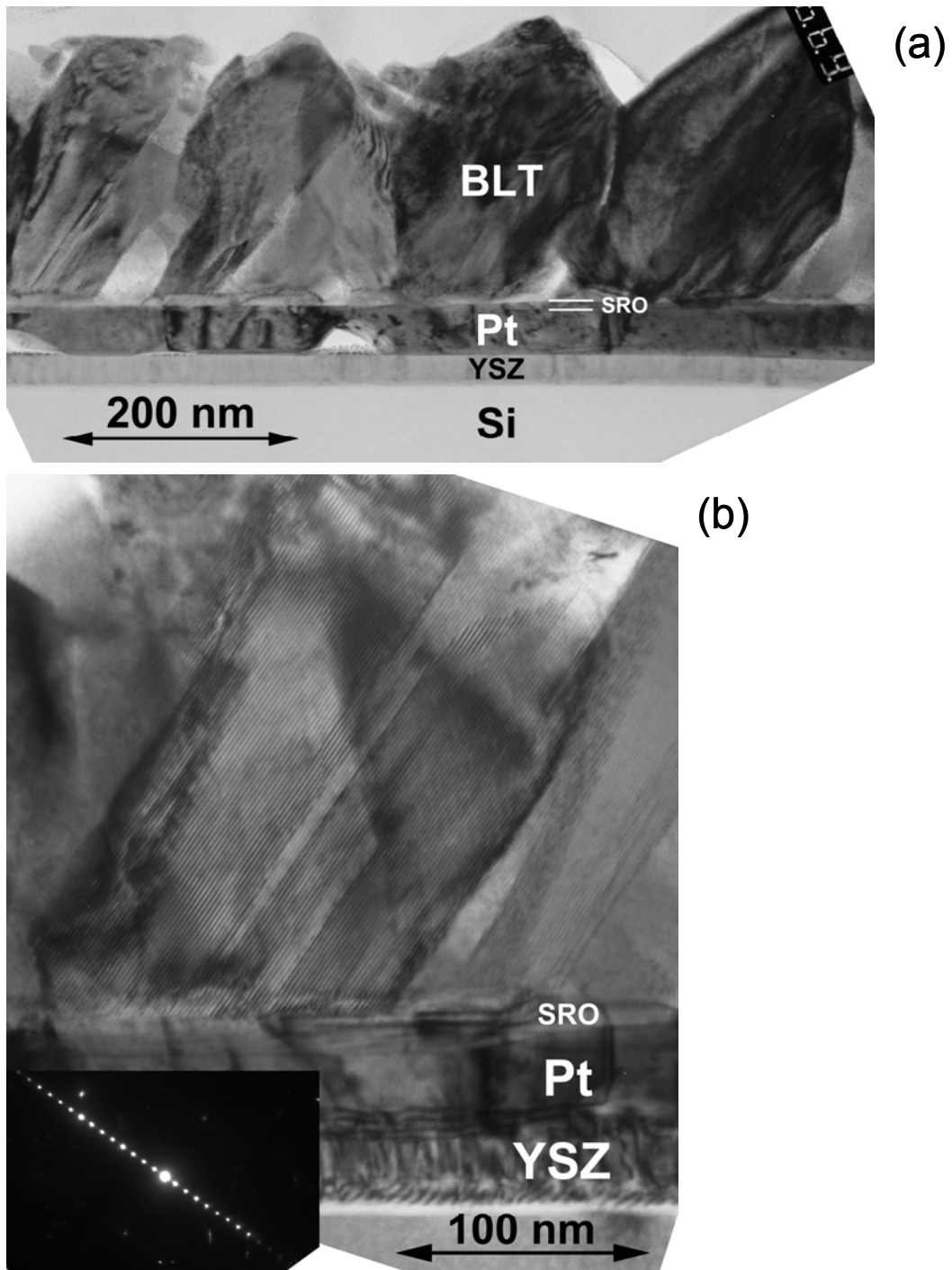


FIG. 5.14. [(a) and (b)] Cross-sectional TEM images and electron diffraction pattern [inset in (b)] of a (104)-oriented BLT film on SrRuO₃(111)-covered Pt(111)/YSZ(100)/Si(100). (b) Magnified detail revealing the BLT (002) planes and corresponding electron diffraction pattern (inset).

No voids have been found in the Pt layer of this sample. Figure 5.15(b) taken at higher magnification reveals the Bi₂O₂ layers or (002) planes within a single BNT grain, similarly to those within a BLT grain of Fig. 5.14(b). Again these planes are at an angle of 56.4° with the (104) plane, i.e., with the substrate plane. The inset of Fig. 5.15(b) shows the selected-area

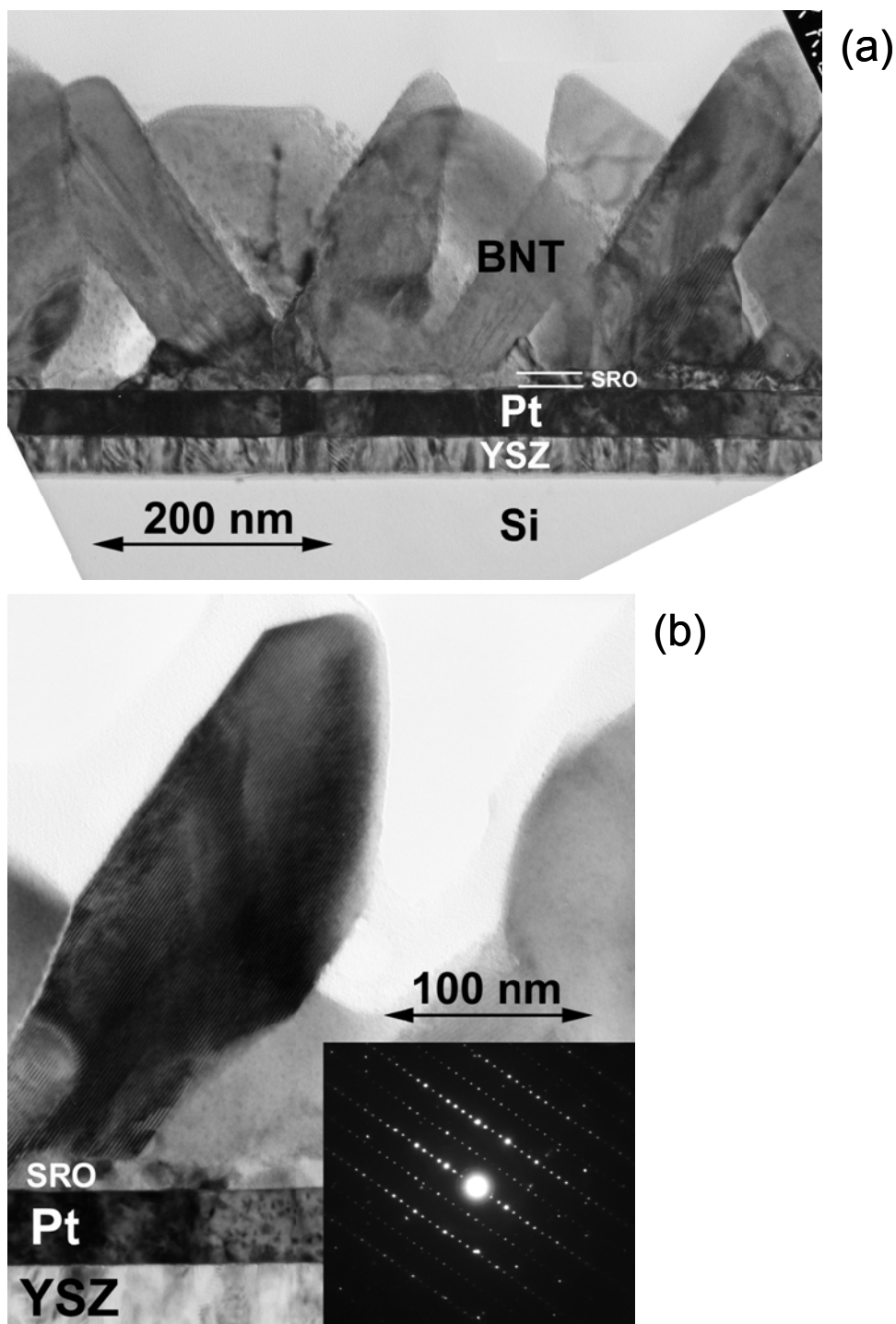


FIG. 5.15. [(a) and (b)] Cross-sectional TEM images and electron diffraction pattern [inset in (b)] of a (104)-oriented BNT film on SrRuO₃(111)-covered Pt(111)/YSZ(100)/Si(100). (b) Magnified detail revealing the BLT (002) planes and corresponding electron diffraction pattern (inset).

electron diffraction pattern of the grain seen in the image (and its surroundings), revealing the well-known narrow-spaced (00 l) rows of diffraction spots. The difference of the two diffraction patterns of Figs. 5.14(b) and 5.15(b) stems from a slightly different beam direction

(sample tilt), which in the case of Fig. 5.15 (b) resulted in a low-index crystal direction (diffraction pole) of the BNT grain.

Ferroelectric properties

Ferroelectric hysteresis loops were recorded in order to evaluate the ferroelectric properties of BLT and BNT films. Figures 5.16(a) and 5.16(b) show ferroelectric hysteresis loops recorded from (104)-oriented BLT and BNT films deposited on epitaxial (111)-oriented SrRuO₃ films on Pt(111)-covered YSZ(100)/Si(100) substrates, respectively. Both BLT and BNT thin films exhibit well-saturated polarization-electric field (P - E) curves revealing good ferroelectric switching characteristics. The measured remanent polarization ($2P_r$) and coercive field ($2E_c$) of the BLT films are $26.0 \mu\text{C}/\text{cm}^2$ and $163 \text{ kV}/\text{cm}$, respectively, for a maximum applied electric field of $300 \text{ kV}/\text{cm}$. For the BNT films, an about 1.5 times higher remanent polarization ($2P_r=38.7 \mu\text{C}/\text{cm}^2$) was obtained for the same maximum applied electric field and an about 1.3 times higher coercive field ($2E_c=212 \text{ kV}/\text{cm}$) was found. Compared to (104)-oriented BLT films grown by other deposition techniques and on other substrates, (104)-oriented BLT grown on SrRuO₃(111)/Pt(111)-covered Si(100) substrates by PLD show slightly lower remanent polarization values. Thus a BLT film grown on SrRuO₃(111) on SrTiO₃(111) by PLD showed a $2P_r$ value of $31.9 \mu\text{C}/\text{cm}^2$ [95] and a $2P_r$ value of $34 \mu\text{C}/\text{cm}^2$ was reported for a BLT film on SrRuO₃(111) on SrTiO₃(111) by MOCVD [97]. In the case of (104)-oriented BNT films, a similar remanent polarization value ($2P_r=40 \mu\text{C}/\text{cm}^2$) was reported, obtained from a BNT film on SrRuO₃(111) on SrTiO₃(111) made by PLD [96]. However, a BNT film grown on SrRuO₃(111) on SrTiO₃(111) by MOCVD showed higher $2P_r$ value of $50 \mu\text{C}/\text{cm}^2$ [97]. The overall values of remanent polarization in my samples are lower than the reported values for BLT and BNT films epitaxially grown on SrTiO₃ single crystal substrates. The cause of these lower remanent polarization values is under investigation and might be related to different crystallinities and to the presence of multiple twins in the films on buffered Si substrates.

Figures 5.16(c) and 5.16(d) show the recorded remanent polarization and the coercive field of BLT and BNT films as a function of the applied electric field. Although the polarization values of the BNT films are lower than those of the BLT films below an applied electric field of about $150 \text{ kV}/\text{cm}$, it can be concluded that the BNT films overall exhibit a higher polarization value than the BLT films above an applied field of about $150 \text{ kV}/\text{cm}$. It had been already reported that the higher polarization in the BNT films, compared with BLT films, is due to the structurally higher distortion of the TiO₆ octahedra in the perovskite block which originates from the smaller ionic radius of Nd³⁺ compared to La³⁺. A higher coercive field was observed in BNT films than in BLT films, as can be seen Fig. 5.11(d).

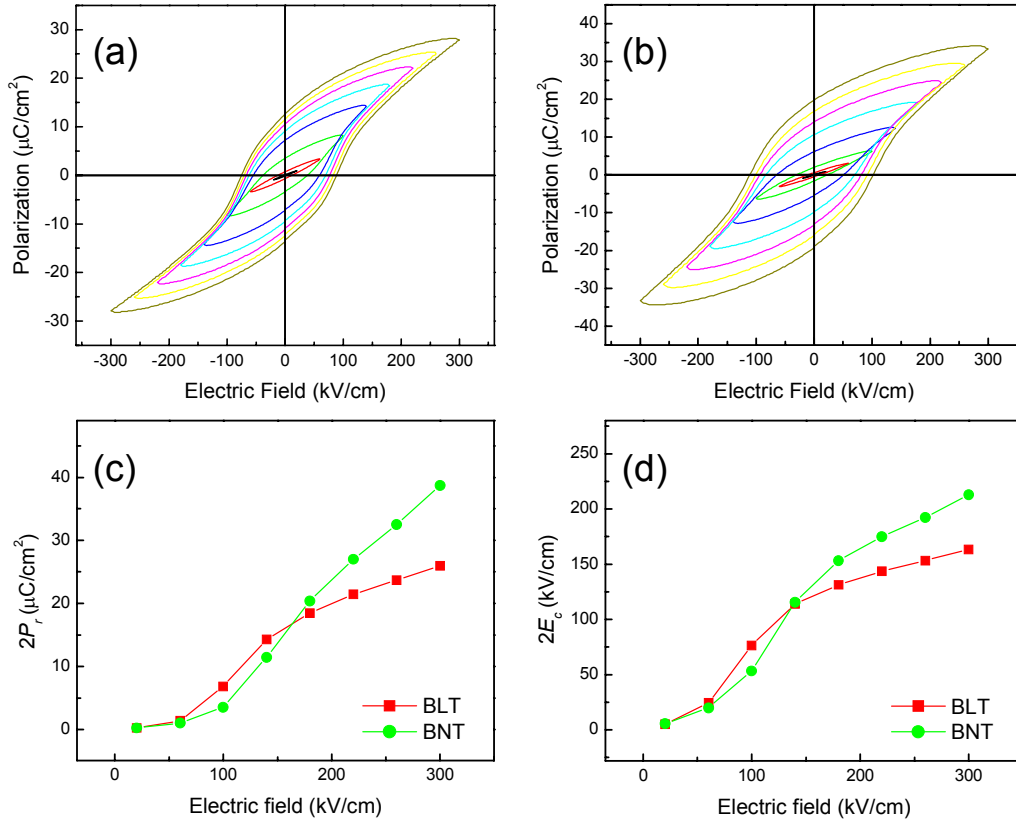


FIG. 5.16. P - E hysteresis loops of (a) Pt-BLT(104)-SrRuO₃(111) and (b) Pt-BNT(104)-SrRuO₃(111) capacitors on a Pt(111)/YSZ(100)/Si(100) heteroepitaxial substrate. The hysteresis loops were recorded at a frequency of 100 Hz. Different colors in P - E hysteresis loops stand for various applied electric fields. Comparison of (c) remanent polarization and (d) coercive field between BLT and BNT films.

Figure 5.17 shows the fatigue endurance characteristics of (a) a (104)-oriented BLT and (b) a (104)-oriented BNT film recorded at a frequency of 1 MHz using a fatiguing electric field of 180 kV/cm. The values of switching polarization are shown as a function of the number of switching cycles up to 1×10^{11} . Both BLT and BNT films show slight changes in the switching polarization. The insets in Figs. 5.17(a) and 5.17(b) show hysteresis loops recorded at an applied electric field of 180 kV/cm before and after the electrical fatigue test. Furthermore, in the cases of both BLT and BNT films, no significant change in the shape of the hysteresis loops was observed even after being subject to 1×10^{11} switching cycles at a frequency of 1 MHz. After the fatigue test a small reduction of the coercive field was found in the BLT film, whereas in the case of the BNT film the initial coercive field value was retained.

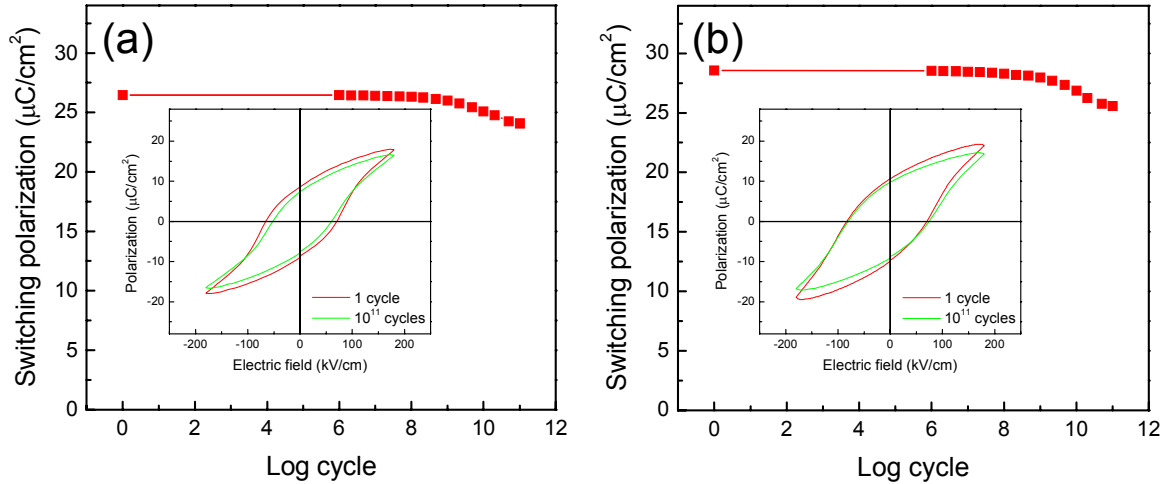


FIG. 5.17. Fatigue endurance of epitaxially twinned films of (a) (104)-oriented BLT and (b) (104)-oriented BNT recorded applying a bipolar electric field of 180 kV/cm at a frequency of 1 MHz. The insets show hysteresis loops before and after the fatigue test at 180 kV/cm.

5.3 Summary

Non-*c*-axis-oriented ferroelectric $\text{Bi}_{3.25}\text{La}_{0.75}\text{Ti}_3\text{O}_{12}$ and $\text{Bi}_{3.54}\text{Nd}_{0.46}\text{Ti}_3\text{O}_{12}$ epitaxial thin films with (104) orientation were grown by PLD on buffered Si(100) substrates. For the buffer layers, a heterostructure consisting of Pt(111)/YSZ(100)/Si(100) was applied to induce the growth of a (111)-oriented SrRuO_3 bottom electrode. Due to the fourfold symmetry of YSZ(100) and the threefold symmetry of the Pt(111) plane the SrRuO_3 electrodes were multiply twinned. Therefore the overlying ferroelectric films were also multiply twinned, inheriting this property from the electrodes. X-ray diffraction and transmission microscopy revealed the well-defined orientation relationships

$$\begin{aligned} & \text{BLT}(104); \text{BNT}(104) \parallel \text{SrRuO}_3(111) \parallel \text{Pt}(111) \parallel \text{YSZ}(100) \parallel \text{Si}(100); \\ & \text{BLT}[010]; \text{BNT}[010] \parallel \text{SrRuO}_3[0\bar{1}1] \parallel \text{Pt}[0\bar{1}1] \parallel \text{YSZ}\langle 001 \rangle \parallel \text{Si}\langle 001 \rangle. \end{aligned}$$

The BNT films showed an about 1.5 times higher remanent polarization ($2P_r=38.7 \mu\text{C}/\text{cm}^2$) than the BLT films ($2P_r=26.0 \mu\text{C}/\text{cm}^2$), revealing good ferroelectric properties. These (104)-oriented BLT and BNT films on Si(100) exhibited a good fatigue endurance and are suitable for applications in a number of silicon-based microelectronics.

Chapter 6

Reducing azimuthal domains in epitaxial ferroelectric La-substituted $\text{Bi}_4\text{Ti}_3\text{O}_{12}$ films using miscut yttria- stabilized zirconia single crystal substrates

In the previous chapters it has been demonstrated that non-*c*-axis-oriented La-substituted $\text{Bi}_4\text{Ti}_3\text{O}_{12}$ (BLT) thin films, having a rather large polarization component perpendicular to the film plane, can be grown on appropriately oriented SrTiO_3 substrates respectively on SrRuO_3 electrode layers on the latter, as well as on $\text{SrRuO}_3(111)$ -covered $\text{Pt}(111)/\text{YSZ}(100)/\text{Si}(100)$ substrates. In the latter case, the multiply twinned character of the Pt and SrRuO_3 layers resulted in twelve azimuthal domain variants in the BLT and Nd-substituted $\text{Bi}_4\text{Ti}_3\text{O}_{12}$ (BNT) films.

On the other hand it is well known that (110)-oriented SrRuO_3 films epitaxially grown on (100)-oriented YSZ have a specific in-plane domain structure consisting of four equivalent azimuthal orientations due to a diagonal-type rectangle-on-cube epitaxy of $\text{SrRuO}_3(110)$ on $\text{YSZ}(100)$ [66,69]. As a result, the angles between the lattices of four azimuthal domains are 20° , 70° , and 90° [cf. Fig. 6.4 below]. Therefore subsequently deposited bismuth-layered perovskite films on the SrRuO_3 electrodes also grow with the equivalent number of azimuthal domain variants resulting in 20° -, 70° -, and 90° -azimuthal domain boundaries [91]. As a result, the number of azimuthal domains in bismuth-layered perovskite films grown on $\text{SrRuO}_3(110)$ on $\text{YSZ}(100)$ is four times higher than on $\text{SrRuO}_3(110)$ on $\text{SrTiO}_3(110)$. Many of the corresponding domain boundaries in BLT films have a rather large thickness of the order of a few to about 15 nm and an amorphous crystallography as shown in Fig. 6.1. The electrical properties of the films may be influenced by the domain boundaries because the latter have many associated defects and are not fully

crystallized as had been shown by transmission electron microscopy (TEM) [91]. It is therefore desirable to find a way to reduce the number of azimuthal domains in BLT thin films. In view of YSZ(100) layers generally serving as buffer layers on Si(100) substrates, I concentrate on a method to reduce the number of azimuthal domains in BLT films grown on SrRuO_3 -covered YSZ(100) single crystals.

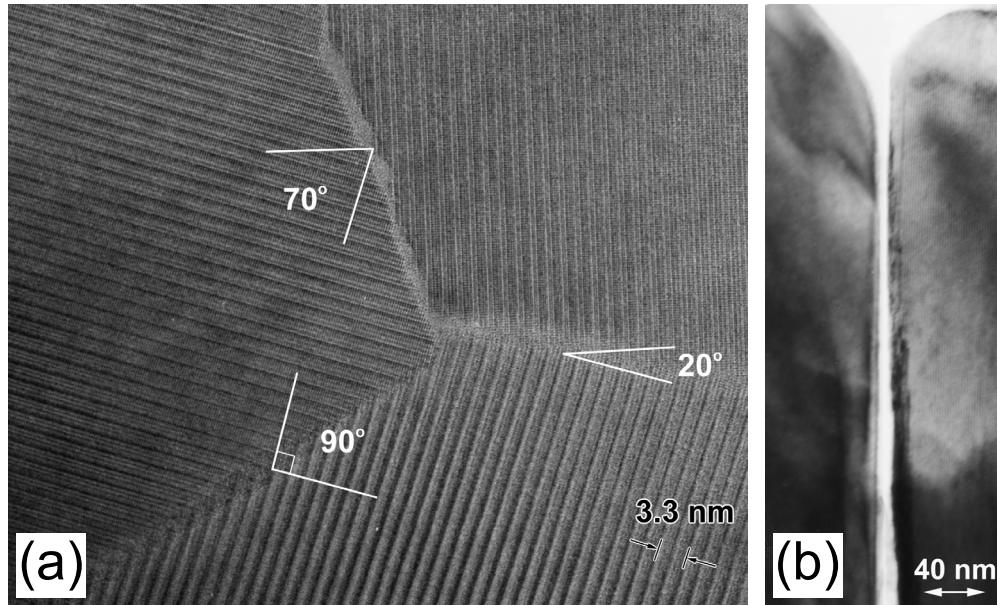


FIG. 6.1. (a) Plan-view TEM image of a section of a BLT(100) film containing three azimuthal domains, corresponding to domain boundaries of 20° , 70° and 90° types. The experimental value of approx. 20° corresponds to the theoretical value of 19.5° . (b) Cross-sectional TEM micrograph of a partially amorphous, thick azimuthal domain boundary.

In order to enhance the growth of single-domain, perovskite-type oxide thin films (including, e.g., SrRuO_3 , superconducting, and ferroelectric films), various miscut substrates such as SrTiO_3 [48,112,113,114,115], LaAlO_3 [116], and MgO [117,118] single crystals have been used. For instance, miscut $\text{SrTiO}_3(100)$ single crystal substrates have been used to achieve high-quality, single-domain epitaxial SrRuO_3 films using a 90° off-axis sputtering technique, selecting the miscut angle and direction [48,112]. In the case of high temperature superconducting films, epitaxial (103)-oriented, single-domain $\text{La}_{2-x}\text{Sr}_x\text{CuO}_4$ films have been obtained by 90° off-axis sputtering using miscut $\text{SrTiO}_3(101)$ substrates of appropriate miscuts [114]. In addition, recently Zheng *et al.* [118] have reported that the nucleation of antiphase domain boundaries is greatly reduced in $\text{Ba}_{0.5}\text{Sr}_{0.5}\text{TiO}_3$ thin films grown on miscut (001)-oriented MgO substrates, compared to the films on exactly cut substrates. It is generally believed that well-defined miscut substrates enable the growth of high quality oxide thin films, which can change the growth mechanism of thin films; for instance, the formation of selected predominant domains is induced by a step flow growth mechanism of

the film on the miscut substrate [119].

6.1 Experiment

Miscut (100)-oriented YSZ single crystal substrates with different miscut angles and miscut directions were commercially obtained and used to elucidate the influence of miscut substrates on the reduction of the number of azimuthal domain variants in SrRuO_3 and BLT films. As can be seen in Fig. 6.2, the angle between the surface normal and the crystallographic [100] direction of the YSZ(100) substrate is the miscut angle α . The miscut direction, β , is defined as the angle between the projection of the surface normal onto the (100) plane and the in-plane [001] direction. {Here, $\beta=0^\circ$ is defined as the YSZ[001] direction and $\beta=45^\circ$ is defined as the YSZ[011] direction in the YSZ(100) plane}. Before SrRuO_3 film deposition, the miscut YSZ single crystal substrates are thermally treated to improve their quality and finally to enhance the effect of the reduction of the number of azimuthal domain variants. Miscut YSZ substrates were annealed at 1200°C for 10 min in air. The deposition of the SrRuO_3 electrode layers and the BLT thin films was carried out *in situ* by pulsed laser deposition (PLD). The SrRuO_3 films were grown from a stoichiometric target at a substrate temperature of 775°C in 0.14 mbar oxygen ambient using a laser energy density of 1.7 J/cm^2 . The epitaxial BLT films were grown at 750°C in 0.4 mbar of oxygen pressure with a laser energy density of 2.3 J/cm^2 .

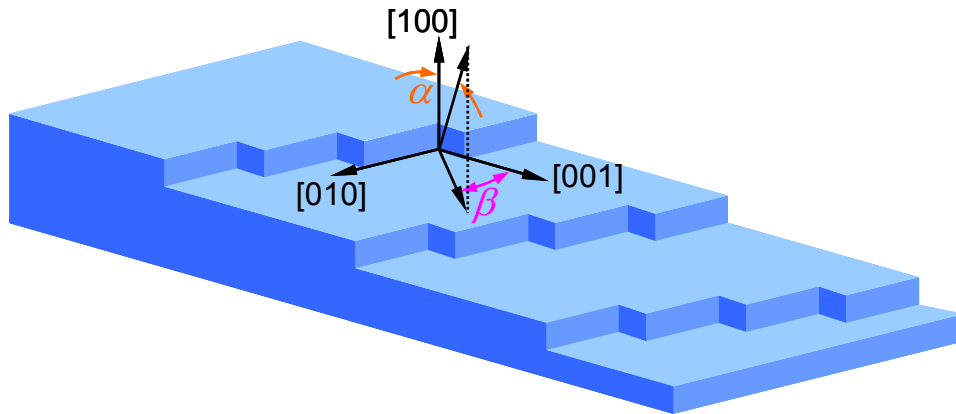


FIG. 6.2. Schematic drawing of a miscut YSZ(100) single crystal substrate surface. The miscut angle and miscut direction are denoted “ α ” and “ β ”, respectively.

6.2 Results and discussion

6.2.1 SrRuO_3 films on miscut YSZ(100) single crystal substrates

Commercially available (100)-oriented YSZ single crystals with different miscut angles (α) and directions (β) were used as substrates, namely (i) $\alpha=1.5^\circ$ and $\beta=0^\circ$, (ii) $\alpha=5^\circ$ and $\beta=0^\circ$, (iii) $\alpha=1.5^\circ$ and $\beta=45^\circ$, and (iv) $\alpha=5^\circ$ and $\beta=45^\circ$. It should be noted that $\beta=0^\circ$ and 45° correspond to the YSZ[001] and the YSZ[011] direction, respectively. Figure 6.3 shows the results of XRD ϕ scans of SrRuO_3 films deposited on as-purchased miscut YSZ(100) substrates. The fixed 2θ angle used to record the ϕ scans was 46.18° corresponding to the SrRuO_3 200 reflection. For all SrRuO_3 films on four different types of YSZ substrates, eight peaks arranged with a four-fold symmetry are seen.

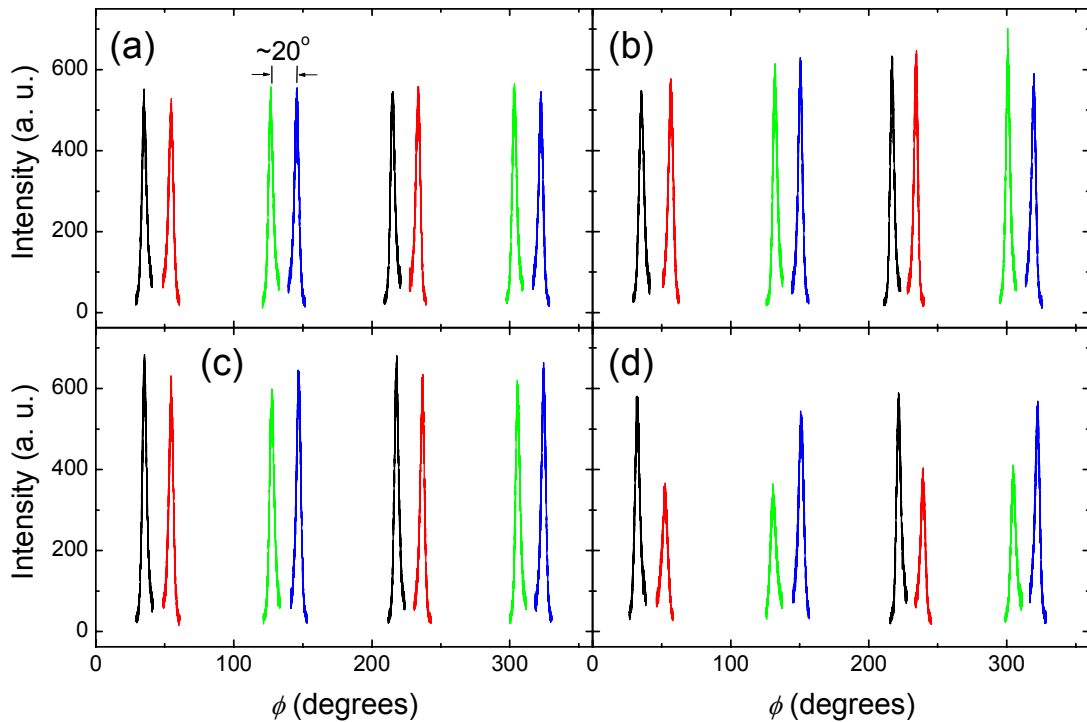


FIG. 6.3. X-ray diffraction ϕ scans of $\text{SrRuO}_3(110)$ films on as-purchased miscut YSZ(100) single crystal substrates with (a) $\alpha=1.5^\circ$ and $\beta=0^\circ$, (b) $\alpha=5^\circ$ and $\beta=0^\circ$, (c) $\alpha=1.5^\circ$ and $\beta=45^\circ$, and (d) $\alpha=5^\circ$ and $\beta=45^\circ$. The fixed 2θ angles were 46.18° corresponding to the SrRuO_3 200 reflection. The four colors mark the four different azimuthal domains seen in Fig. 6.4.

These peaks are grouped into four sets of two reflection peaks each, with a ϕ angle difference $\Delta\phi$ of $\sim 20^\circ$. This arrangement of the peaks originates from the diagonal-type rectangle-on-cube epitaxy relation of $\text{SrRuO}_3(110)$ on YSZ(100) as schematically shown in Fig. 6.4. As the figure shows, the (110) orientation of SrRuO_3 on (100)-oriented YSZ implies

a minimization of the $\text{SrRuO}_3/\text{YSZ}$ lattice misfit by each one of four specific azimuthal orientations of the SrRuO_3 lattice. (The lattice mismatch along the diagonal direction of $\text{SrRuO}_3[\bar{1}11]||\text{YSZ}\langle 011\rangle$ is -6.3% , which is to be compared to the mismatch of 8.2% along $\text{SrRuO}_3\langle 110\rangle||\text{YSZ}\langle 100\rangle$ or that of -23.5% along the $\text{SrRuO}_3\langle 100\rangle||\text{YSZ}\langle 100\rangle$ directions.) Since there are four positionings to arrange the respective diagonals, there are four possible azimuthal domain variants in a $\text{SrRuO}_3(110)$ film on a $\text{YSZ}(100)$ substrate taking into account that the $\text{SrRuO}_3[\bar{1}11]$ direction may be parallel to any of the four $[011]$, $[0\bar{1}\bar{1}]$, $[01\bar{1}]$ and $[0\bar{1}1]$ directions of $\text{YSZ}(100)$.

Pairwise comparing peaks with the ϕ angle difference of $\sim 20^\circ$ [Figs. 6.3(a)–6.3(c)], it is found that there are no significant differences in reflection intensities. This indicates that the four azimuthal SrRuO_3 domain variants are of approximately equal volume fraction. On the other hand, SrRuO_3 films grown on miscut $\text{YSZ}(100)$ substrates with $\alpha=5^\circ$ and $\beta=45^\circ$ in Fig. 6.3(d) revealed an asymmetric intensity between two neighboring peaks, indicating that the volume fraction of two azimuthal domain variants is larger than that of the other two domain variants. The $\text{SrRuO}_3[\bar{1}11]$ direction of the two domain variants with the larger volume fraction is parallel to the $[011]$ or $[0\bar{1}\bar{1}]$ direction of YSZ , which is identical to the substrate miscut direction.

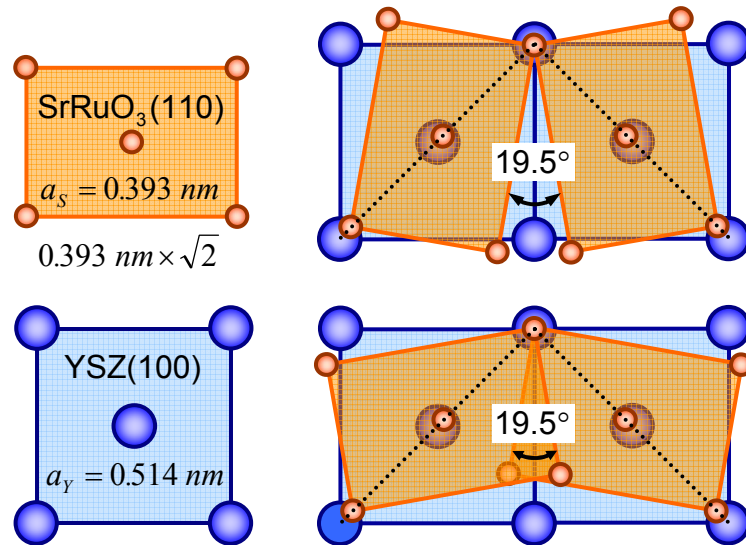


FIG. 6.4. Schematic drawing of the diagonal-type “rectangle-on-cube” epitaxy relation of $\text{SrRuO}_3(110)$ on $\text{YSZ}(100)$. Four possible azimuthal domain variants in a $\text{SrRuO}_3(110)$ film on a $\text{YSZ}(100)$ substrate.

In order to enhance the effect of the reduction of the number of azimuthal domain variants in SrRuO_3 thin films, the miscut $\text{YSZ}(100)$ single crystal substrates were annealed at 1200°C for 10 min in air, before depositing the SrRuO_3 film. Figure 6.5 shows AFM topographic images taken from four different miscut $\text{YSZ}(100)$ substrates after annealing. In

the case of the 1.5° miscut YSZ substrates shown in Figs. 6.5(a) and 6.5(c), it is rather difficult to observe a specific pattern of the substrate surface whereas step-like surface morphologies of YSZ substrates with 5° miscut angle along corresponding miscut directions are clearly seen in Figs. 6.5(b) and 6.5(d). It is generally known that chemically or thermally treated substrates with high miscut angle show a high step height and a narrow step width. This might be the reason why a well-developed step pattern is visible in Figs. 6.5(b) and 6.5(d), but not in Figs. 6.5(a) and 6.5(c).

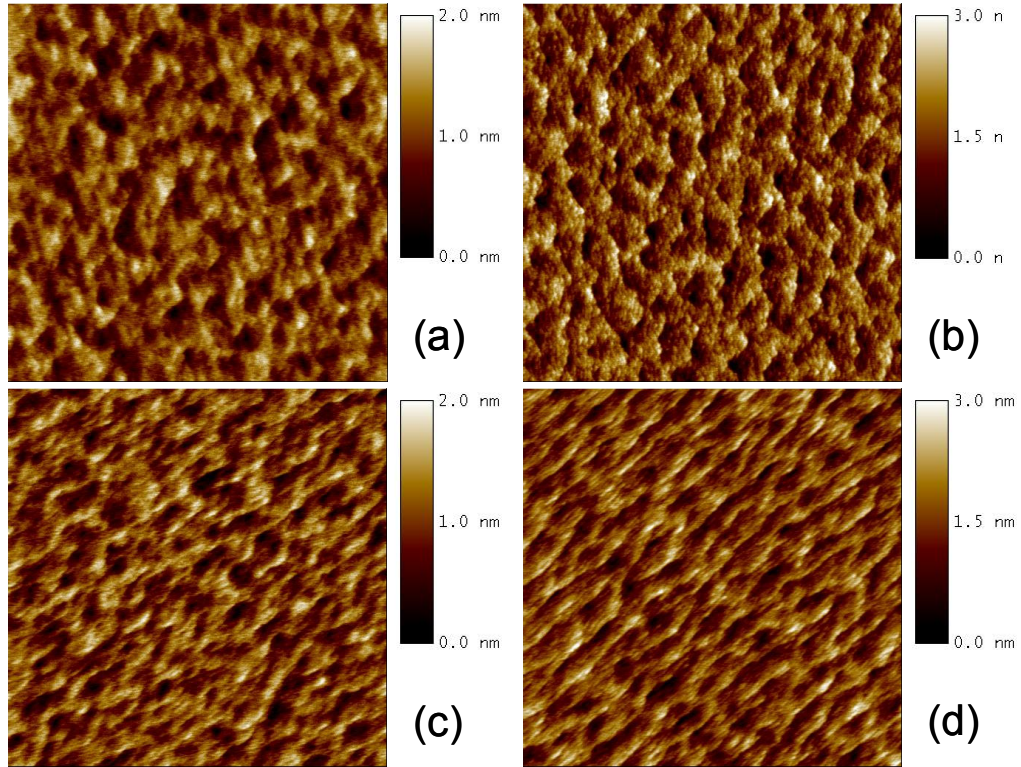


FIG. 6.5. AFM topography images (image size: $2 \times 2 \mu\text{m}^2$) of thermally treated miscut YSZ(100) single crystal substrates with (a) $\alpha=1.5^\circ$ and $\beta=0^\circ$, (b) $\alpha=5^\circ$ and $\beta=0^\circ$, (c) $\alpha=1.5^\circ$ and $\beta=45^\circ$, and (d) $\alpha=5^\circ$ and $\beta=45^\circ$.

Figure 6.6 shows ϕ scans of SrRuO_3 films deposited on the thermally treated miscut YSZ(100) substrates. These figures were recorded using the SrRuO_3 200 reflection ($2\theta=46.18^\circ$), and they are quite different from the ϕ scans of SrRuO_3 films in Fig. 6.3. In the case of SrRuO_3 films on the annealed YSZ(100) substrates with low miscut angle in Fig. 6.5(a), the reduction of azimuthal domain variants was not effective. However, as is evident from the ϕ scans [Figs 6.6(b)–6.6(d)], an enhancement of the reduction effect was possible by annealing the miscut YSZ substrates. In the case of SrRuO_3 films on miscut YSZ(100) substrates with $\beta=45^\circ$ [Figs. 6.6(c) and 6.6(d)], a strongly asymmetric intensity between two neighboring reflection peaks is observed, whereas the two peaks with angle differences $\Delta\phi$ of $\sim 70^\circ$ and $\sim 110^\circ$ are symmetric revealing that the volume fraction of two azimuthal domain

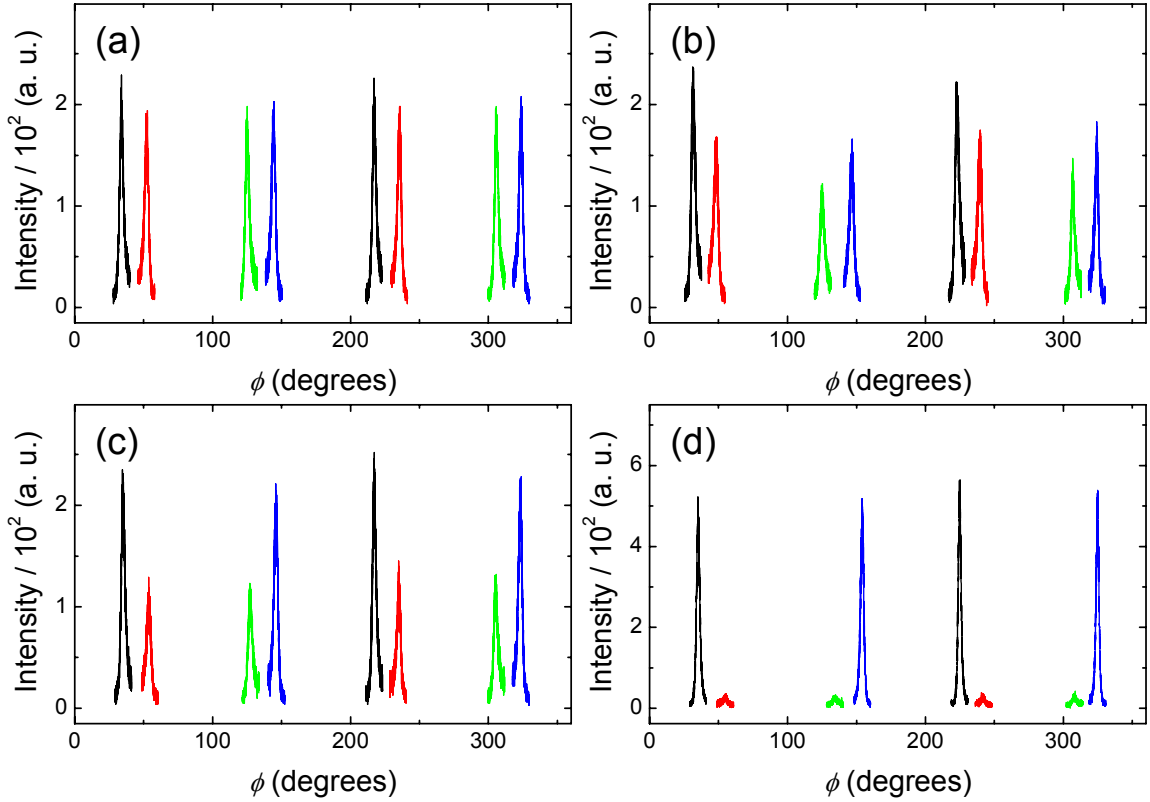


FIG. 6.6. X-ray diffraction ϕ scans of $\text{SrRuO}_3(110)$ films on thermally treated miscut $\text{YSZ}(100)$ single crystal substrates with (a) $\alpha=1.5^\circ$ and $\beta=0^\circ$, (b) $\alpha=5^\circ$ and $\beta=0^\circ$, (c) $\alpha=1.5^\circ$ and $\beta=45^\circ$, and (d) $\alpha=5^\circ$ and $\beta=45^\circ$. The fixed 2θ angles were 46.18° corresponding to the SrRuO_3 200 reflection.

variants (out of four) is uniformly reduced. However as shown in Fig. 6.6(b), the distribution of the azimuthal domain variants in SrRuO_3 films grown on $\text{YSZ}(100)$ substrates with $\alpha=5^\circ$ and $\beta=0^\circ$ is not homogeneous. In summary, SrRuO_3 films grown on miscut $\text{YSZ}(100)$ with $\alpha=5^\circ$ and $\beta=45^\circ$ showed an almost entire elimination of two (out of four) azimuthal domain variants, as shown in Fig.6.6(d). The $\text{YSZ}[011]$ miscut direction ($\beta=45^\circ$) thus effectively reduces the number of the azimuthal domain variants in SrRuO_3 thin films by about 50%. A careful inspection of Fig. 6.6 reveals small deviations (of the order of 1° to 2°) from $\Delta\phi=19.5^\circ$ between two neighboring peaks. This finding will be discussed below in relation to the detailed characterization of the pole figures of SrRuO_3 films in Fig. 6.7. The volume fraction distribution of the four possible azimuthal domain variants (“A” to “D”) in SrRuO_3 films with respect to the investigated four different miscut $\text{YSZ}(100)$ substrates are summarized in Table 6.1, together with the comparison between non-annealed and annealed substrates. These volume fractions have been evaluated by comparing the intensities of each peak in the ϕ scan [Figs. 6.3 and 6.6], using the following equation

$$\frac{I_k}{I_A + I_B + I_C + I_D} \cdot 100 \quad (k=A, B, C, \text{ and } D). \quad (6.1)$$

Note that each peak of the ϕ scan in Figs. 6.3 and 6.6 is repeated after 180° due to the mirror symmetry of any diffraction pattern, so that each type of azimuthal domain gives rise to *two* peaks in a ϕ scan. Accordingly the intensity I_k of each azimuthal domain is the summation of the two peak intensities with about $\Delta\phi=180^\circ$.

Table 6.1. Volume fraction (in percent) of the four different azimuthal domain variants “A” to “D” in $\text{SrRuO}_3(110)$ films on $\text{YSZ}(100)$ substrates with miscut α and β .

	On as-purchased $\text{YSZ}(100)$				On thermally treated $\text{YSZ}(100)$			
	$\alpha=1.5^\circ$ $\beta=0^\circ$	$\alpha=5^\circ$ $\beta=0^\circ$	$\alpha=1.5^\circ$ $\beta=45^\circ$	$\alpha=5^\circ$ $\beta=45^\circ$	$\alpha=1.5^\circ$ $\beta=0^\circ$	$\alpha=5^\circ$ $\beta=0^\circ$	$\alpha=1.5^\circ$ $\beta=45^\circ$	$\alpha=5^\circ$ $\beta=45^\circ$
“A”	25.4	24.7	22.1	21.5	23.9	18.9	17.5	3.0
“B”	25.0	25.3	25.9	27.0	24.8	24.6	30.6	46.3
“C”	25.0	24.8	27.0	31.0	27.6	32.3	33.2	47.5
“D”	24.6	25.2	25.0	20.5	23.7	24.2	18.7	3.2

In addition to the azimuthal growth-domain reduction, another interesting feature is observed in pole figures of the SrRuO_3 films. Figure 6.7 shows pole figures of SrRuO_3 films deposited on different miscut $\text{YSZ}(100)$ substrates using the SrRuO_3 200 reflection corresponding to $2\theta=46.18^\circ$. (The center and the rim of the pole figures correspond to $\psi=0^\circ$ and 90° , respectively; $\psi=90^\circ$ corresponds to the substrate surface being parallel to the plane defined by the incident and reflected x-ray beams.) As can be seen in Fig. 6.7, a small, systematic tilt of the crystallographic orientation of the films was observed. In general, the reflection peaks from (110)-oriented SrRuO_3 grown on exactly (100)-oriented YSZ in pole figures are centrosymmetrically positioned at $\psi=45^\circ$, i.e., $\text{SrRuO}_3(110)\parallel\text{YSZ}(100)$; $\text{SrRuO}_3[110]\parallel\text{YSZ}[100]$. However the pole figures of SrRuO_3 films on the miscut YSZ substrates do not exhibit centrosymmetrical reflection peaks. It is found that all reflection peaks were shifted by the corresponding miscut angle towards the corresponding miscut direction. This is a consequence of the fact that both the upper and lower crystal surfaces were processed (cut and polished) by the commercial manufacturer with the same miscut [see Fig. 6.7(e) and 6.7(f)]. Since $\text{SrRuO}_3(110)\parallel\text{YSZ}(100)$ exactly, a similar scheme like Fig. 6.7(f) holds for the SrRuO_3 film on top of the miscut YSZ substrate, giving rise to the asymmetry of the pole figures. (This tilt was also observed in SrRuO_3 films on the non-

annealed miscut YSZ substrates in Fig. 6.3.) To guide the eye, dashed line circles and arrows are drawn into the pole figures, the latter indicating the order and the direction of the shift of the peaks. Due to this fact, the angle difference between neighboring peaks in SrRuO_3 films on miscut YSZ(100) substrates is not exactly 19.5° , but a slight deviation from this angle difference occurs, as already mentioned above. According to the tilt of the film orientation, the angle difference of ideally 19.5° is increased on the side of shift direction and is decreased on the opposite side. This is also the reason why different angle differences were recorded in XRD ϕ scans of Figs. 6.3 and 6.6. Therefore in this chapter all XRD ϕ scans of SrRuO_3 and BLT films were performed through finding the maximal intensities of all peaks

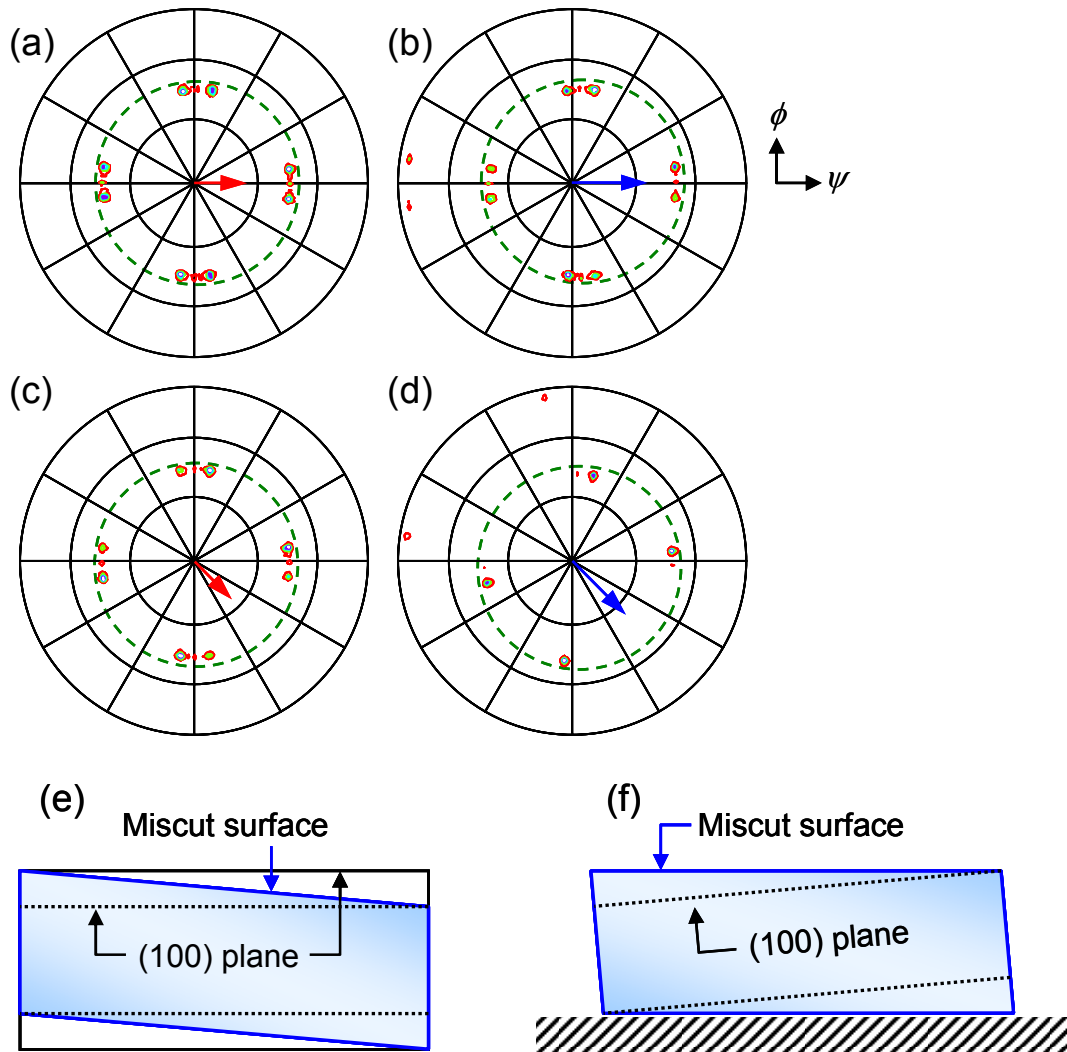


FIG. 6.7. X-ray diffraction pole figures of $\text{SrRuO}_3(110)$ films on thermally treated miscut YSZ(100) single crystal substrates with (a) $\alpha=1.5^\circ$ and $\beta=0^\circ$, (b) $\alpha=5^\circ$ and $\beta=0^\circ$, (c) $\alpha=1.5^\circ$ and $\beta=45^\circ$, and (d) $\alpha=5^\circ$ and $\beta=45^\circ$. The fixed 2θ angle was 46.18° corresponding to the SrRuO_3 200 reflection. The arrows indicate that the SrRuO_3 (110) lattice plane is parallel to the YSZ (100) lattice plane, which is tilted with respect to the top and bottom surfaces of the substrate. [(e) and (f)] Schematic drawing of a miscut YSZ single crystal substrate. Both the upper and lower crystal surfaces were processed (cut and polished) by the commercial manufacturer with the same miscut.

after several optimization scans in ϕ and ψ . In addition, on the assumption that the SrRuO_3 (110) plane is parallel to the YSZ(100) plane, the positions of the maxima of all peaks could be predicted by calculation.

Figure 6.8 represents schematic drawings of four possible azimuthal domain variants and the corresponding pole figure of a (110)-oriented SrRuO_3 film grown on a YSZ(100) substrate. As shown in this figure, possible angle differences between the four domain variants of SrRuO_3 are 20° , 70° , and 90° . These angles are shown in the corresponding schematic pole figure, which is in good agreement with the experimental pole figures in Fig. 6.7. Comparing the experimental pole figures [Fig. 6.7(c) and 6.7(d)] to the schematic pole figure, a pair of two predominant domain variants in SrRuO_3 films on YSZ(100) substrates with [011] miscut direction is either the pair of domain variants “B” and “C”, or the pair of “A” and “D”. Due to the step flow growth mechanism of the thin film on the miscut substrate [119], the formation of preferential domains *along the miscut direction* is induced. Thus it can be concluded that the two predominant domain variants are the domain variants marked “B” and “C” whose $\text{SrRuO}_3[\bar{1}11]$ directions are identical with the corresponding substrate miscut direction of YSZ[011]. It should be noted that a consideration of the exact misfit values of the domain variants “A” to “D” results in an increased misfit for domains “A” and “D” as compared to domains “B” and “C” [120]. This is an additional argument in favor of domain variants “B” and “C” becoming the predominant ones.

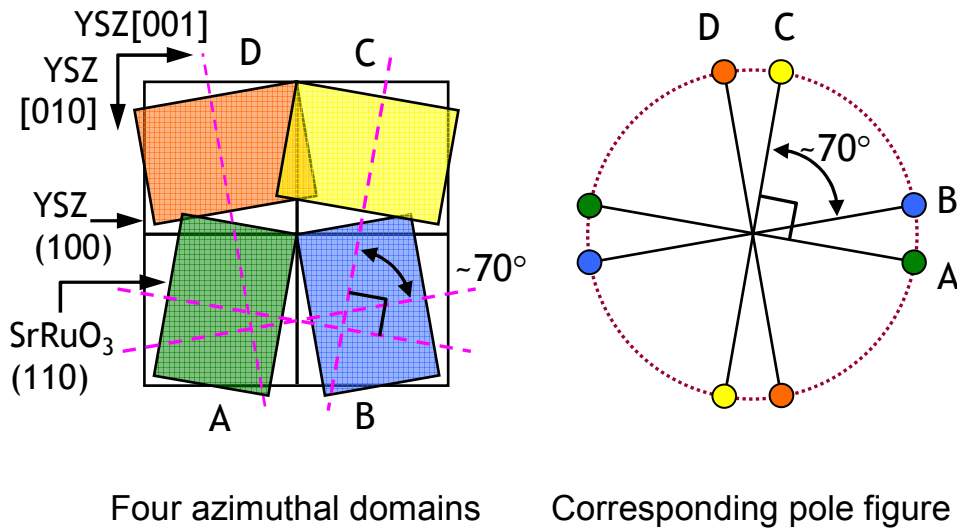


FIG. 6.8. Azimuthal domain variants and corresponding schematic pole figure of (110)-oriented SrRuO_3 on (100)-oriented YSZ.

Transmission electron microscope (TEM) investigations were performed to confirm the crystallographic orientation and the effect of the reduction of the azimuthal domain variants. Figure 6.9(a) shows a cross-sectional TEM image of a 65 nm thick $\text{SrRuO}_3(110)$ film on an annealed miscut YSZ(100) substrate. The electron diffraction pattern [inset of Fig. 6.9(a), and

the identical but magnified lower left image of Fig. 6.9(b), with spot indexation] confirms the exact orientation of the SrRuO_3 lattice with respect to the YSZ lattice. (This finding supports the argument above, used when discussing the origin of the asymmetry of the SrRuO_3 pole figures.) Figure 6.9(c) is a plan-view electron diffraction pattern that shows a clear asymmetry of the inner reflections corresponding to the (012) and (102) orthorhombic SrRuO_3 planes. This asymmetry is equivalent to the asymmetry of the XRD ϕ scan of Fig. 6.6(d). Both in Fig. 6.6(d) and here, the angle of about 70° between the azimuthal domain variants “B” and “C” is clearly visible [cf. Fig. 6.8].

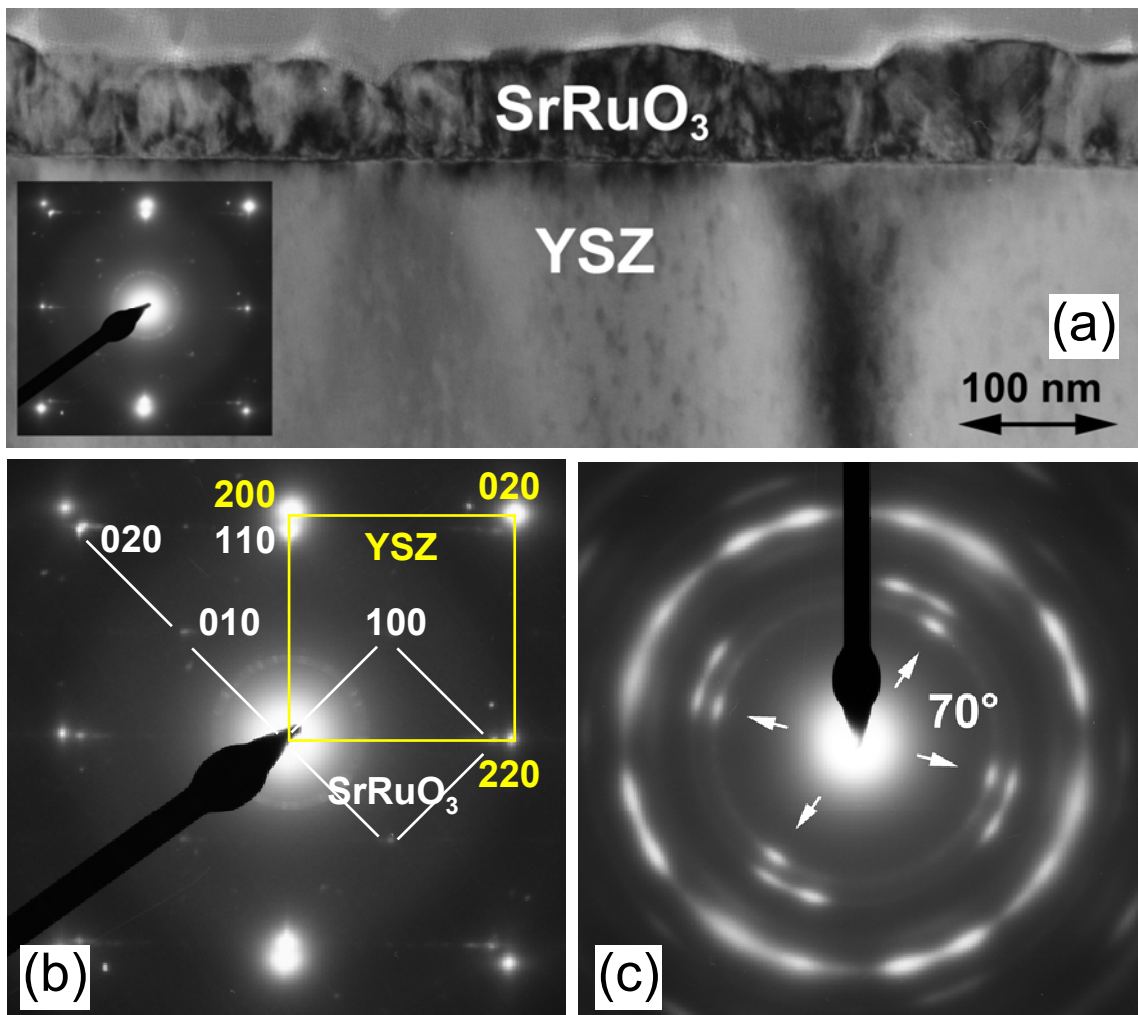


FIG. 6.9. (a) Cross-sectional transmission electron micrographs with electron diffraction pattern in the inset, (b) magnified electron diffraction pattern of the inset in (a), and (c) plan-view electron diffraction pattern of a (110)-oriented SrRuO_3 film on a thermally treated miscut YSZ(100) single crystal substrate with $\alpha=5^\circ$ and $\beta=45^\circ$.

6.2.2 La-substituted $\text{Bi}_4\text{Ti}_3\text{O}_{12}$ films on SrRuO_3 -covered miscut YSZ(100) substrates

X-ray diffraction θ - 2θ scan, ϕ scan, and pole figures

In order to investigate whether the miscut substrate also affects the domain variants of subsequently grown films, ferroelectric BLT films were deposited on $\text{SrRuO}_3(110)$ electrodes on miscut YSZ(100) single crystal substrates. To simultaneously study the influence of the miscut onto (100)- and (118)-oriented BLT films, I used growth conditions that result in the growth of a mix of (100) and (118) orientations. Figure 6.10 is a XRD θ - 2θ scan of a BLT film grown on $\text{SrRuO}_3(110)$ on a miscut YSZ(100) substrate with $\alpha=5^\circ$ and $\beta=45^\circ$. Only the peaks from the YSZ(100) substrate, the $\text{SrRuO}_3(110)$ film, and the BLT film with the mix of (100) and (118) orientations (showing BLT 200/020, 400/040, and $22\bar{1}6$ peaks) are observed.

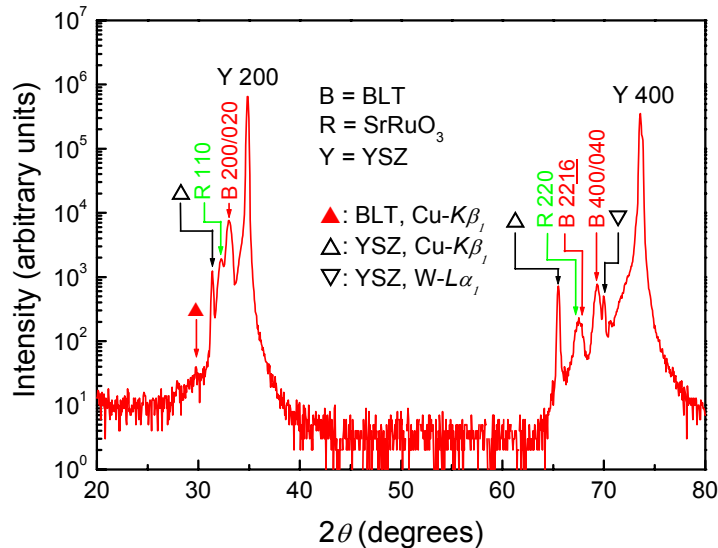


FIG. 6.10. X-ray diffraction θ - 2θ scan of a BLT film on a $\text{SrRuO}_3(110)$ -covered thermally treated miscut YSZ(100) single crystal substrate with $\alpha=5^\circ$ and $\beta=45^\circ$. The θ - 2θ scan was performed at $\psi=5^\circ$ due to the tilt of the surface of the YSZ(100) substrate. The $\text{Cu-K}\beta_1$ lines are due to the remaining $\text{Cu-K}\beta_1$ radiation, and the $\text{W-L}\alpha_1$ lines are due to the tungsten contamination of the x-ray target by the tungsten cathode filament.

Figure 6.11 shows pole figures of BLT films on $\text{SrRuO}_3(110)$ -covered miscut YSZ(100) substrates with (a) $\alpha=1.5^\circ$ and $\beta=0^\circ$, (b) $\alpha=5^\circ$ and $\beta=0^\circ$, (c) $\alpha=1.5^\circ$ and $\beta=45^\circ$, and (d) $\alpha=5^\circ$ and $\beta=45^\circ$. These pole figures were recorded using the BLT 117 reflection corresponding to $2\theta=30.1^\circ$. One set is composed of peaks located at $\psi\approx 4^\circ$, 64° , and 82° (within a ψ angle deviation of about 5° resulting from the miscut) corresponding to the BLT 117, $\bar{1}17/1\bar{1}7$, and $11\bar{7}$ peaks, respectively, from the (118)-oriented part of the film. Another set appears at $\psi\approx 57^\circ$ (again within a ψ angle deviation of about 5°) consisting of the

$11\bar{7}$, $1\bar{1}7$, $1\bar{1}\bar{7}$, and $11\bar{7}$ peaks from the (100)-oriented part of the film. As can be seen in these pole figures, a similar feature of the shift of the reflection peaks as for the SrRuO_3 films on miscut YSZ(100) substrates is also observed in all pole figures of Fig. 6.11. All reflection peaks are shifted by the corresponding miscut angles towards the corresponding miscut direction revealing the tilt of the crystallographic orientation of the BLT films due to the corresponding miscut YSZ(100) substrates. Moreover it is found that the reduction of the number of azimuthal domain variants also occurs in the BLT films that are grown on SrRuO_3 films having a reduced number of azimuthal domain variants. Since this effect is not easy to see in the pole figures of Fig. 6.11, it will be demonstrated by help of ϕ scans.

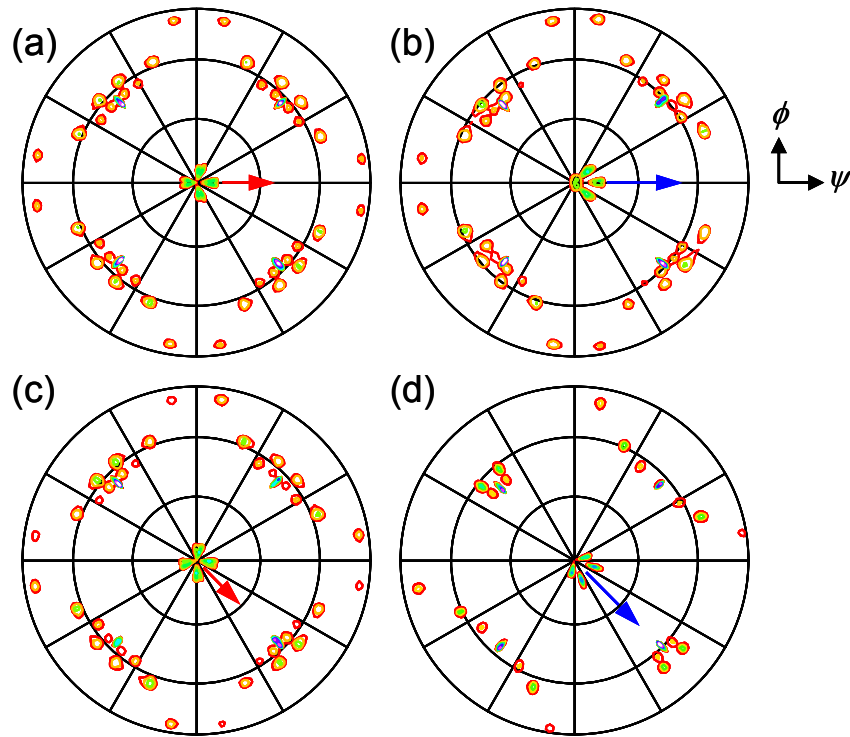


FIG. 6.11. X-ray diffraction pole figures of BLT films on $\text{SrRuO}_3(110)$ -covered YSZ(100) single crystal substrates (with thermal treatment) with (a) $\alpha=1.5^\circ$ and $\beta=0^\circ$, (b) $\alpha=5^\circ$ and $\beta=0^\circ$, (c) $\alpha=1.5^\circ$ and $\beta=45^\circ$, and (d) $\alpha=5^\circ$ and $\beta=45^\circ$. The fixed 2θ angles were 30.1° corresponding to the BLT 117 reflection. The pole figures show a mix of (118) and (100) orientation of the BLT thin films. All reflection peaks are shifted by the corresponding miscut angles towards the corresponding miscut direction.

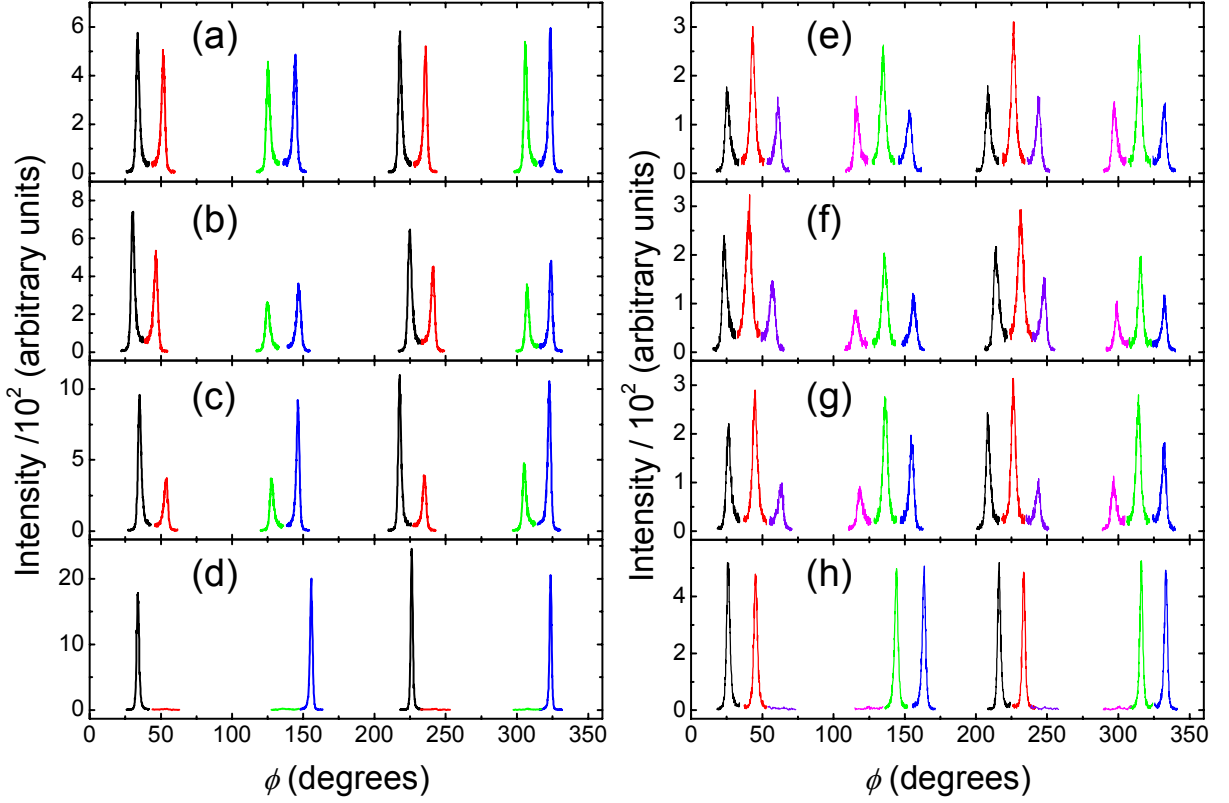


FIG. 6.12. X-ray diffraction ϕ scans of BLT films on $\text{SrRuO}_3(110)$ -covered $\text{YSZ}(100)$ single crystal substrates with [(a) and (e)] $\alpha=1.5^\circ$ and $\beta=0^\circ$, [(b) and (f)] $\alpha=5^\circ$ and $\beta=0^\circ$, [(c) and (g)] $\alpha=1.5^\circ$ and $\beta=45^\circ$, and [(d) and (h)] $\alpha=5^\circ$ and $\beta=45^\circ$. The fixed 2θ angles were 23.31° corresponding to BLT 111 reflection. The ϕ scans were recorded at $\psi \sim 36^\circ$ (within the ψ angle deviation of about 5° resulting from the miscut) [(a) to (d)] and at $\psi \sim 46^\circ$ (again within the ψ angle deviation of about 5°), respectively [(e) to (h)], in correspondence to the (118)- and (100)-oriented parts of the BLT films.

In order to compare the effect of the reduction of domain variants between BLT films on four different miscut $\text{YSZ}(100)$ substrates in detail, various XRD ϕ scans were performed through finding the maximal intensities of all peaks after several optimization scans in ϕ and ψ . Figure 6.12 shows ϕ scans of BLT films using the BLT 111 reflection corresponding to $2\theta=23.31^\circ$ in the ψ angle range between $\sim 31^\circ$ and $\sim 41^\circ$ [Figs. 6.11(a)–6.11(d)] for the (118)-oriented part of the film, and between $\psi \sim 41^\circ$ and $\sim 51^\circ$ [Figs. 6.11(e)–6.11(h)] for the (100)-oriented part, respectively. [Note the angles $\angle(118) : (111) = 36.4^\circ$ and $\angle(100) : (111) = 45.6^\circ$ for a BLT film on an exactly cut YSZ substrate.] For the reason mentioned before, ψ angular deviations of the BLT 111 reflection are also attributed to the crystallographic tilting analogous to the situation in the SrRuO_3 films. For the (118)-oriented part of the BLT film, as shown in Figs. 6.12(a)–6.12(c), ϕ angle differences of $\sim 20^\circ$ between two neighboring peaks are present in the BLT films resulting from corresponding azimuthal domain variants in SrRuO_3 films, whereas the BLT film in Fig. 6.12(d) exhibits only two predominant azimuthal domain variants which are identical to those in a SrRuO_3 film grown on miscut $\text{YSZ}(100)$ with $\alpha=5^\circ$ and $\beta=45^\circ$. Similarly, four sets of reflection peaks in the ϕ scans were also

observed in Figs. 6.12(e)–6.12(h). For the (100)-oriented part of the BLT films each set of peaks shown in Fig. 6.11(e)–6.11(g) is composed of two subsets (overlapping into three peaks), with an offset between the two neighboring subsets of $\Delta\phi \sim 20^\circ$, whereas in Fig. 6.12(h) each set consists of only one subset. Overall Fig. 6.12 indicates that the effect of a miscut substrate on the reduction of the number of azimuthal domain variants has taken place not only in the SrRuO_3 electrodes [Figs. 6.6(a)–6.6(d)], but also in the subsequently grown BLT films.

Atomic force microscopy and transmission electron microscopy

AFM characterizations clearly confirmed the reduction of the number of the azimuthal domain variants in ferroelectric BLT thin films. Figure 6.13 shows AFM topographic images of BLT films on SrRuO_3 films on miscut YSZ(100) substrates revealing very different grain orientations.

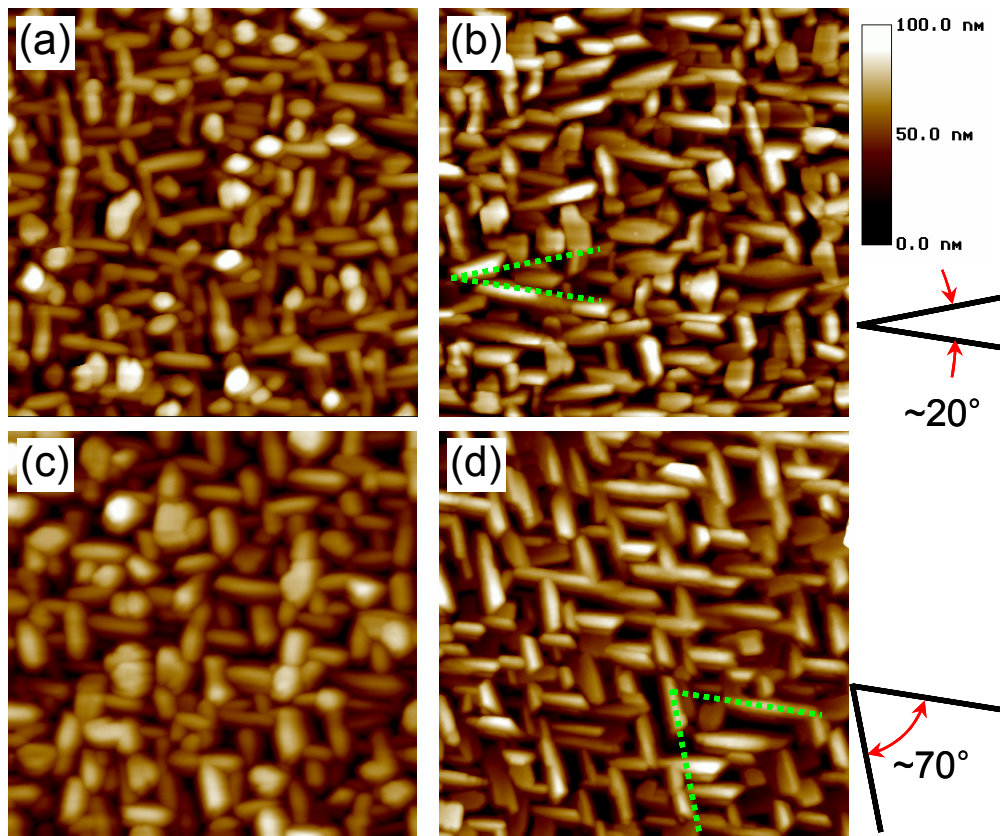


FIG. 6.13. AFM topography images (image size: $2 \times 2 \mu\text{m}^2$) of BLT films on $\text{SrRuO}_3(110)$ -covered YSZ(100) single crystal substrates with (a) $\alpha=1.5^\circ$ and $\beta=0^\circ$, (b) $\alpha=5^\circ$ and $\beta=0^\circ$, (c) $\alpha=1.5^\circ$ and $\beta=45^\circ$, and (d) $\alpha=5^\circ$ and $\beta=45^\circ$. Particularly, in (d), most grains are aligned along only two directions with an azimuthal angle difference of $\sim 70^\circ$.

In the case of BLT films grown on YSZ(100) substrates with YSZ[001] miscut direction in Figs. 6.13(a) and 6.13(b), most of the grains having azimuthal angle differences of 20° , 70° , and 90° are homogeneously oriented along four directions in the BLT film of Fig. 6.13(a), whereas the BLT film in Fig. 6.13(b) shows the grains arranged along two directions with an angle difference of $\sim 20^\circ$. For this sample, the ϕ scan intensities of two neighboring peaks with $\Delta\phi \sim 20^\circ$ are higher than those of the other two neighboring peaks, separated by 90° from the former [Figs. 6.12(b) and 6.12(f)] which is in good agreement with the AFM image of Fig. 6.12(b). Moreover, in the case of BLT films grown on YSZ(100) substrates with YSZ[011] miscut direction in Figs. 6.13(c) and 6.13(d), most grains are arranged along only two directions with an azimuthal angle difference of $\sim 70^\circ$. In particular, Fig. 6.13(d) shows almost completely the alignment of the grains along two azimuthal directions with an angle difference of $\sim 70^\circ$. Overall, the conclusions drawn from the ϕ scans on the configurations of the azimuthal domain variants in BLT films grown on four different miscut YSZ(100) substrates are clearly confirmed by the AFM investigations.

TEM characterizations confirmed the reduction of the number of the azimuthal domain variants in ferroelectric BLT thin films as well. Figure 6.14 shows plan-view TEM images of a BLT film on a YSZ(100) substrate with $\alpha=5^\circ$ and $\beta=45^\circ$ covered with an $\text{SrRuO}_3(110)$ electrode layer. The dark grains of elongated shape are (100)-oriented BLT grains. Most of the (100)-oriented grains have two specific azimuthal orientations, separated by $\sim 70^\circ$. Also on account of these two predominant azimuthal orientations, the electron diffraction pattern shown in the inset of Fig. 6.14(a) consists of only two rows of BLT(00 l) reflections in distinction to that of a BLT film grown on $\text{SrRuO}_3(110)$ (having four azimuthal domains) showing four rows of BLT (00 l) reflections (not shown here). Figure 6.14(b) is a magnified section of Fig. 6.14(a), exhibiting (100)-oriented grains showing the BLT (002) lattice fringes with a spacing of half of the c lattice parameter, corresponding to the Bi_2O_2 planes in BLT.

From the XRD, AFM, and TEM results it can be concluded that the respective reduced azimuthal domain characteristics of the SrRuO_3 films were inherited by the BLT films for all different types of miscut YSZ(100) single crystal substrates.

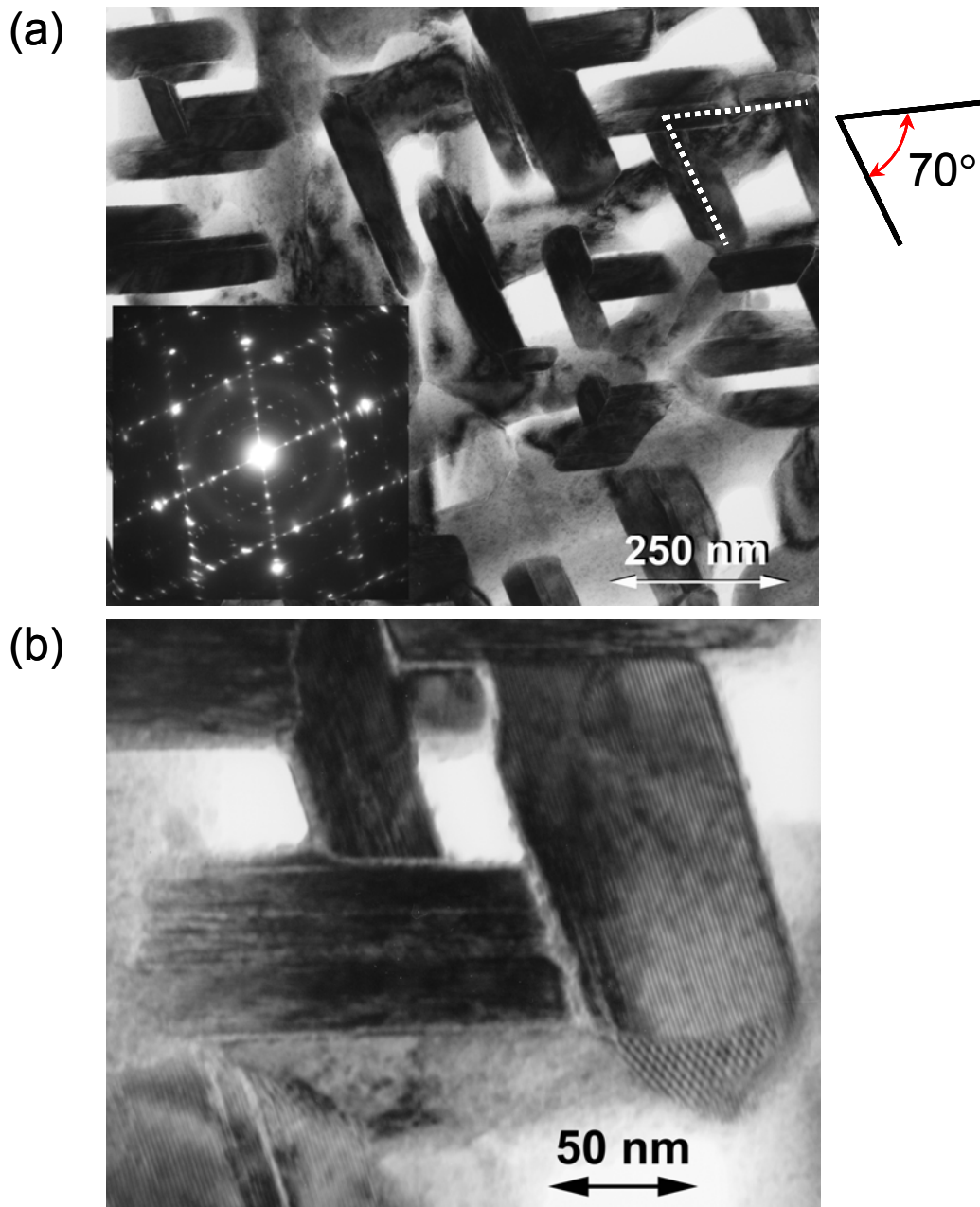


FIG. 6.14. (a) Plan-view transmission electron micrograph of a BLT film grown on (110)-oriented SrRuO_3 on a 5° [011] miscut YSZ(100) single crystal substrate ($\alpha=5^\circ$ and $\beta=45^\circ$). Two predominant grain orientations separated by $\sim 70^\circ$ are seen. The inset in (a) shows an electron diffraction pattern consisting of two rows of BLT (00 l) reflections. (b) Magnified section of (a) exhibiting the BLT(002) lattice fringes of (100)-oriented grains. The large spacings between the dark grains are filled with (118)-oriented BLT, and have partially been removed by the thinning process.

Ferroelectric properties

Figure 6.15 shows ferroelectric hysteresis loops recorded from BLT films grown on SrRuO_3 electrode layers on $\text{YSZ}(100)$ substrates with (a) $\alpha=1.5^\circ$ and $\beta=0^\circ$, (b) $\alpha=5^\circ$ and $\beta=45^\circ$, (c) $\alpha=1.5^\circ$ and $\beta=0^\circ$, and (d) $\alpha=5^\circ$ and $\beta=45^\circ$. The corresponding measured remanent polarization (P_r) of the BLT films are 9.9, 10.3, 11.7 and 12.5 $\mu\text{C}/\text{cm}^2$, respectively, for a maximum applied electric field of 433.3 kV/cm.

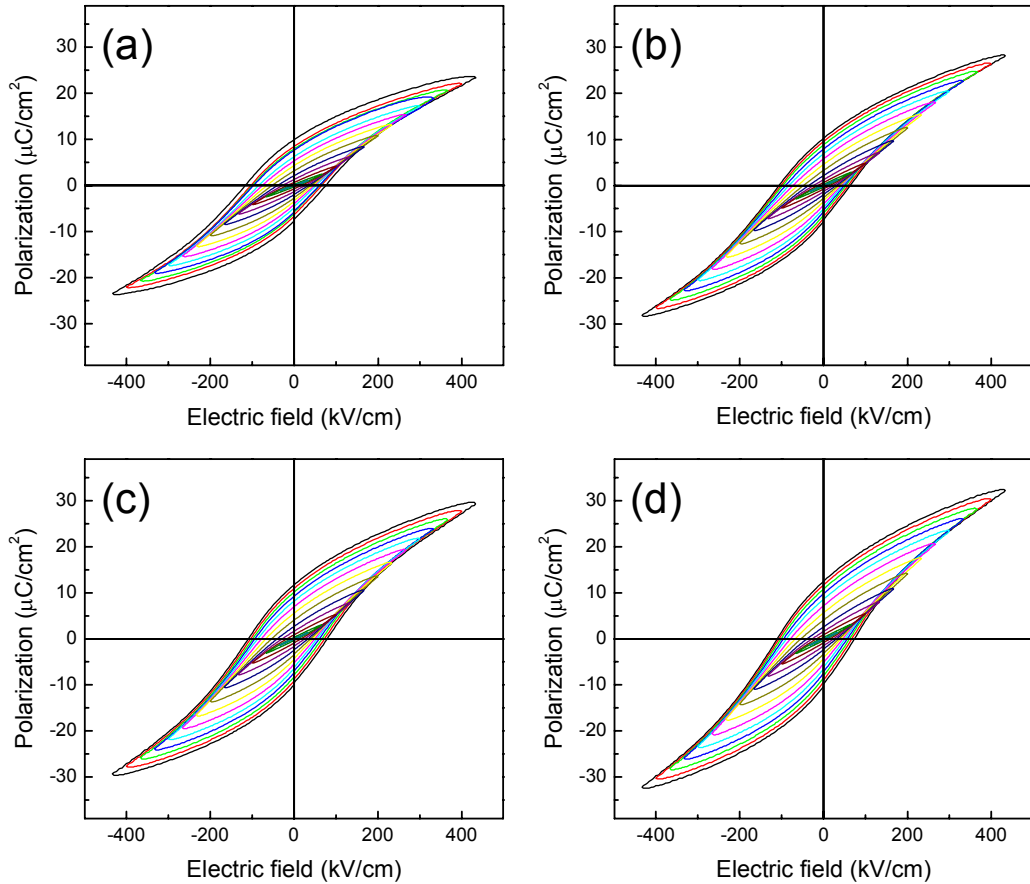


FIG. 6.15. P - E hysteresis loops of a Pt-BLT- SrRuO_3 capacitors on $\text{YSZ}(100)$ single crystal substrates with (a) $\alpha=1.5^\circ$ and $\beta=0^\circ$, (b) $\alpha=5^\circ$ and $\beta=0^\circ$, (c) $\alpha=1.5^\circ$ and $\beta=45^\circ$, and (d) $\alpha=5^\circ$ and $\beta=45^\circ$. The hysteresis loops were recorded at a frequency of 100 Hz. Different colors of P - E hysteresis loops stand for various applied electric fields.

Figure 6.16 summarizes the recorded remanent polarization of the BLT films grown on the four different $\text{YSZ}(100)$ substrates as a function of the applied electric field. Larger values of the remanent polarization were recorded in BLT films on $\text{YSZ}(100)$ substrates with 5° miscut angle and $\text{YSZ}[011]$ miscut direction. This is most probably due to the reduction of the number of the azimuthal domains which results in a lower areal density of azimuthal domain boundaries, which in turn might cause ferroelectric domain pinning or clamping. As

can be seen in Fig. 6.16, overall the BLT films on YSZ(100) with [011] miscut direction show higher remanent polarization than those on YSZ(100) with [001] miscut direction. It can be concluded that a substrate miscut direction is more effective than a substrate miscut angle for reducing azimuthal domain boundaries in the BLT film, thus for obtaining higher remanent polarization.

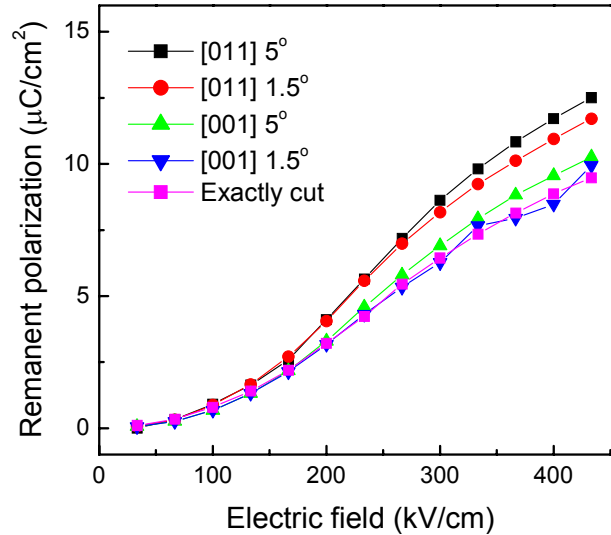


FIG. 6.16. Remanent polarization recorded as a function of the applied electric field for Pt-BLT-SrRuO₃ capacitors on different YSZ(100) single crystal substrates using the P - E hysteresis loops in Fig. 6.15. The remanent polarization values of the BLT film on YSZ(100) substrate with $\alpha=1.5^\circ$ and $\beta=0^\circ$ are similar to those of the BLT film the on an exactly cut YSZ(100) substrate.

6.3 Summary

In summary, a reduction of the number of azimuthal domain variants in SrRuO₃(110) electrode layers as well as in (100)/(118)-oriented BLT films has been achieved by using miscut YSZ(100) substrates. As a consequence, improved ferroelectric properties were achieved for BLT films with less azimuthal domains in the film. Annealing of the miscut YSZ single crystals substrates enhanced strongly the effect of the reduction of azimuthal domain variants. As the miscut angle is increased, this effect is unambiguously demonstrated. In addition, YSZ(100) substrates miscut towards the YSZ[011] direction are preferred to achieve uniformly reduced azimuthal domain variants. The value of remanent polarization recorded in BLT films on miscut YSZ(100) substrates with $\alpha=5^\circ$ and $\beta=45^\circ$ is higher than that in BLT films on other miscut YSZ(100) substrates. This observed improvement of the ferroelectric properties with reduced domain number is probably due to a reduced pinning or clamping effect of the ferroelectric domains at the azimuthal domain boundaries.

Chapter 7

Well-ordered large-area arrays of epitaxial ferroelectric La-substituted $\text{Bi}_4\text{Ti}_3\text{O}_{12}$ nanostructures of (001), (118)/(100), and (104) orientations

For high density memory applications of bismuth-layered perovskite oxides, such as $\text{Bi}_4\text{Ti}_3\text{O}_{12}$ or lanthanum-substituted $\text{Bi}_4\text{Ti}_3\text{O}_{12}$ (BLT), in integrated microelectronics these materials have to be patterned down to the nanometer range [121]. For example, a memory density of 2.5 Gbit/cm^2 requires the production of an array of $50,000 \times 50,000$ memory cells on a $1 \times 1 \text{ cm}^2$ substrate, whereby each of the cells would have a maximum lateral size of $200 \times 200 \text{ nm}^2$. In addition, each of the cells should retain its ferroelectric – or, in case of a micromechanical application, piezoelectric – properties, in spite of the very small size. However ferroelectricity vanishes below a critical size due to a weakening of the cooperative driving force which relies on the interaction of neighboring permanent electric dipoles in a crystal lattice, and an increasing depolarizing electrostatic field caused by dipoles at the ferroelectric-metal interfaces [122]. There are only few reports on the effect of size reduction for ferroelectric $\text{Bi}_4\text{Ti}_3\text{O}_{12}$ or BLT materials [123]. The size effect thus remains one of the most important issues in the field of ferroelectrics. Pertinent studies of size effects in ferroelectrics should enable the discrimination between intrinsic and extrinsic size effects. Such studies require, however, high quality single crystal nanoscale structures and eventually perfectly ordered arrays.

To date, various attempts to fabricate nanostructured ferroelectric materials by electron beam direct writing [124,125], focused ion beam milling [126,127], nanoimprint lithography [128], self-patterning methods [129,130], and nanosphere lithography [131], have been reported. Most of the above methods are unfortunately not appropriate to fabricate two-

dimensionally (2D) periodic large-area arrays of nanoscale structures because of some drawbacks such as high cost, scalability limit, and long processing time.

Very recently, our group proposed a useful technique to create periodic arrays of nanostructures [132]. A simple and general method for fabricating well-ordered arrays of gold nanotubes within a membrane has been developed [133] and this membrane can be used as a shadow mask for generating well-resolved 2D periodic nanostructures arrays.

In the following I report on the fabrication, crystallographic structure and ferroelectric properties of two-dimensionally periodic, hexagonally ordered, large-area arrays of BLT nanostructures epitaxially grown on SrRuO_3 electrode layers on SrTiO_3 single crystal substrates with (001), (011), and (111) orientation, respectively, using gold nanotube membranes of square millimeter or square centimeter sizes as shadow masks.

7.1 Experiment

The whole fabrication process of periodic arrays of ferroelectric BLT nanostructures is schematically illustrated in Fig. 7.1. First of all, SrRuO_3 bottom electrodes, also serving as epitaxial templates, were deposited by pulsed laser deposition (PLD) onto the SrTiO_3 single crystal substrates employing a KrF excimer laser ($\lambda=248$ nm) operated at a repetition rate of 5 Hz. Again perovskite-type SrRuO_3 proves to be a very good electrode material because it is well lattice matched with SrTiO_3 and chemically compatible with both ferroelectric and substrate. SrRuO_3 films with thicknesses of 10 to 20 nm were grown with a stoichiometric target onto SrTiO_3 single crystal substrates at a substrate temperature of 700 °C in an oxygen pressure of 0.14 mbar using a laser energy fluence of 1.7 J/cm².

Gold nanotube membranes with sizes of 2×2 mm² and 10×10 mm² were transferred onto the SrRuO_3 -covered SrTiO_3 substrates as shadow masks, immediately after SrRuO_3 deposition. Details on the fabrication of these free-standing large area gold nanotube membranes are reported elsewhere [133]. Perfectly ordered nanoporous anodic alumina oxide (AAO) templates were electrochemically covered by gold. By a wet-chemical etch the resulting gold nanotube membrane is detached from the oxide pore structure and subsequently transferred to the desired substrate.

The $\text{SrRuO}_3/\text{SrTiO}_3$ substrate covered by the gold membrane mask was loaded into the PLD chamber that was pumped down to 2×10^{-7} mbar. The deposition of BLT through the gold nanotubes was carried out at room temperature in an oxygen pressure of 1×10^{-4} mbar using a laser energy fluence of 2.3 J/cm². After BLT deposition, the nanostructures were obtained by simply mechanically lifting off the gold membranes. To obtain crystalline BLT nanostructures and to ensure ferroelectric properties, the as-deposited amorphous structures were crystallized at 700 °C for 30 min in a pure oxygen-flow ambient using a quartz tube furnace. In this way, large areas (from 2×2 mm² to about 10×10 mm²) of well-ordered BLT nanostructures with

hexagonal arrangement can be fabricated.

The surface topography of the BLT nanostructure arrays was investigated by atomic force microscopy (AFM) working in tapping mode and by scanning electron microscopy (SEM). Crystallographic orientation and epitaxial relations were characterized by x-ray diffraction (XRD) pole figures. Transmission electron microscopy (TEM) in cross-section geometry was used for the microstructure characterization. The ferroelectric properties were studied by piezoresponse scanning force microscopy (PFM).

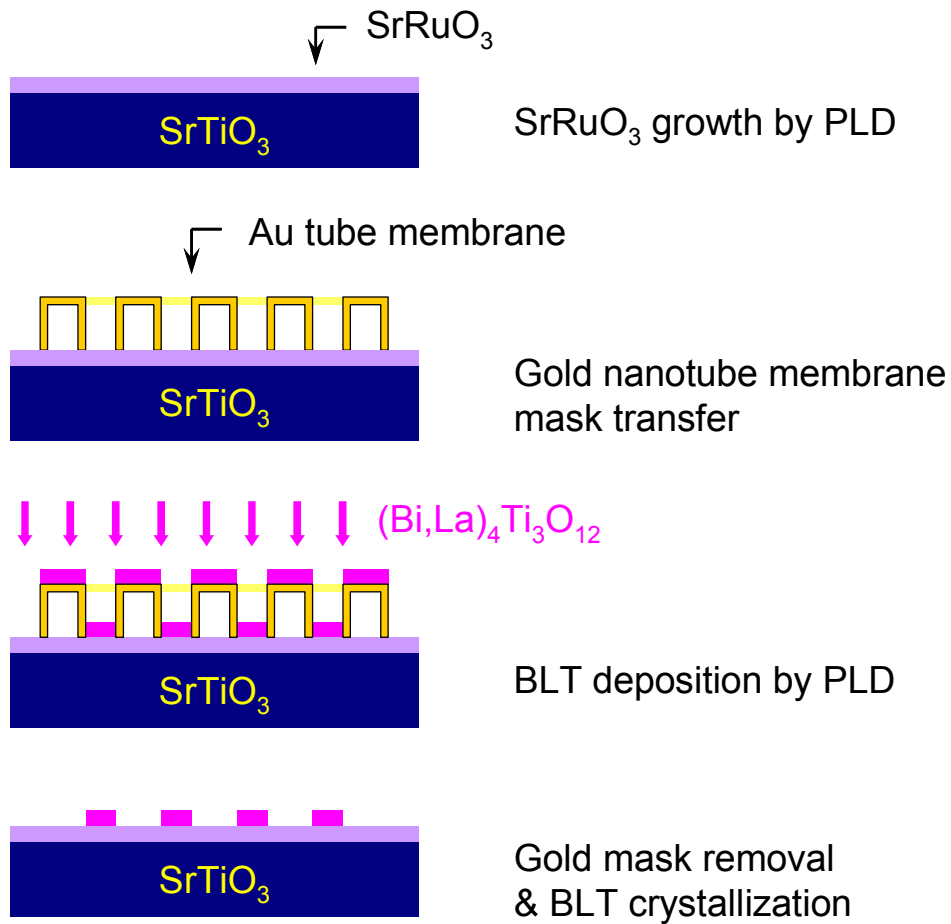


FIG. 7.1. Flow chart of the experimental procedure to fabricate periodic arrays of ferroelectric BLT nanostructures.

7.2 Results and discussion

7.2.1 Preparation of gold nanotube membranes [133]

Figure 7.2 shows various SEM images of gold nanotube membranes fabricated from an as-prepared AAO template. The two sides of the gold nanotube membranes are not identical. As can be seen in Fig. 7.2(a), the front side is composed of a hexagonal arrangement of nanopores with a center-to-center distance of 500 nm. The average pore diameter of the gold nanotube membrane estimated from the front surface turned out to be around 150 nm. On the other hand, the other side of the gold nanotube membrane has a completely different surface morphology with a uniform array of gold nanotubes, as shown in Figs 7.2(b), 7.2(c), and 7.2(d). Figures 7.2(b) and 7.2(c) show a top view of the gold nanotube arrays revealing the open ends of the individual nanotubes. As clearly shown in Fig. 7.2(d), the gold nanotubes have a funnel-shape morphology. The channel diameter of the gold nanotubes was estimated to be about 150 nm as well.

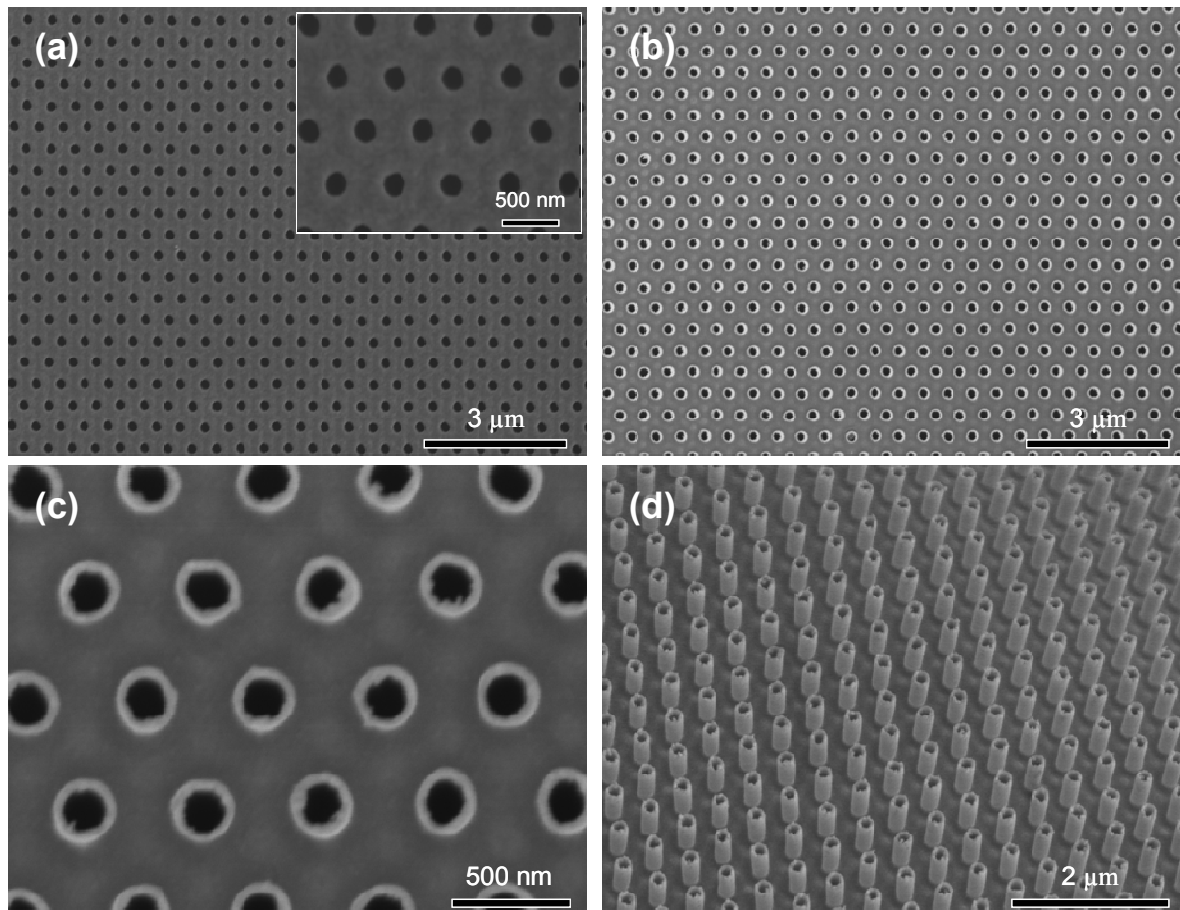


FIG. 7.2. Representative scanning electron micrographs of the gold nanotube membranes; (a) front surface view with the inset of a magnified image, (b) back surface view, (c) magnified view of (b), and (d) back surface tilted view, illustrating the three-dimensional structure of the membrane.

7.2.2 La-substituted $\text{Bi}_4\text{Ti}_3\text{O}_{12}$ nanostructures

Scanning electron microscopy

The fabricated gold nanotube membranes were used as shadow masks to generate the 2D arrays of ferroelectric nanostructures. Figure 7.3 shows SEM images of a BLT nanostructure array as-deposited on a SrTiO_3 substrate covered with a SrRuO_3 electrode layer. A similar technique using closed-packed latex sphere monolayers as deposition shadow masks to fabricate ferroelectric nanostructures was reported [131,134]. For that technique it is difficult to obtain large areas of well-ordered arrays because of many stacking faults occurring in the monolayer. However, as can be seen in Fig. 7.3, I achieved a large area (typical area: $\sim 10 \times 10 \text{ mm}^2$) of well-ordered arrays of BLT nanostructures with good hexagonal arrangement. Individual BLT nanostructures were spatially apart by 500 nm (see inset in Fig. 7.3) which is identical to the intertube distance of the gold nanotube membrane.

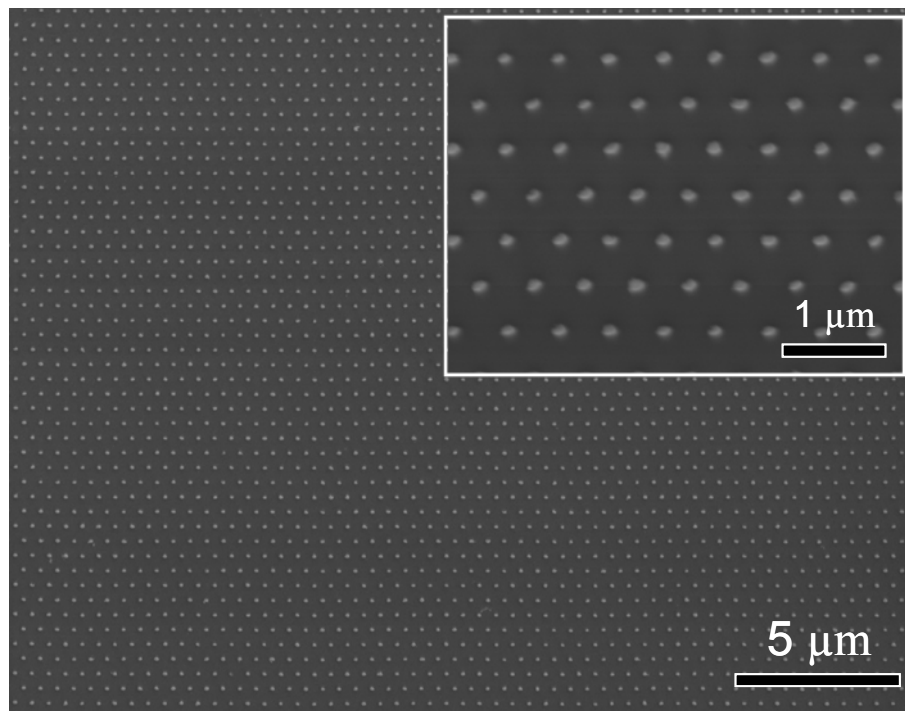


FIG. 7.3. Typical scanning electron micrograph of a BLT nanostructure array as-deposited on a SrRuO_3 -covered SrTiO_3 single crystal substrate using a gold nanotube membrane. The inset shows the hexagonal arrangement of the BLT nanostructures with a center-to-center distance of 500 nm.

Atomic force microscopy

In order to make a comparison between the sizes of the BLT nanostructures before and after annealing and to analyze the lateral and vertical sizes, AFM characterization was performed. Figures 7.4(a) and 7.4(b) show AFM topography images of as-deposited and crystallized BLT nanostructures on $\text{SrRuO}_3/\text{SrTiO}_3$ substrates. Figures 7.4(c) and 7.4(d) represent corresponding section profiles. From the AFM images of the BLT nanostructures taken before and after annealing, I observed that after annealing, the 2D periodic arrays of the BLT nanostructures with hexagonal arrangement were retained. Ferroelectric nanostructures fabricated by chemical solution deposition (CSD) generally show some deformation and

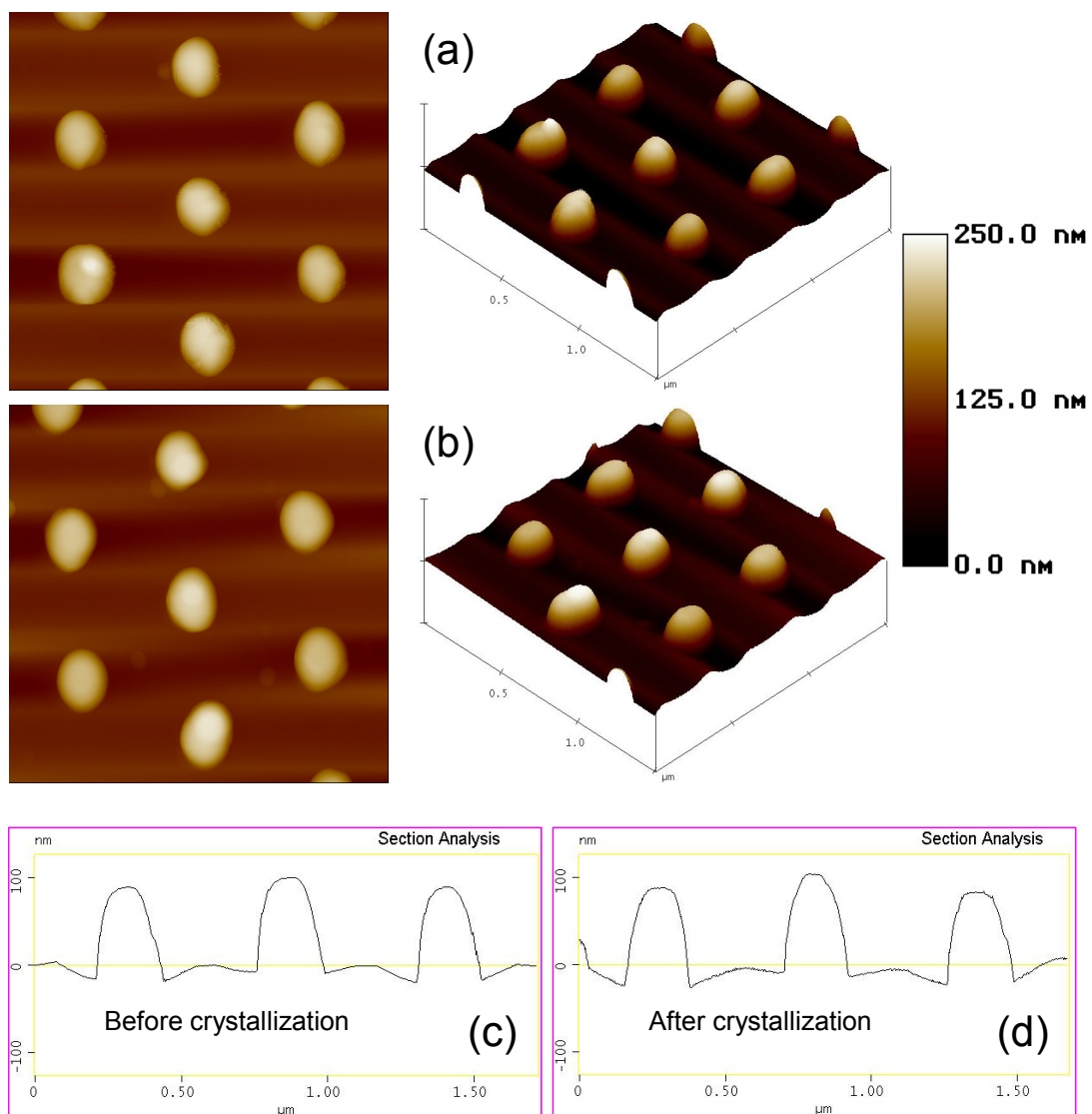


FIG. 7.4. Comparison of AFM topography images [(a) and (b)] and corresponding section analysis profiles [(c) and (d)] between the as-deposited BLT nanostructures [(a) and (c)] and crystallized BLT nanostructures [(b) and (d)]. The image size of (a) and (b) is $1.5 \times 1.5 \mu\text{m}^2$

shrinkage in their shape and size during the crystallization process. Moreover, for $\text{SrBi}_2\text{Ta}_2\text{O}_9$ nanostructures on Nb-doped $\text{SrTiO}_3(111)$ substrates produced by PLD, a shrinkage in vertical and lateral dimension was reported because of a high crystallization temperature of 950°C [134]. No significant shrinkage or deformation was observed in my BLT nanostructures. In most of the cases the BLT nanostructures have an oval shape and their average height and lateral size are about 100 nm and about 150 nm respectively. The oval shape might be either a result of a rather elliptical shape of the gold nanotubes [Figs. 7.2(c) and 7.2(d)] or of a small shadow effect that may occur during BLT deposition.

X-ray diffraction pole figures

Although the BLT nanostructures were amorphous after the lift-off process, and then *ex-situ* crystallized, I obtained epitaxial BLT nanostructures with good epitaxy relations with respect to the corresponding SrTiO_3 substrates. Due to the large size of the BLT nanostructure arrays, XRD was directly applicable. Figure 7.5 shows XRD pole figures of BLT nanostructure arrays on (a) (001)- (b) (011)-, and (c) (111)-oriented SrTiO_3 substrates, respectively. The fixed 2θ angle used to record the pole figures was 30.1° corresponding to the BLT 117 planes. In the case of the (001)-oriented BLT nanostructure arrays shown in Fig. 3(a), four reflection peaks are observed at $\psi \approx 51^\circ$ revealing a single-domain situation; the BLT 117 planes have a tilt angle of 50.7° with respect to the BLT (001) plane, which is parallel to the substrate surface. ($\psi=90^\circ$ corresponds to the substrate surface being parallel to the plane defined by the incident and reflected x-ray beam.)

The pole figure of the BLT nanostructures on the $\text{SrRuO}_3(011)/\text{SrTiO}_3(011)$ substrate is more complex, as can be seen in Fig. 7.5(b). First of all, it consists of a set of peaks (marked “A”) that stem from a (100)-oriented part of the BLT nanostructures, and of another set (marked “B”) which stems from a (118)-oriented part. Second, the peaks corresponding to the (118) orientation indicate the presence of two types of azimuthal domains. Set “A” appears at $\psi \approx 57^\circ$ and consists of the 117, $1\bar{1}\bar{7}$, $11\bar{7}$, and $1\bar{1}\bar{7}$ reflections from the (100)-oriented part indicating that this part has a single domain situation. Set “B” appears at $\psi \approx 4^\circ$, 65° , and 82° corresponding to 117, $\bar{1}17/1\bar{1}\bar{7}$, and $11\bar{7}$ reflections from the (118)-oriented part of the BLT nanostructures [cf. the angles $\angle(118) : (117) = 3.8^\circ$, $\angle(118) : (\bar{1}17) = 64.1^\circ$, $\angle(118) : (1\bar{1}\bar{7}) = 64.6^\circ$, and $\angle(118) : (11\bar{7}) = 82.4^\circ$]. A detailed analysis reveals that the (118)-oriented BLT nanostructures occur with two azimuthal domains, i.e., in exactly that double-twin situation which is well-known from (118)-oriented BLT thin films [95]. Moreover the mix of the (118) and (100) orientations of BLT thin films epitaxially grown on $\text{SrTiO}_3(011)$ substrates covered with about 15 nm thick SrRuO_3 electrode layer has been demonstrated in Chapter 4. Cross-sectional electron diffraction patterns (not shown) point to the additional presence of a minor (117) orientation of BLT as well.

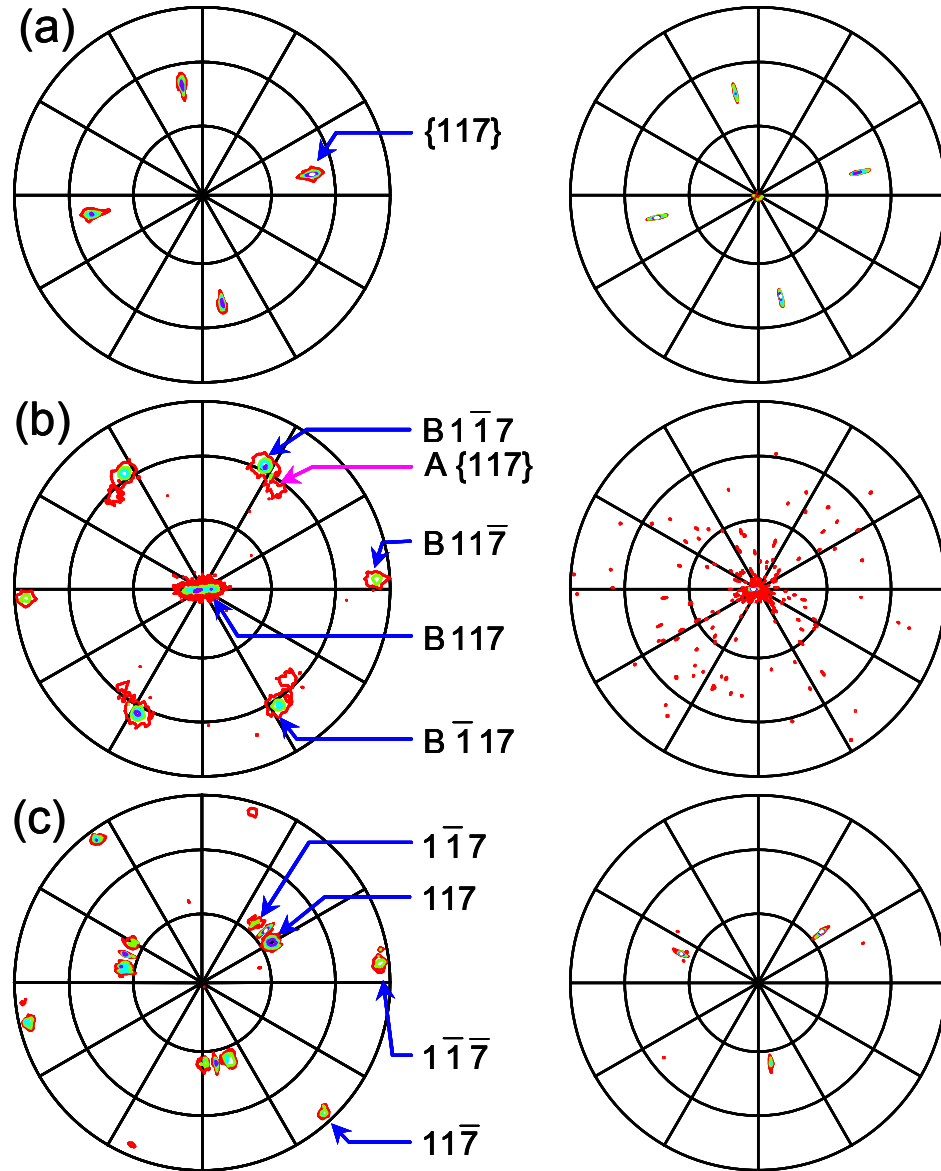


FIG. 7.5. X-ray diffraction pole figures of BLT nanostructures (left-hand side) on SrRuO_3 -covered (a) (001)-, (b) (011)-, and (c) (111)-oriented SrTiO_3 substrates. Pole figures of the corresponding bare $\text{SrRuO}_3/\text{SrTiO}_3$ substrates (right-hand side). The fixed 2θ angle was 30.1° corresponding to the BLT 117 reflection. Peaks originating from (100)- and (118)-oriented parts of the BLT nanostructures are denoted “A” and “B”, respectively in Fig. 7.5(b). The center and the rim of the pole figure correspond to $\psi=0^\circ$ and 90° , respectively.

Finally, in the case of BLT nanostructures on a $\text{SrRuO}_3(111)/\text{SrTiO}_3(111)$ substrate, a triple-twin situation was found as demonstrated by the pole figure shown in Fig. 7.5(c). The peaks at $\psi \approx 36^\circ$ from the 117 and $1\bar{1}7$ reflections as well as at $\psi \approx 84^\circ$ from the $11\bar{7}$ and $1\bar{1}\bar{7}$ reflections indicate the triple-twin situation, showing that the BLT (104) plane is parallel to the substrate plane, because the angle between the (104) and (117) planes of BLT is 36.4° [cf. the angles $\angle (104) : (117) = 36.4^\circ$, $\angle (104) : (1\bar{1}7) = 36.4^\circ$, $\angle (104) : (11\bar{7}) = 84.1^\circ$, and \angle

$(104) : (1\bar{1}\bar{7})=84.1^\circ$].

A closer look at the three different pole figures shows that additional reflection peaks are observed at $\psi \approx 45^\circ$ [Fig. 7.5(a)], $\psi \approx 0^\circ$ [Fig. 7.5(b)], and $\psi \approx 36^\circ$ [Fig. 7.5(c)]. To demonstrate their origin, pole figures of only the bare $\text{SrRuO}_3/\text{SrTiO}_3$ substrates were recorded for the three different substrates, at the same $2\theta=30.1^\circ$ corresponding to the BLT 117 planes as well. It turned out that the peaks with low reflection intensity in the left pole figures of Fig. 7.5 most probably are SrTiO_3 011 reflections because the used 2θ angle of the BLT 117 reflection is rather close to that of the SrTiO_3 011 reflection: The 2θ angle difference between BLT 117 and SrTiO_3 011 planes is only about 2.3° .

Transmission electron microscopy

Figure 7.6 shows a series of cross-sectional TEM images of different magnifications, taken on different samples. In evaluating these images, one has to keep in mind that during TEM cross-section preparation, some or all of the nanostructures of a certain image may have been cut non-centrally. In addition, the cut may have gone not exactly parallel to a line of the array, or may even cross different lines of the array. Occasional variations of the apparent spacing (pitch) between the nanostructures may have their origin in these effects. Figure 7.6(a) shows such a deviation from the otherwise regular spacing, in the middle of the image. Figure 7.6(b) shows some apparent, small variations of the shape of the nanostructures. Overall, Figs. 7.6(a) and 7.6(b) show, however, a rather uniform cell-to-cell shape and size. Fig. 7.6(c) shows a BLT nanostructure at somewhat higher magnification, revealing a trapezoidal shape projection. Finally Fig. 7.6(d) shows an electron diffraction pattern taken from a single BLT island of a BLT nanostructure array grown onto a $\text{SrTiO}_3(111)$ substrate. On the background of a diffuse ring pattern, which originates from the amorphous glue used to prepare the cross section, a rather regular spot pattern is visible. Because of the low volume of the island, the diffraction spots are weak; for better visibility a scanned negative is shown in inverted contrast. The negative is shown in the correct orientation with respect to the corresponding cross sectional TEM image [cf., e.g., Fig. 7.6(c)]. The orientation of the substrate surface is shown in green color, whereas the blue line marks the normal to the substrate. The (208) , (000) , and $(\bar{2}0\bar{8})$ reflections are all on this blue line, demonstrating the (104) orientation of the BLT nanostructure. Part of the other spots has also been indexed, which permitted the determination of the beam direction as $[\bar{4}\bar{3}1]$.

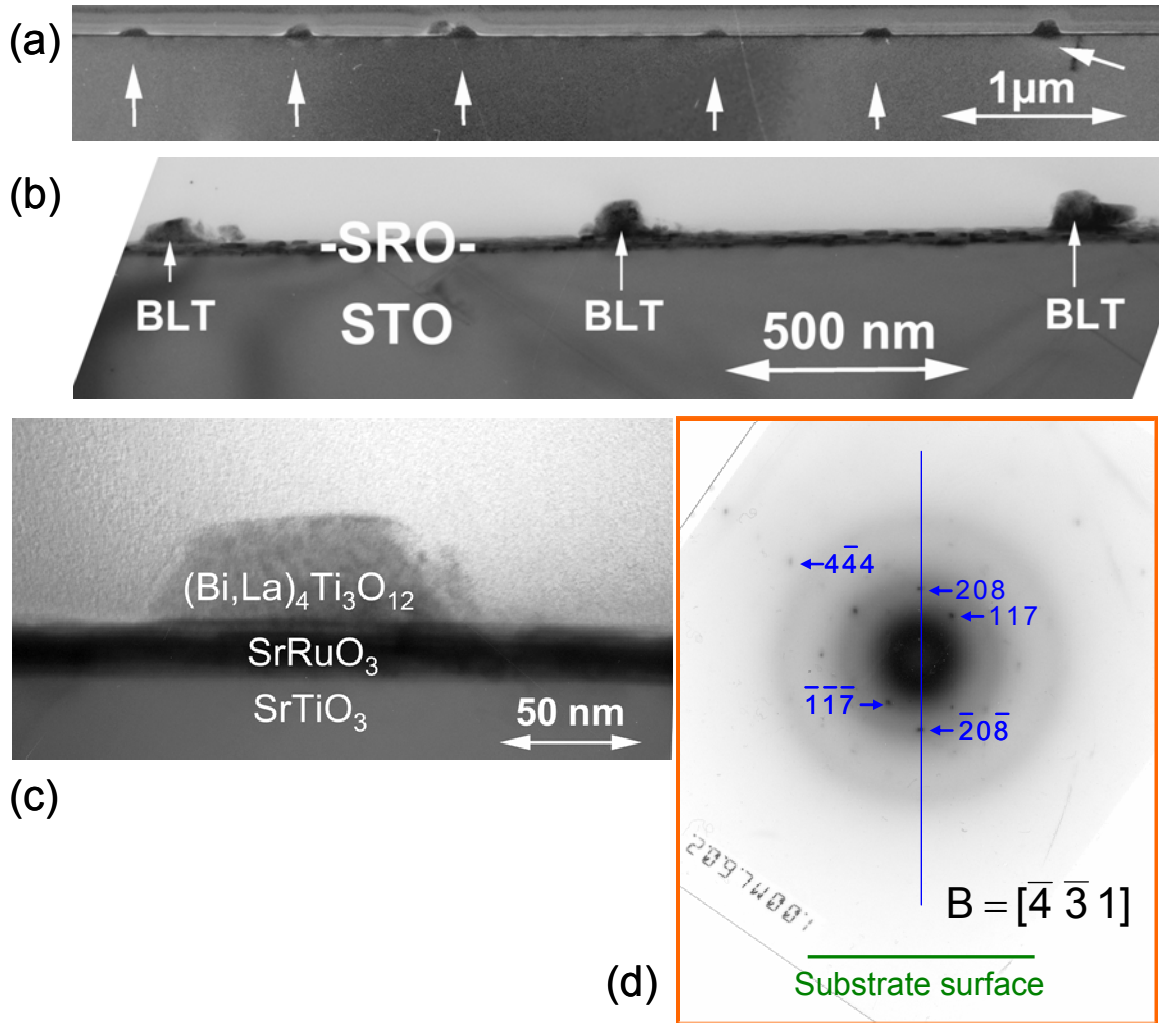


FIG. 7.6. [(a) to (c)] Cross-sectional transmission electron micrographs of different BLT nanostructure arrays, taken with different magnifications. (d) Cross-sectional diffraction pattern taken from a (104)-oriented BLT nanostructure grown on a SrRuO_3 -covered $\text{SrTiO}_3(111)$ substrate.

Ferroelectric characterization

In order to investigate whether the crystallized BLT nanostructures show ferroelectric switching, piezoelectric hysteresis loops and piezoresponse images were recorded using scanning force microscopy in the piezoresponse mode (PFM). Figure 7.7(a) shows a typical piezoelectric hysteresis loop recorded from a c -axis-oriented BLT nanostructure on a $\text{SrRuO}_3(001)/\text{SrTiO}_3(001)$ substrate. The measured value of the effective remanent piezoelectric coefficient ($2d_{zz}$) is 5.0 pm/V (positive $d_{zz} = -0.1 \text{ pm/V}$ and negative $d_{zz} = -5.1 \text{ pm/V}$) for a maximum applied voltage of 5 V. As already known, c -axis-oriented SBT films do not exhibit any ferroelectricity, but c -axis-oriented $\text{Bi}_4\text{Ti}_3\text{O}_{12}$ exhibits a distinct piezoelectric hysteresis loop with weak ferroelectricity [135]. Figures 7.7(b) and 7.7(c) show

the typical surface morphology and the corresponding ferroelectric domain structure of BLT nanostructures, respectively. White and black contrast regions in the piezoresponse image generally correspond to positive (polarization upward) and negative (polarization downward) ferroelectric domains, respectively. The regions without a net black or white contrast correspond to areas of the sample that possess no piezoelectric behavior. The out-of-plane piezoresponse image [Fig. 7.7(c)] reveals a weak contrast within each c -axis-oriented BLT nanostructure and almost no contrast in the SrRuO_3 electrode layer (“gray”). Due to the presence of the small component of spontaneous polarization of $\text{Bi}_4\text{Ti}_3\text{O}_{12}$ as well as BLT along the crystallographic c axis, their piezoelectric coefficient d_{zz} does not vanish. The weak contrast in c -axis-oriented BLT nanostructures indicates a small reversible switching of the polarization along their c axis.

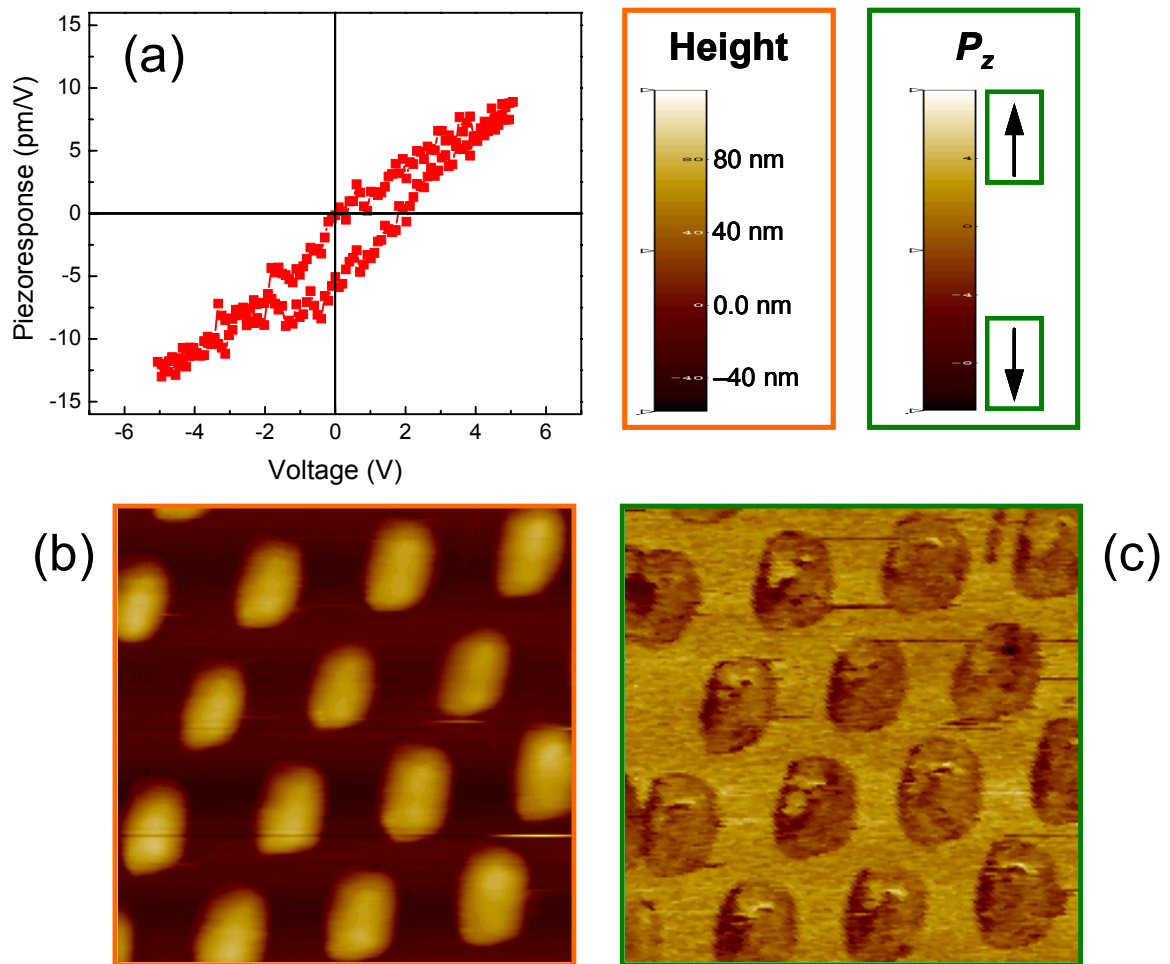


FIG. 7.7. (a) Piezoresponse hysteresis loop, (b) topography image, and (c) piezoresponse image (out-of-plane) of BLT nanostructures grown on a $\text{SrRuO}_3(001)$ -covered $\text{SrTiO}_3(001)$ substrate. The image size of (b) and (c) is $1.5 \times 1.5 \mu\text{m}^2$.

Figures 7.8(a) and 7.8(b) show a well-defined piezoelectric hysteresis loop and AFM topography image recorded from a (118)/(100)-oriented BLT nanostructure. It was found that a considerably higher value of the effective piezoresponse coefficient ($2d_{zz}$) of 38 pm/V was obtained from the BLT nanostructures on the $\text{SrRuO}_3(011)/\text{SrTiO}_3(011)$ substrate than from those on $\text{SrRuO}_3(001)/\text{SrTiO}_3(001)$. In spite of the image noise, a uniformly strong contrast of the BLT nanostructures was observed in both out-of-plane [Fig. 7.8(c)] and in-plane [Fig. 7.8(d)] piezoresponse images which results in the high piezoelectric coefficient. A similar effective piezoelectric coefficient (d_{zz}) of 19 pm/V has been reported in $1 \mu\text{m}$ thick polycrystalline $\text{Bi}_{3.25}\text{La}_{0.75}\text{Ti}_3\text{O}_{12}$ thin films made by CSD, determining the slope of field-induced strain loops [136].

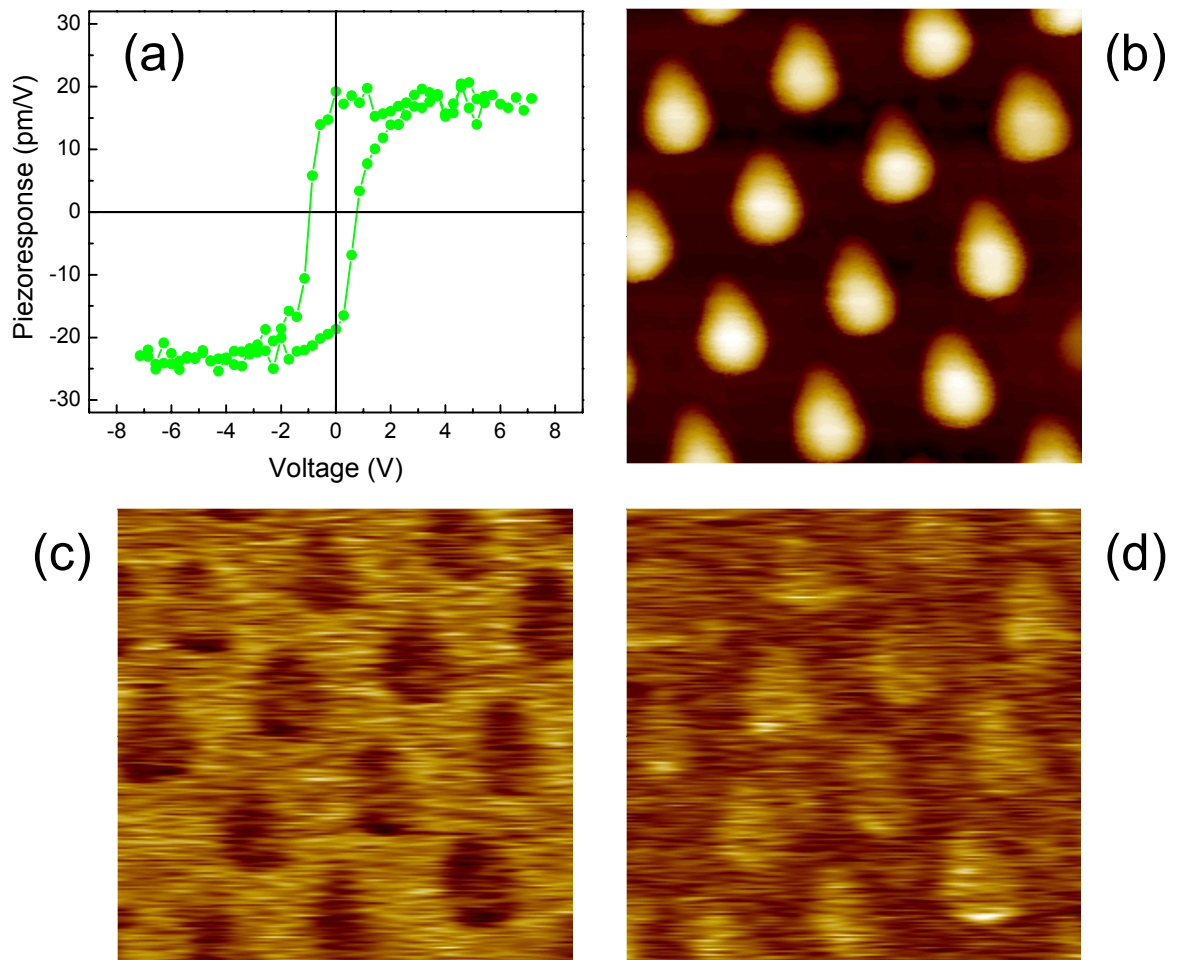


FIG. 7.8. (a) Piezoresponse hysteresis loop, (b) topography image, (c) out-of-plane piezoresponse image, and (d) in-plane piezoresponse image of BLT nanostructures grown on a $\text{SrRuO}_3(011)$ -covered $\text{SrTiO}_3(011)$ single crystal substrate. The image size of (b) to (d) is $1.5 \times 1.5 \mu\text{m}^2$.

Figures 7.9(a) and 7.9(b) show a piezoelectric hysteresis loop and an AFM topography image recorded from (104)-oriented BLT nanostructures on a $\text{SrRuO}_3(111)$ -covered $\text{SrTiO}_3(111)$ substrate, revealing a lower piezoelectric coefficient ($2d_{zz}=1.4 \text{ pm/V}$) than on BLT nanostructures on $\text{SrRuO}_3(011)/\text{SrTiO}(011)$ and on $\text{SrRuO}_3(001)/\text{SrTiO}_3(001)$ substrates. This result of a low piezoelectric coefficient is not consistent with the polarization value of bulk BLT because it has been already demonstrated that non- c -axis-oriented BLT films have a higher polarization component than c -axis-oriented ones. I suggest that the result might be explained by the investigation of the corresponding piezoresponse image. Compared with piezoresponse images of BLT nanostructures on $\text{SrRuO}_3(011)/\text{SrTiO}(011)$ substrates, an inhomogeneous contrast within individual BLT nanostructures is seen in both out-of-plane [Fig. 7.9(c)] and in-plane [Fig. 7.9(d)] piezoresponse images. This means that two opposite polarization states are present simultaneously and therefore a net polarization state is detected, although my BLT nanostructures have the same crystallographic orientation confirmed by XRD and TEM. It is well known that the magnitude of the piezoresponse signal depends on

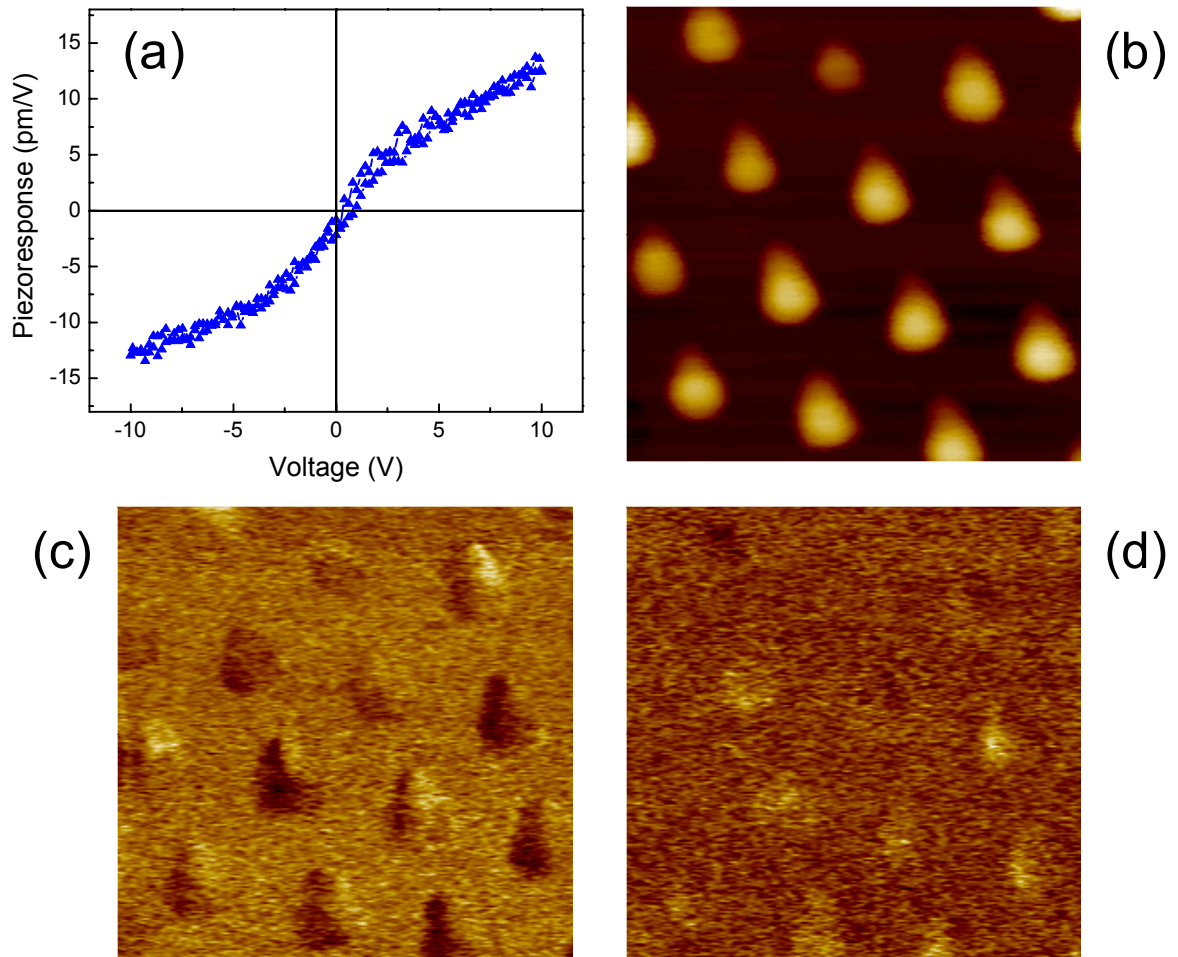


FIG. 7.9. (a) Piezoresponse hysteresis loop, (b) topography image, (c) out-of-plane piezoresponse image, and (d) in-plane piezoresponse image of BLT nanostructures grown on $\text{SrRuO}_3(111)$ -covered $\text{SrTiO}_3(111)$ single crystal substrate. The image size of (b) to (d) is $1.5 \times 1.5 \mu\text{m}^2$.

the component of the spontaneous polarization normal to the substrate surface. However, the exact relationship $d_{zz}(\theta)$ (where θ is the angle between the measurement direction and the [001] crystallographic axis of the tested grain) is governed by the transformation rules of the whole piezoelectric tensor, which may be closely related to the component of the vector of polarization normal to the substrate surface, but not directly proportional to it [137].

In addition, the exact relationship between the piezoelectric response signal and the ferroelectric polarization for BLT or $\text{Bi}_4\text{Ti}_3\text{O}_{12}$ (monoclinic symmetry) is complicated. The effective piezoelectric coefficient d_{zz} depends not only on θ but also on the azimuthal angle ϕ (in-plane orientation). This means that ferroelectric domains have the same remanent polarization but different orientations of the in-plane component of polarization have different effective piezoelectric coefficients and therefore different piezoelectric response signals. In detail, Harnagea *et al.* suggested the shape of the $d_{zz}(\theta, \phi)$ surface for $\text{Bi}_4\text{Ti}_3\text{O}_{12}$ [137]. They calculated the $d_{zz}(\theta, \phi)$ surface as a function of the direction for monoclinic symmetry using piezoelectric coefficients obtained by Sa Neto and Cross [138]. According to their calculation, the depicted piezoelectric surface showed that the maximum of the piezoelectric coefficient does not occur along the direction of the spontaneous polarization, but it has lobes protruding nearly along the a and c axes.

7.3 Summary

Well-ordered large-area arrays of epitaxial La-substituted $\text{Bi}_4\text{Ti}_3\text{O}_{12}$ nanostructures with (001), (118)/(100), and (104) orientations have been achieved on SrRuO_3 -covered SrTiO_3 substrates of (001), (011), and (111) orientations. The arrays were achieved using a liftoff method based on gold nanotube membranes as shadow masks. Epitaxial BLT nanostructures with a height of about 65 nm and a lateral size of about 150 nm have been obtained. In spite of their small lateral size and thickness, the nanostructures of the arrays were clearly revealed to have ferroelectric properties, the values of which depend on their crystallographic orientation. Among them, a maximum effective piezoresponse coefficient ($2d_{zz}$) of about 38.0 pm/V was obtained in (118)/(100)-oriented BLT nanostructures on SrRuO_3 (011)-covered SrTiO_3 (001) substrates. Although (104)-oriented BLT nanostructures show a piezoresponse image contrast in both in-plane and out-of plane images, revealing a switchable polarization, they exhibit a smaller piezoelectric coefficient ($2d_{zz}=1.4$ pm/V) than the others.

Chapter 8

Conclusions and future work

In the course of this study, epitaxially twinned ferroelectric bismuth-layered perovskite materials of lanthanum-substituted $\text{Bi}_4\text{Ti}_3\text{O}_{12}$ (BLT) and neodymium-substituted $\text{Bi}_4\text{Ti}_3\text{O}_{12}$ (BNT) have been successfully grown by pulsed laser deposition (PLD). According to the purpose of the study, appropriate substrates were chosen to grow the epitaxial films and epitaxial nanostructures.

Due to the highly anisotropic structure of BLT, its ferroelectric properties are also anisotropic. This has been demonstrated using different SrTiO_3 single crystal substrates of (001), (011), and (111) orientations to control the BLT film orientation. The ferroelectric anisotropy is clearly revealed by measuring the remanent polarizations of (001)-, (118)-, and (104)-oriented BLT films. The (001)-oriented (*c*-axis-oriented) BLT films show a small polarization component ($2P_r=0.81 \mu\text{C}/\text{cm}^2$), revealing that the vector of the spontaneous polarization is directed (almost) perpendicular to the *c* axis. The polarization component $2P_r$ of the (104)-oriented BLT films is about 1.5 times larger than that of the (118)-oriented films in accordance with the predictions. BLT films grown on a thin SrRuO_3 bottom electrode ($t\sim 15$ nm) on $\text{SrTiO}_3(011)$ consist of a mix of (118) and (100) orientations.

The integration of non-*c*-axis oriented bismuth-layered perovskite materials into silicon technology is required to produce commercially viable high-density non-volatile memories and other devices. In order to grow uniformly non-*c*-axis-oriented BLT and BNT films on Si(100), SrRuO_3 -covered Pt(111) electrodes have been grown on YSZ(100)-buffered Si(100) substrates by rf sputtering. Due to the fourfold symmetry of YSZ(100) and the threefold symmetry of the Pt(111) plane these electrodes are multiply twinned. (104)-oriented ferroelectric $\text{Bi}_{3.25}\text{La}_{0.75}\text{Ti}_3\text{O}_{12}$ and $\text{Bi}_{3.54}\text{Nd}_{0.46}\text{Ti}_3\text{O}_{12}$ thin films have been grown onto this

surface. These ferroelectric films are also multiply twinned, inheriting this property from the electrodes. However, all of the azimuthal domains (twins) potentially have the same component P_{\perp} of the polarization vector perpendicular to the film plane. The BNT films show a higher polarization value than the BLT films due to the structurally higher distortion of the TiO_6 octahedra in the perovskite block. It originates from the smaller ionic radius of Nd^{3+} compared to La^{3+} . These (104)-oriented BLT and BNT films on Si(100) have thus good ferroelectric properties and should be suitable for applications in a number of silicon-based microtechnologies.

Azimuthal domain boundaries within films can affect the electrical properties of the films because they are composed of many associated defects and are not fully crystallized. It is demonstrated that BLT films epitaxially grown on buffered Si(100) substrates involve more azimuthal domains than those grown on SrTiO_3 single crystal substrates and therefore they have more azimuthal domain boundaries. It has been shown that the number of azimuthal domain variants in SrRuO_3 electrode layers as well as in BLT films can be reduced by using miscut yttria-stabilized zirconia (YSZ) substrates. Both miscut angle and miscut direction of YSZ(100) substrates play an important role in reducing the number of the azimuthal domain variants. In this study, a reduction of the number of azimuthal domain variants by 50% was achieved on YSZ(100) substrates with a miscut direction of YSZ[011] and a miscut angle of 5° . BLT films deposited on SrRuO_3 (110)-covered YSZ(100) substrates of this kind show improved ferroelectric properties, compared to BLT films on exactly cut YSZ(100) substrates. Furtheron, it is expected that miscut Si(100) substrates also enable the reduction of azimuthal domain variants in ferroelectric BLT films as well as SrRuO_3 electrode layers. In the case of miscut Si(100) substrates, however, a most careful substrate preparation will be required in order to obtain well-defined substrate surfaces through appropriate chemical and thermal treatment. In addition, it will be required to control the formation of the native SiO_x on the silicon surface due to the chemically easy reaction. This SiO_x layer on silicon may have a negative influence on the effect of the reduction of azimuthal domains in the overlying films. In addition, a possible negative effect of a miscut silicon substrate on the electronic properties of silicon devices such as field-effect transistors will have to be considered.

For ferroelectric random access memories with a memory density in the gigabit range, well-ordered ferroelectric nanostructures with a lateral size in the 100 nm range are required. It is important to understand whether or not such small structures are still ferroelectric, i.e., possess a spontaneous polarization which is switchable. Two-dimensionally well-ordered, large-area arrays of epitaxial BLT nanostructures have been achieved using gold nanotube membranes as liftoff masks. Epitaxial nanostructures with a height of about 65 nm and a lateral size of about 150 nm have been obtained. On the nanoscale, it is possible to control the orientation of the BLT nanostructures using (001)-, (011)-, and (111)-oriented SrTiO_3 substrates covered with SrRuO_3 bottom electrodes. Anisotropic properties in these BLT

nanostructures with different orientations have been found by piezoreponse force microscopy (PFM). Among them, the highest effective piezoresponse coefficient ($2d_{zz}$) of about 38.0 pm/V was obtained in (118)/(100)-oriented BLT nanostructures on SrRuO₃(011)/SrTiO₃(011). Although (104)-oriented BLT nanostructures show a piezoresponse image contrast both in in-plane and out-of plane images, revealing a switchable polarization, they exhibit a smaller piezoelectric coefficient ($2d_{zz}=1.4$ pm/V) than the others. This is inconsistent with theory and should be investigated further. Moreover, investigations of the size effects in terms of not only the height but also the lateral size of the BLT nanostructures are required.

In view of the structural similarity and wide chemical variability of materials with perovskite-derived crystal structures, the results of the present work are not only relevant to rare-earth-substituted bismuth titanates, but are of more general significance. Future work should demonstrate this. For example, non-(100)-oriented SrRuO₃ template layers, e.g., of (110) and (111) orientation, can serve to grow other types of ferroelectric oxides. Recently, BiFeO₃ has attracted much attention as it shows a coexistence of ferroelectric and magnetic ordering. It has ferroelectric properties with a high Curie temperature ($T_C \sim 850$ °C) and antiferromagnetic behavior with a corresponding Néel temperature ($T_N \sim 370$ °C). The BiFeO₃ crystallographic structure is a distorted rhombohedral perovskite, which belongs to the space group $R3c$. The rhombohedral unit cell parameters are $a_r=0.5634$ nm and $\alpha_r=59.348^\circ$. The crystallographic structure can be represented as nearly pseudo-cubic with lattice parameters $a_c=0.3963$ nm and $\alpha_c=89.40^\circ$. It has been reported that (001)_c-, (101)_c-, and (111)_c-oriented BiFeO₃ thin films were epitaxially grown on (100)-, (110), and (111)-oriented SrTiO₃ single crystal substrates, respectively, covered with SrRuO₃ [139,140]. Compared to the remanent polarization of (001)_c-oriented BiFeO₃ films (~ 55 $\mu\text{C}/\text{cm}^2$), BiFeO₃ films with (101)_c and (111)_c orientations showed higher polarization of ~ 80 $\mu\text{C}/\text{cm}^2$ and ~ 100 $\mu\text{C}/\text{cm}^2$, respectively. It has also been reported that (001)_c-oriented BiFeO₃ films having a remanent polarization of ~ 45 $\mu\text{C}/\text{cm}^2$ were epitaxially grown on SrRuO₃(001)-covered Si(100) substrates buffered with SrTiO₃ layers [141]. For a desirable compatibility with silicon-based microelectronics, epitaxial BiFeO₃ films with higher polarization should be grown on silicon substrates. It is likely that (110)- and (111)-oriented SrRuO₃ films as conducting template layers will enable the growth of (101)_c- and (111)_c-oriented BiFeO₃ films on Si(100) substrates. In other words, it is expected that (101)_c-oriented BiFeO₃ films can be grown on epitaxially (110)-oriented SrRuO₃-covered YSZ(100)/Si(100) substrates and BiFeO₃ with (111)_c orientation can be grown on (111)-oriented SrRuO₃-covered Pt(111)/YSZ(100)/Si(100) substrates. This example shows that the results of the present work can also be significant for multiferroic materials with a perovskite-derived crystal structure and should thus be of some general relevance.

Bibliography

- [1] O. Auciello, J. F. Scott, and R. Ramesh, *Phys. Today* **51**, 22 (1998).
- [2] J. F. Scott and C. A. P. de Araujo, *Science* **246**, 1400 (1989).
- [3] C. A. P. de Araujo, J. D. Cuchiaro, L. D. McMillan, M. C. Scott, and J. F. Scott, *Nature (London)* **374**, 627 (1995).
- [4] C. H. Ahn, T. Tybell, L. Antognazza, K. Char, R. H. Hammond, M. R. Beasley, Ø. Fisher, and J.-M. Triscone, *Science* **276**, 1100 (1997).
- [5] K. Kim and Y. J. Song, *Integr. Ferroelectr.* **61**, 3 (2004).
- [6] M. de Keijser and G. J. M. Dormans, *MRS Bull.* **21**, 37 (1996).
- [7] H. D. Chen, K. R. Udayakumar, C. J. Gaskey, and L. E. Cross, *Appl. Phys. Lett.* **67**, 3411 (1995).
- [8] H. M. Duiker, P. D. Beale, J. F. Scott, C. A. P. de Araujo, B. M. Melnick, J. D. Cuchiaro, and L. D. McMillan, *J. Appl. Phys.* **68**, 5783 (1990).
- [9] C. Sudhama, A. C. Campbell, P. D. Maniar, R. E. Jones, R. Moazzami, C. J. Mogab, and J. C. Lee, *J. Appl. Phys.* **75**, 1014 (1994).
- [10] H. Chen and J. Y. Lee, *J. Appl. Phys.* **82**, 3478 (1997).
- [11] G. Arlt and N. A. Pertsev, *J. Appl. Phys.* **70**, 2283 (1991).
- [12] U. Robels and G. Arlt, *J. Appl. Phys.* **73**, 3454 (1993).
- [13] O. Auciello, K. D. Gifford, and A. I. Kingon, *Appl. Phys. Lett.* **64**, 2873 (1994).
- [14] H. N. Al-Shareef, K. R. Bellur, A. I. Kingon, and O. Auciello, *Appl. Phys. Lett.* **66**, 239 (1995).
- [15] T. Nakamura, Y. Nakao, A. Kamisawa, and H. Takasu, *Appl. Phys. Lett.* **65**, 1522 (1994).
- [16] R. Ramesh, W. K. Chan, B. Wilkens, H. Gilchrist, T. Sands, J. M. Tarascon, V. G. Keramidas, D. K. Fork, J. Lee, and A. Safari, *Appl. Phys. Lett.* **61**, 1537 (1992).
- [17] R. Ramesh, H. Gilchrist, T. Sands, V. G. Keramidas, R. Haakenaasen, and D. K. Fork, *Appl. Phys. Lett.* **63**, 3592 (1993).
- [18] R. Dat, D. J. Lichtenwalner, O. Auciello, and A. I. Kingon, *Appl. Phys. Lett.* **64**, 2673 (1994).
- [19] R. Ramesh, J. Lee, T. Sands, V. G. Keramidas, and O. Auciello, *Appl. Phys. Lett.* **64**, 2511 (1994).
- [20] O. Auciello and R. Ramesh, *MRS Bull.* **21**, 31 (1996).
- [21] R. Dat, J. K. Lee, O. Auciello, and A. I. Kingon, *Appl. Phys. Lett.* **67**, 572 (1995).
- [22] T. Li, Y. Zhu, S. B. Desu, C.-H. Peng, and M. Nagata, *Appl. Phys. Lett.* **68**, 616 (1996).
- [23] K. Amanuma, T. Hase, and Y. Miyasaka, *Appl. Phys. Lett.* **66**, 221 (1995).
- [24] B. Aurivillius, *Ark. Kemi* **1**, 499 (1950).
- [25] C. H. Hervoches and P. Lightfoot, *J. Solid State Chem.* **153**, 66 (2000).
- [26] A. D. Rae, J. G. Thompson, and R. L. Withers, *Acta Crystallogr., Sect. B: Struct. Sci.*

- 48**, 418 (1992).
- [27] A. D. Rae, J. G. Thompson, R. L. Withers, and A. C. Willis, *Acta Crystallogr., Sect. B: Struct. Sci.* **46**, 474 (1990).
- [28] S. E. Cummins and L. E. Cross, *J. Appl. Phys.* **39**, 2268 (1968).
- [29] P. C. Joshi, S. B. Krupanidhi, and A. Mansingh, *J. Appl. Phys.* **72**, 5517 (1992).
- [30] T. Kijima, M. Ushikubo, and H. Matsunaga, *Jpn. J. Appl. Phys., Part 1* **38**, 127 (1999).
- [31] P. C. Joshi and S. B. Krupanidhi, *Appl. Phys. Lett.* **62**, 1928 (1993).
- [32] B. H. Park, B. S. Kang, S. D. Bu, T. W. Noh, J. Lee, and W. Jo, *Nature (London)* **401**, 682 (1999).
- [33] R. W. Wolfe and R. E. Newnham, *J. Electrochem. Soc.* **116**, 832 (1969).
- [34] T. Takenaka and K. Sakata, *Ferroelectrics* **38**, 769 (1981).
- [35] Y. Shimakawa, Y. Kubo, Y. Tauchi, H. Asano, T. Kamiyama, F. Izumi, and Z. Hiroi, *Appl. Phys. Lett.* **79**, 2791 (2001).
- [36] U. Chon, G.-C. Yi, and H. M. Jang, *Appl. Phys. Lett.* **78**, 658 (2001).
- [37] U. Chon, H. M. Jang, M. G. Kim, and C. H. Chang, *Phys. Rev. Lett.* **89**, 087601 (2002).
- [38] U. Chon, K.-B. Kim, H. M. Jang, and G.-C. Yi, *Appl. Phys. Lett.* **79**, 3137 (2001).
- [39] U. Chon, J. S. Shim, and H. M. Jang, *J. Appl. Phys.* **93**, 4769 (2003).
- [40] N. A. Pertsev, A. G. Zembilgotov, and A. K. Tagantsev, *Phys. Rev. Lett.* **80**, 1988 (1998).
- [41] J. H. Haeni, P. Irvin, W. Chang, R. Uecker, P. Reiche, Y. L. Li, S. Choudhury, W. Tian, M. E. Hawley, B. Craigo, A. K. Tagantsev, X. Q. Pan, S. K. Streiffer, L. Q. Chen, S. W. Kirchoefer, J. Levy, and D. G. Schlom, *Nature (London)* **430**, 758 (2004).
- [42] K. J. Choi, M. Biegalski, Y. L. Li, A. Sharan, J. Schubert, R. Uecker, P. Reiche, Y. B. Chen, X. Q. Pan, V. Gopalan, L.-Q. Chen, D. G. Schlom, and C. B. Eom, *Science* **306**, 1005 (2004).
- [43] J.-P. Locquet, J. Perret, J. Fompeyrine, E. Mächler, J. W. Seo, and G. Van Tendeloo, *Nature (London)* **394**, 453 (1998).
- [44] J. Lettieri, Y. Jia, M. Urbanik, C. I. Weber, J.-P. Maria, D. G. Schlom, H. Li, R. Ramesh, R. Uecker, and P. Reiche, *Appl. Phys. Lett.* **73**, 2923 (1998).
- [45] Q. D. Jiang, Z. J. Huang, P. Jin, C. L. Chen, A. Brazdeikis, Y. Y. Sun, H. H. Feng, A. Benneker, and C. W. Chu, *Surf. Sci. Lett.* **405**, L554 (1998).
- [46] J. H. Cho, S. H. Bang, J. Y. Son, and Q. X. Jia, *Appl. Phys. Lett.* **72**, 665 (1998).
- [47] C.-H. Kim, J.-K. Lee, H.-S. Suh, J. Y. Yi, K.-S. Hong, and T.-S. Hang, *Jpn. J. Appl. Phys., Part 1* **41**, 1495 (2002).
- [48] C. B. Eom, R. J. Cava, R. M. Fleming, J. M. Phillips, R. B. van Dover, J. H. Marshall, J. W. P. Hsu, J. J. Krajewski, and W. F. Peck, Jr., *Science* **258**, 1766 (1992).
- [49] J. J. Randall and R. Ward, *J. Am. Chem. Soc.* **81**, 2629 (1959).
- [50] A. Callaghan, C. W. Moeller, and R. Ward, *Inorg. Chem.* **5**, 1572 (1966).
- [51] L. Klein, J. S. Dodge, T. H. Geballe, A. Kapitulnik, A. F. Marshall, L. Antognazza, and

- K. Char, *Appl. Phys. Lett.* **66**, 2427 (1995).
- [52] X. D. Wu, S. R. Foltyn, R. C. Dye, Y. Coulter, R. E. Muenchausen, *Appl. Phys. Lett.* **62**, 2434 (1993).
- [53] Q. X. Jia, F. Chu, C. D. Adams, X. D. Wu, M. Hawley, J. H. Cho, A. T. Findikoglu, S. R. Foltyn, J. L. Smith, and T. E. Mitchell, *J. Mater. Res.* **11**, 2263 (1996).
- [54] H. N. Lee, H. M. Christen, M. F. Chisholm, C. M. Rouleau, and D. H. Lowndes, *Appl. Phys. Lett.* **84**, 4107 (2004).
- [55] N. Higashi, T. Watanabe, K. Saito, I. Yamaji, T. Akai, and H. Funakubo, *J. Cryst. Growth* **229**, 450 (2001).
- [56] C. H. Ahn, R. H. Hammond, T. H. Geballe, M. R. Beasley, J.-M. Triscone, M. Decroux, Ø. Fisher, L. Antognazza, and K. Char, *Appl. Phys. Lett.* **70**, 206 (1997).
- [57] C. B. Eom, R. B. Van Dover, J. M. Phillips, D. J. Werder, J. H. Marshall, C. H. Chen, R. J. Cava, R. M. Fleming, and D. K. Fork, *Appl. Phys. Lett.* **63**, 2570 (1993).
- [58] S. Matsubara, N. Shohata, and M. Mikami, *Jpn. J. Appl. Phys., Part 1* **24** (Suppl 3), 10 (1985).
- [59] R. A. McKee, F. J. Walker, J. R. Conner, E. D. Specht, and D. E. Zelmon, *Appl. Phys. Lett.* **59**, 782 (1991).
- [60] K. Eisenbeiser, J. M. Finder, Z. Yu, J. Ramdani, J. A. Curless, J. A. Hallmark, R. Droopad, W. J. Ooms, L. Salem, S. Bradshaw, and C. D. Overgaard, *Appl. Phys. Lett.* **76**, 1324 (2000).
- [61] R. A. McKee, F. J. Walker, and M. F. Chisholm, *Phys. Rev. Lett.* **81**, 3014 (1998).
- [62] K. Eisenbeiser, R. Emrick, R. Droopad, Z. Yu, J. Finder, S. Rockwell, J. Holmes, C. Overgaard, and W. Ooms, *IEEE Electron Device Lett.* **23**, 300 (2002).
- [63] Y. Wang, C. Ganpule, B. T. Liu, H. Li, K. Mori, B. Hill, M. Wuttig, R. Ramesha, J. Finder, Z. Yu, R. Droopad, and K. Eisenbeiser, *Appl. Phys. Lett.* **80**, 97 (2002).
- [64] B. T. Liu, K. Maki, Y. So, V. Nagarajan, R. Ramesha, J. Lettieri, J. H. Haeni, D. G. Schlom, W. Tian, X. Q. Pan, F. J. Walker, and R. A. McKee, *Appl. Phys. Lett.* **80**, 4801 (2002).
- [65] S. H. Oh and C.-G. Park, *J. Mater. Res.* **16**, 1998 (2001).
- [66] H. N. Lee, S. Senz, A. Visinoiu, A. Pignolet, D. Hesse, and U. Gösele, *Appl. Phys. A* **71**, 101 (2000).
- [67] D. K. Fork, D. B. Fenner, G. A. N. Connell, J. M. Phillips, T. H. Geballe, *Appl. Phys. Lett.* **57**, 1137 (1990).
- [68] R. D. Vispute, S. M. Kanetkar, S. B. Ogale, K. C. Rajkumar, A. Madhukar, N. Parikh, and B. Patnaik, *Physica C* **199**, 59 (1992).
- [69] S. Y. Hou, J. Kwo, R. K. Watts, J.-Y. Cheng, and D. K. Fork, *Appl. Phys. Lett.* **67**, 1387 (1995).
- [70] H. N. Lee, S. Senz, N. D. Zakharov, C. Harnagea, A. Pignolet, D. Hesse, and U. Gösele, *Appl. Phys. Lett.* **77**, 3260 (2000).

- [71] H. N. Lee, D. Hesse, N. Zakharov, and U. Gösele, *Science* **296**, 2006 (2002).
- [72] A. Inam, M. S. Hegde, X. D. Wu, T. Venkatesan, P. England, P. F. Miceli, E. W. Chase, C. C. Chang, J. M. Tarascon, and J. B. Wachtman, *Appl. Phys. Lett.* **53**, 908 (1988).
- [73] D. B. Chrisey and G. K. Hubler (Eds.), *Pulsed Laser Deposition of Thin Films* (John Wiley & Sons, New York, 1994).
- [74] B. Chapman, *Glow Discharge Processes* (John Wiley & Sons, 1980).
- [75] L. V. Azároff, *Elements of X-Ray Crystallography* (McGraw-Hill, New York, 1968), pp. 360–389.
- [76] B. D. Cullity and S. R. Stock, *Elements of X-Ray Diffraction* (Prentice Hall, New Jersey, 2001).
- [77] D. B. Williams and C. B. Carter, *Transmission Electron Microscopy: A Textbook for Materials Science* (Plenum Press, New York, 1996).
- [78] S. N. Magonov and M.-W. Hwangbo, *Surface Analysis with STM and AFM: Experimental and Theoretical Aspects of Image Analysis* (VCH, Weinheim, 1996).
- [79] C. B. Sawyer and C. H. Tower, *Phys. Rev.* **35**, 269 (1930).
- [80] M. Alexe and A. Gruverman (Eds.), *Nanoscale Characterisation of Ferroelectric Materials: Scanning Probe Microscopy Approach* (Springer, Berlin, 2004).
- [81] M.-W. Chu, M.-T. Caldes, L. Brohan, M. Ganne, A.-M. Marie, O. Joubert, and Y. Piffard, *Chem. Mater.* **16**, 31 (2004).
- [82] R. Ramesh, A. Inam, W. K. Chan, B. Wilkens, K. Myers, K. Remschnig, D. L. Hart, and J. M. Tarascon, *Science* **252**, 944 (1991).
- [83] W. Jo and T. W. Noh, *Appl. Phys. Lett.* **65**, 2780 (1994).
- [84] H. N. Lee, A. Visinoiu, S. Senz, C. Harnagea, A. Pignolet, D. Hesse, and U. Gösele, *J. Appl. Phys.* **88**, 6658 (2000).
- [85] C. D. Theis, J. Yeh, D. G. Schlom, M. E. Hawley, G. W. Brown, J. C. Jiang, and X. Q. Pan, *Appl. Phys. Lett.* **72**, 2817 (1998).
- [86] S. E. Moon, T. K. Song, S. B. Back, S.-I. Kwun, J.-G. Yoon, and J. S. Lee, *Appl. Phys. Lett.* **75**, 2827 (1999).
- [87] K. Ishikawa and H. Funakubo, *Appl. Phys. Lett.* **75**, 1970 (1999).
- [88] T. Nagahama, T. Manabe, I. Yamaguchi, T. Kumagai, T. Tsuchiya, and S. Mizuta, *Thin Solid Films* **353**, 52 (1999).
- [89] M.-W. Chu, S. K. Lee, D. Hesse, and U. Gösele, *Appl. Phys. Lett.* **85**, 2029 (2004)
- [90] M. Hawley, I. D. Raistrick, J. G. Berry, and R. J. Houlton, *Science* **251**, 1587(1991).
- [91] H. N. Lee, D. Hesse, N. Zakharov, S. K. Lee, and U. Gösele, *J. Appl. Phys.* **93**, 5592 (2003).
- [92] H. N. Lee, D. N. Zakharov, S. Senz, A. Pignolet, and D. Hesse, *Appl. Phys. Lett.* **79**, 2961 (2001).
- [93] J. Lettieri, M. A. Zurbuchen, Y. Jia, D. G. Schlom, S. K. Streiffer, and M. E. Hawley, *Appl. Phys. Lett.* **76**, 2937 (2000).

- [94] J. Lettieri, M. A. Zurbuchen, Y. Jia, D. G. Schlom, S. K. Streiffer, and M. E. Hawley, *Appl. Phys. Lett.* **77**, 3090 (2000).
- [95] H. N. Lee and D. Hesse, *Appl. Phys. Lett.* **80**, 1040 (2002).
- [96] A. Garg, Z. H. Barber, M. Dawber, J. F. Scott, A. Snedden, and P. Lightfoot, *Appl. Phys. Lett.* **83**, 2414 (2003).
- [97] T. Kojima, T. Sakai, T. Watanabe, H. Funakubo, K. Saito, and M. Osada, *Appl. Phys. Lett.* **80**, 2746 (2002).
- [98] T. Watanabe, H. Funakubo, K. Saito, T. Suzuki, M. Fujimoto, M. Osada, Y. Noguchi, and M. Miyayama, *Appl. Phys. Lett.* **81**, 1660 (2002).
- [99] H. N. Lee, S. Senz, A. Pignolet, and D. Hesse, *Appl. Phys. Lett.* **78**, 2922 (2001).
- [100] R. D. Shannon, *Acta Crystallogr., Sect. A: Cryst. Phys., Diffr., Theor. Gen. Crystallogr.* **32**, 751 (1976).
- [101] P. C. McIntyre, C. J. Maggiore, and M. Nastasi, *J. Appl. Phys.* **77**, 6201 (1995).
- [102] K. H. Ahn, S. Baik, and S. S. Kim, *J. Mater. Res.* **17**, 2334 (2002).
- [103] J. Janek, private communication, Fall 2004.
- [104] H. McMurdie, M. Morris, E. Evans, B. Paretzkin, W. Wong-Ng, and C. Hubbard, *Powder Diffr.* **1**, 84 (1986).
- [105] G. Asayama, J. Lettieri, M. A. Zurbuchen, Y. Jia, S. Trolrier-McKinstry, D. G. Schlom, S. K. Streiffer, J-P. Maria, S. D. Bu, and C. B. Eom, *Appl. Phys. Lett.* **80**, 2371 (2002).
- [106] P. Tiwari, X. D. Wu, S. R. Foltyn, M. Q. Le, I. H. Campbell, R. C. Dye, and R. E. Muenchausen, *Appl. Phys. Lett.* **64**, 634 (1994).
- [107] J.-Y. Hwang, C.-R. Cho, and S.-Y. Jeong, *J. Cryst. Growth* **271**, 50 (2004).
- [108] A. R. James, A. Pignolet, S. Senz, N. D. Zakharov, and D. Hesse, *Solid State Commun.* **114**, 249 (2000).
- [109] Z. Song, C. Lin, L. Wang, J. Huang, D. Hesse, N. D. Zakharov, H. Xu, and M. Okuyama, *Appl. Phys. A* **70**, 355 (2000).
- [110] D. Hesse, N. D. Zakharov, A. Pignolet, A. R. James, and S. Senz, *Cryst. Res. Technol.* **35**, 641 (2000).
- [111] N. D. Zakharov, A. R. James, A. Pignolet, S. Senz, and D. Hesse, *Mater. Res. Soc. Symp. Proc.* **623**, 173 (2000).
- [112] Q. Gan, R. A. Rao, and C. B. Eom, *Appl. Phys. Lett.* **70**, 1962 (1997).
- [113] C. D. Theis and D. G. Schlom, *J. Mater. Res.* **12**, 1297 (1997).
- [114] J. Kwo, R. M. Fleming, H. L. Kao, D. J. Werder, and C. H. Chen, *Appl. Phys. Lett.* **60**, 1905 (1992).
- [115] J. D. Budai, M. F. Chisholm, R. Feenstra, D. H. Lowndes, D. P. Norton, L. A. Boatner, and D. K. Christen, *Appl. Phys. Lett.* **58**, 2174 (1991).
- [116] Z. L. Wang and A. J. Shapiro, *Surf. Sci.* **328**, 141 (1995).
- [117] S. K. Streiffer, B. M. Lairson, and J. C. Bravman, *Appl. Phys. Lett.* **57**, 2501 (1990).
- [118] H. Zheng, L. Salamanca-Riba, R. Ramesh, and H. Li, *Appl. Phys. Lett.* **85**, 2905

- (2004).
- [119] M. Giesen, *Prog. Surf. Sci.* **68**, 1 (2001).
- [120] S. K. Lee, H. N. Lee, X. H. Zhu, D. Hesse, and U. Gösele, *Integr. Ferroelectr.* **68**, 179 (2004).
- [121] J. F. Scott, *Ferroelectric Memories* (Springer, Berlin, 2000).
- [122] J. Junquera and P. Ghosez, *Nature (London)* **422**, 506 (2003).
- [123] Y. L. Du, M. S. Zhang, Q. Chen, Z. R. Yuan, Z. Yin, and Q. A. Zhang, *Solid State Commun.* **124**, 113 (2002).
- [124] S. Okamura, K. Mori, T. Tsukamoto, and T. Shiosaki, *Integr. Ferroelectr.* **18**, 311 (1997).
- [125] M. Alexe, C. Harnagea, D. Hesse, and U. Gösele, *Appl. Phys. Lett.* **75**, 1793 (1999).
- [126] A. Stanishevski, S. Aggarwal, A. S. Prakash, J. Melngailis, and R. Ramesh, *J. Vac. Sci. Technol. B* **16**, 3899 (1998).
- [127] C. S. Ganpule, A. Stanishevsky, S. Aggarwal, J. Melngailis, E. Williams, R. Ramesh, V. Joshi V, and C. P. de Araujo, *Appl. Phys. Lett.* **75**, 3874 (1999).
- [128] C. Harnagea, M. Alexe, J. Schilling, J. Choi, R. B. Wehrspohn, D. Hesse, and U. Gösele, *Appl. Phys. Lett.* **83**, 1827 (2003).
- [129] A. Roelofs, T. Schneller, K. Szot, and R. Waser, *Appl. Phys. Lett.* **81**, 5231 (2002).
- [130] I. Szafraniak, C. Harnagea, R. Scholz, S. Bhattacharyya, D. Hesse, and M. Alexe, *Appl. Phys. Lett.* **83**, 2211 (2003).
- [131] W. Ma, C. Harnagea, D. Hesse, and U. Gösele, *Appl. Phys. Lett.* **83**, 3770 (2003).
- [132] S. K. Lee, W. Lee, M. Alexe, K. Nielsch, D. Hesse, and U. Gösele, *Appl. Phys. Lett.* **86**, 152906 (2005).
- [133] W. Lee, M. Alexe, K. Nielsch, and U. Gösele, *Chem. Mater.* **17**, 3325 (2005).
- [134] W. Ma and D. Hesse, *Appl. Phys. Lett.* **85**, 3214 (2004).
- [135] C. Harnagea, A. Pignolet, M. Alexe, D. Hesse, and U. Gösele, *Appl. Phys. A* **70**, 261 (2000).
- [136] H. Maiwa, N. Iizawa, D. Togawa, T. Hayashi, W. Sakamoto, M. Yamada, and S. Hirano, *Appl. Phys. Lett.* **82**, 1760 (2003).
- [137] C. Harnagea, A. Pignolet, M. Alexe, and D. Hesse, *Integr. Ferroelectr.* **44**, 113 (2002).
- [138] A. Sa Neto and L. E. Cross, *J. Mater. Sci.* **17**, 1409 (1982).
- [139] J. Wang, J. B. Neaton, H. Zheng, V. Nagarajan, S. B. Ogale, B. Liu, D. Viehland, V. Vaithyanathan, D. G. Schlom, U. V. Waghmare, N. A. Spaldin, K. M. Rabe, M. Wuttig, and R. Ramesh, *Science* **299**, 1719 (2003).
- [140] J. Li, J. Wang, M. Wuttig, R. Ramesh, N. Wang, B. Ruetter, A. P. Pyatakov, A. K. Zvezdin, and D. Viehland, *Appl. Phys. Lett.* **84**, 5261 (2004).
- [141] J. Wang, H. Zheng, Z. Ma, S. Prasertchoung, M. Wuttig, R. Droopad, J. Yu, K. Eisenbeiser, and R. Ramesh, *Appl. Phys. Lett.* **85**, 2574 (2004).

Eidesstattliche Erklärung

Ich erkläre, dass ich keine anderen als die von mir angegebenen Quellen und Hilfsmittel zur Erstellung meiner Dissertation verwendet habe. Den benutzten Werken wörtlich oder inhaltlich entnommene Stellen sind als solche gekennzeichnet.

Lee, Sung Kyun

Halle/Saale, 22 Juni 2005

Acknowledgements

I have benefited from a number of people during the study towards this thesis.

First of all, I would like to express my gratitude to my supervisors, Prof. Dr. Ulrich Gösele for giving me the opportunity to do my Ph.D. at the Max Planck Institute of Microstructure Physics, and Priv.-Doz. Dr. Dietrich Hesse for his guidance and his continuous support.

I thank Dr. Stephan Senz for his advice on scientific aspects. I also thank Dr. Marin Alexe for his PFM work on my samples.

My special thanks go to Ho Nyung Lee for his constant encouragement and his helpful advice. His silent enthusiasm towards achieving something deeply impressed me.

I thank my former office-mates, Alina Schilling (Visinoiu), Dinghua Bao, and Andreas Graff for their careful advices. They helped me to survive the highs and lows of the years.

I would like to thank the “Kwangwhamoon” members of Korea Institute Science and Technology for their optimistic advice and encouragement. I am still missing the good times with them discussing about not only various scientific fields but also various issues in the life, how to live, what to do, etc.

I wish to thank Prof. Kie Bong Nahm and Prof. Young Jik Ahn, at the department of physics of the Hallym University, for their encouragement.

Most of all, I must thank my wife, Sung Bum Choi who encouraged me whenever I felt stressed or down, and my beloved son, Jungjin whose cute tricks always make me happy.

Finally, I would like to dedicate this thesis to my parents and my parents-in-law. Without their unconditional love, unreserved support, and endless concern, I would not have finished my work in Germany.

Résumé

First name: Sung Kyun

Family name: Lee

Date of birth: September 19, 1972 (Seoul, Republic of Korea)

Citizenship: Korean

Email: sklee@mpi-halle.de, s.k.lee@hotmail.com

Education

- Ph.D. Candidate (January 2002–Present)
Max Planck Institute of Microstructure Physics
& Martin-Luther-University Halle-Wittenberg, Halle/Saale, Germany
Advisor: Prof. Dr. Ulrich Gösele and Priv.-Doz. Dr. Dietrich Hesse
Thesis title: Growth, microstructure and ferroelectric properties of non-*c*-axis-oriented rare-earth-substituted bismuth titanate thin films and nanostructures
- M.S. Solid State Physics, Department of Physics (March 1998–February 2000)
Korea University, Seoul, South Korea
Advisor: Prof. Dr. Cheol Eui Lee
Thesis title: Study of thermal treatment effect on low dielectric $\text{Sr}_2(\text{Ta,Nb})_2\text{O}_7$ thin films
- B.S. Department of Physics (March 1991–February 1996)
Hallym University, Chuncheon, South Korea

Research Experience

- Korea Institute of Science and Technology Seoul, South Korea
March 2000–December 2001 Educational-Research Cooperation Fellow
Korea Institute of Science and Technology Seoul, South Korea
August 1998–February 2000 Research Trainee

Teaching Experience

- 2001–2001 Lecturer in General Physics
(Kookmin University and Sung Kyun Kwan University)
1998–1999 Lecturer in General Physics Experiment (Korea University)
1996–1996 Teaching Assistant in Department of Physics (Hallym University)

Honors

Best Poster Award, The 16th International Symposium on Integrated Ferroelectrics (ISIF 2004) Gyeongju, Korea (2004).

Lee, Sung Kyun

Halle/Saale, 22. Juni 2005

Publications

1. **S. K. Lee**, D. Hesse, and U. Gösele, “Growth and properties of (104)-oriented ferroelectric Nd-substituted $\text{Bi}_4\text{Ti}_3\text{O}_{12}$ films on Si(100) using (111)-oriented SrRuO_3/Pt electrodes”, *Appl. Phys. Lett.* (in press).
2. **S. K. Lee**, D. Hesse, M. Alexe, W. Lee, K. Nielsch, and U. Gösele, “Growth and characterization of epitaxial ferroelectric lanthanum-substituted bismuth titanate nanostructures with three different orientations”, *J. Appl. Phys.* (in press).
3. D. Hesse, **S. K. Lee**, and U. Gösele, “Microstructure of (104)-oriented $\text{Bi}_{3.25}\text{La}_{0.75}\text{Ti}_3\text{O}_{12}$ and $\text{Bi}_{3.54}\text{Nd}_{0.46}\text{Ti}_3\text{O}_{12}$ ferroelectric thin films on multiply twinned $\text{SrRuO}_3/\text{Pt}(111)$ electrodes on YSZ(100)-buffered Si(100)”, *Phys. Status Solidi A* **202**, 2287 (2005).
4. L. Zhao, M. Steinhart, M. Yosef, **S. K. Lee**, and S. Schlecht, “Large-scale template-assisted growth of LiNbO_3 one-dimensional nanostructures for nano-sensors”, *Sens. Actuators, B* **109**, 86 (2005).
5. X. Zhu, **S. K. Lee**, H. N. Lee, and D. Hesse, “Microstructure of (110)-oriented epitaxial SrRuO_3 thin films grown on off-cut single crystal YSZ(100) substrates”, *Mater. Sci. Eng., B* **118**, 65 (2005).
6. **S. K. Lee**, W. Lee, M. Alexe, K. Nielsch, D. Hesse, and U. Gösele, “Well-ordered large-area arrays of epitaxial ferroelectric $(\text{Bi},\text{La})_4\text{Ti}_3\text{O}_{12}$ nanostructures fabricated by gold nanotube-membrane lithography”, *Appl. Phys. Lett.* **86**, 152906 (2005).
7. **S. K. Lee**, D. Hesse, U. Gösele, and H. N. Lee, “Reducing azimuthal domains in epitaxial ferroelectric lanthanum-substituted bismuth titanate films using miscut yttria-stabilized zirconia substrates”, *Appl. Phys. Lett.* **86**, 142903 (2005).
8. D. Bao, **S. K. Lee**, X. Zhu, M. Alexe, and D. Hesse, “Growth, structure, and properties of all-epitaxial ferroelectric $(\text{Bi},\text{La})_4\text{Ti}_3\text{O}_{12}/\text{Pb}(\text{Zr}_{0.4},\text{Ti}_{0.6})\text{O}_3/(\text{Bi},\text{La})_4\text{Ti}_3\text{O}_{12}$ trilayered thin films on SrRuO_3 -covered $\text{SrTiO}_3(011)$ substrates”, *Appl. Phys. Lett.* **86**, 082906 (2005).
9. L. Zhao, M. Steinhart, M. Yosef, **S. K. Lee**, T. Geppert, E. Pippel, R. Scholz, U. Gösele, and S. Schlecht, “Lithium niobate microtubes within ordered macroporous silicon by templated thermolysis of a single source precursor”, *Chem. Mater.* **17**, 3 (2005).
10. **S. K. Lee**, H. N. Lee, X. H. Zhu, D. Hesse, and U. Gösele, “Reducing azimuthal domains in (100)- or (118)-oriented ferroelectric $\text{Bi}_{3.25}\text{La}_{0.75}\text{Ti}_3\text{O}_{12}$ films using off-cut single substrates”, *Integr. Ferroelectr.* **66**, 179 (2004).
11. M.-W. Chu, **S. K. Lee**, D. Hesse, and U. Gösele, “ 90° *a-b* domains in epitaxial ferroelectric $\text{Bi}_{3.25}\text{La}_{0.75}\text{Ti}_3\text{O}_{12}$ Films”, *Appl. Phys. Lett.* **85**, 2029 (2004).
12. Y. Luo, **S. K. Lee**, H. Hofmeister, M. Steinhart, and U. Gösele, “Pt nanoshell tubes by template wetting”, *Nano Lett.* **4**, 143 (2004).
13. H. N. Lee, H. M. Christen, C. M. Rouleau, S. Senz, **S. K. Lee**, D. Hesse, and D. H. Lowndes, “Compositionally asymmetric tri-color superlattices grown by pulsed laser deposition”, *Mater. Res. Soc. Symp. Proc.* **784**, C3.24 (2004).

14. M.-W. Chu, **S. K. Lee**, N. D. Zakharov, H. N. Lee, and D. Hesse, "TEM microstructure investigations of mixed (100)/(118)-oriented ferroelectric $\text{Bi}_{3.25}\text{La}_{0.75}\text{Ti}_3\text{O}_{12}$ films", *Microsc. Microanal.* **9** (Suppl. 3), 242 (2003).
15. H. N. Lee, D. Hesse, N. Zakharov, **S. K. Lee**, and U. Gösele, "Growth of uniformly *a*-axis-oriented ferroelectric lanthanum-substituted bismuth titanate films on silicon substrates", *J. Appl. Phys.* **93**, 5592 (2003).
16. Y. W. Lee, D. Kang, Y. Roh, **S. K. Lee**, and Y. Kim, "Effect of charge trapping on the asymmetrical shift of memory window in MFIS devices", *Integr. Ferroelectr.* **49**, 31 (2002).
17. E. K. Kang, H. K. Jang, **S. K. Lee**, E. R. Park, C. E. Lee, K. M. Kim, S. J. Noh, and S.-J. Yoem, "Low-temperature processing of sol-gel-derived lead-zirconate-titanate thin films by oxygen-plasma treatment", *Curr. Appl. Phys.* **2**, 407 (2002).
18. **S. K. Lee**, Y. T. Kim, S.-I. Kim, and C. E. Lee, "Effects of coercive voltage and charge injection on memory windows of metal-ferroelectric-semiconductor and metal-ferroelectric-insulator-semiconductor gate structures", *J. Appl. Phys.* **91**, 9303 (2002).
19. C. E. Lee, H. K. Jang, E. R. Park, E. K. Kang, **S. K. Lee**, and S. J. Noh, "Oxygen-plasma treatment of sol-gel-derived lead zirconate titanate thin films", *Ferroelectrics* **269**, 123 (2002).
20. H. K. Jang, **S. K. Lee**, C. E. Lee, S. J. Noh, and W. I. Lee, "Oxygen plasma effects on sol-gel-derived lead-zirconate-titanate thin films", *Appl. Phys. Lett.* **76**, 882 (2000).
21. H. K. Jang, H. N. Lee, **S. K. Lee**, C. E. Lee, S. J. Noh, W. I. Lee, and K. S. Lee, "A study of oxygen-plasma treatment effect on $\text{Pb}(\text{Zr}_x\text{Ti}_{1-x})\text{O}_3$ ferroelectric thin films", *Ungyong Mulli* (The Korean Physical Society) **12**, 213 (1999).

Selected Presentations

- M. Alexe, W. Lee, **S. K. Lee**, K. Nielsch, D. Hesse, and U. Gösele, “Nanoscale PZT structures and capacitors obtained by gold nanotube membrane lift-off lithography”, The 17th International Symposium on Integrated Ferroelectrics (ISIF 2005), Shanghai, China (2005).
- **S. K. Lee**, H. N. Lee, and D. Hesse, “Reduction of azimuthal domains in (100)- and (118)-oriented ferroelectric $\text{Bi}_{3.25}\text{La}_{0.75}\text{Ti}_3\text{O}_{12}$ films making use of YSZ and Si substrates with definite off-cut”, The 69th Annual Meeting of the German Physical Society, Berlin, Germany (2005).
- **S. K. Lee**, W. Lee, M. Alexe, K. Nielsch, and D. Hesse, “Ferroelectric nanostructure arrays grown by PLD using metal nanotube membranes as deposition masks”, The 69th Annual Meeting of the German Physical Society, Berlin, Germany (2005).
- W. Lee, H. Fan, **S. K. Lee**, S. Richter, S. Matthias, W. Wulfhekel, M. Zacharias, D. Hesse, J. Kirschner, E. Moyon, M. Hanbuecken, K. Nielsch, and U. Gösele, “Metal nanotube membranes with sub-100 nm apertures and their lithographic applications”, Materials Research Society (MRS) Spring Meeting, Boston, USA (2004).
- **S. K. Lee**, M.-W. Chu, N. Zakharov and D. Hesse, “90° domains in ferroelectric $\text{Bi}_{3.25}\text{La}_{0.75}\text{Ti}_3\text{O}_{12}$ films”, The 8th International Symposium on Ferroic Domains (ISFD-8), Tsukuba, Japan (2004).
- X. H. Zhu, **S. K. Lee**, and D. Hesse, “Epitaxial growth and microstructures of (110)-oriented SrRuO_3 thin films on off-cut single crystal substrates”, European Materials Research Society (E-MRS) Spring Meeting, Strasbourg, France (2004).
- **S. K. Lee**, H. N. Lee, N. D. Zakharov, X. H. Zhu, and D. Hesse, “Reducing azimuthal domains in (100)- or (118)-oriented ferroelectric $\text{Bi}_{3.25}\text{La}_{0.75}\text{Ti}_3\text{O}_{12}$ films using off-cut single crystal substrates”, The 16th International Symposium on Integrated Ferroelectrics (ISIF 2004), Gyeongju, Korea (2004).
- H. N. Lee, H. M. Christen, C. M. Rouleau, D. H. Lowndes, **S. K. Lee**, S. Senz and D. Hesse, “Compositionally asymmetric tri-color superlattices grown by high-pressure pulsed laser deposition”, Materials Research Society (MRS) Fall Meeting, Boston, USA (2003).
- M.-W. Chu, **S. K. Lee**, N. D. Zakharov, H. N. Lee, and D. Hesse, “Morphology and microstructure of ferroelectric $\text{Bi}_{3.25}\text{La}_{0.75}\text{Ti}_3\text{O}_{12}$ films grown on Si(100)”, European Materials Research Society (E-MRS) Spring Meeting, Strasbourg, France (2003).